IntechOpen

Seismic Waves
Probing Earth System

Edited by Masaki Kanao and Genti Toyokuni

Seismic Waves - Probing Earth System

Edited by Masaki Kanao and Genti Toyokuni

IntechOpen

Supporting open minds since 2005

Notice
Statements and opinions expressed in the chapters are these of the individual contributors and not necessarily those of the editors or publisher. No responsibility is accepted for the accuracy of information contained in the published chapters. The publisher assumes no responsibility for any damage or injury to persons or property arising out of the use of any materials, instructions, methods or ideas contained in the book.

We are IntechOpen,
the world's leading publisher of Open Access books
Built by scientists, for scientists

4,400+
Open access books available

117,000+
International authors and editors

130M+
Downloads

151
Countries delivered to

Our authors are among the
Top 1%
most cited scientists

12.2%
Contributors from top 500 universities

CLARIVATE ANALYTICS
BOOK CITATION INDEX
INDEXED

WEB OF SCIENCE™

Selection of our books indexed in the Book Citation Index
in Web of Science™ Core Collection (BKCI)

Interested in publishing with us?
Contact book.department@intechopen.com

Numbers displayed above are based on latest data collected.
For more information visit www.intechopen.com

Meet the editors

Dr. Masaki Kanao obtained his Ph.D from Kyoto University. He is currently working at the National Institute of Polar Research in Tokyo, Japan. He has been chiefly interested in the Earth's structure and dynamics for seismological investigations. Polar regions, both in the Arctic and Antarctic, have mainly been studied using both the passive and active seismic source approaches. Recently, interdisciplinary studies regarding glacial earthquakes, cryoseismic events in polar regions, particular around Greenland, have been focusing on involving environmental changes associated with global warming. These investigations and seismic observations in bi-polar regions have had significant contribution to the development of global Earth sciences, Federation of Digital Seismological Network (FDSN) and International Lithospheric Program (ILP), of the International Association of Seismology and Physics of the Earth's Interior (IASPEI) under ICSU.

Dr. Genti Toyokuni obtained his Ph.D from Kyushu University in 2009. He is currently working at the Department of Geophysics, Tohoku University, Japan. He is interested in numerical modeling of seismic wave propagation using the finite-difference method. He has been working on polar seismology, especially in Greenland. He is a member of GLISN (Greenland Ice Sheet Monitoring Network), an international project with 11 countries to construct a seismic and geodetic network in and around Greenland. He has been participating in the field operation on Greenland Ice Sheet every year since 2011.

Contents

Preface

Low-frequency acoustic energy released within the Earth's interior propagates through several types of seismic waves categorized by body waves or surface waves. The importance of seismic wave research lies not only in our ability to understand and predict earthquakes and tsunamis, but it also reveals information on the Earth's composition and features in much the same way as it led to the discovery of Mohorovicic's discontinuity. As our theoretical understanding of the physics behind seismic waves has grown, physical and numerical modeling have greatly advanced and now augment applied seismology for better prediction and engineering practices. This has led to some novel applications such as using artificially-induced shocks for exploration of the Earth's subsurface and seismic stimulation for increasing the productivity of oil wells. This book demonstrates the latest techniques and advances in seismic wave analysis from the theoretical approach, data acquisition and interpretation, to analyses and numerical simulations, as well as research applications. The major topics in this book cover the aspects on seismic wave propagation, characteristics of their velocities and attenuation, deformation process of the Earth's medium, seismic source process and tectonic dynamics with relating observations, as well as propagation modeling of seismic waves.

Dr. Masaki Kanao
Associate Professor,
National Institute of Polar Research,
Midori-cho, Tachikawa-shi,
Tokyo, Japan

Dr. Genti Toyokuni
Department of Geophysics,
Tohoku University,
Sendai, Miyagi,
Japan

A High-Order Finite Volume Method for 3D Elastic Modelling on Unstructured Meshes

Wensheng Zhang

Abstract

In this chapter, a new efficient high-order finite volume method for 3D elastic modelling on unstructured meshes is developed. The stencil for the high-order polynomial reconstruction is generated by subdividing the relative coarse tetrahedrons. The reconstruction on the stencil is performed by using cell-averaged quantities represented by the hierarchical orthonormal basis functions. Unlike the traditional high-order finite volume method, the new method has a very local property like the discontinuous Galerkin method. Furthermore, it can be written as an inner-split computational scheme which is beneficial to reducing computational amount. The reconstruction matrix is invertible and remains unchanged for all tetrahedrons, and thus it can be pre-computed and stored before time evolution. These special advantages facilitate the parallelization and high-order computations. The high-order accuracy in time is obtained by the Runge-Kutta method. Numerical computations including a 3D real model with complex topography demonstrate the effectiveness and good adaptability to complex topography.

Keywords: numerical solutions, computational seismology, 3D elastic wave, wave propagation, high-order finite volume method, unstructured meshes

1. Introduction

Wave propagation based on wave equations has important applications in geophysics. It is usually used as a powerful tool to detect the structures of reservoir. Thus solving wave equations efficiently and accurately is always an important research topic. There are several types of numerical methods to solve wave equations, for example, the finite difference (FD) method [1, 2], the pseudo-spectral (PS) method [3, 4], the finite element (FE) method [5–9], the spectral element (SE) method [10–14], the discontinuous Galerkin (DG) method [15–18], and the finite volume (FV) method [19–22]. Each numerical method has its own inherent advantages and disadvantages. For example, the FD method is efficient and relatively easy to implement, but the inherent restriction of using regular meshes limits its application to complex topography. The FE method has good adaptability to complex topography, but it has huge computational cost. In this chapter, the FV method is the key consideration.

In order to simulate wave propagation on unstructured meshes efficiently, the FV method is a good choice due to its high computational efficiency and good

adaptability to complex geometry. In this chapter an efficient FV method for 3D elastic wave simulation on unstructured meshes is developed. It incorporates some nice features from the DG and FV methods [15–17, 19, 20, 23] and the spectral FV (SFV) method [24–26]. In our method, the computational domain is first meshed with relative coarse tetrahedral elements in 3D or triangle elements in 2D. Then, each element is further divided as a collection of finer subelements to form a stencil. The high-order polynomial reconstruction is performed on this stencil by using local cell-averaged values on the finer elements. The resulting reconstruction matrix on all coarse elements remains unchanged, and it can be pre-computed before time evolution. Moreover, the method can be written as an inner-split computational scheme. These two advantages of our method are very beneficial to enhancing the parallelization and reducing computational cost.

The rest of this chapter is organized as follows. In Section 2, the theory is described in detail. In Section 3, numerical results are given to illustrate the effectiveness of our method. Finally, the conclusion is given in Section 4.

2. Theory

2.1 The governing equation

The three-dimensional (3D) elastic wave equation with external sources in velocity-stress formulation can be written as the following system [1, 15]:

$$
\begin{cases}
\dfrac{\partial \sigma_{xx}}{\partial t} - (\lambda + 2\mu)\dfrac{\partial u}{\partial x} - \lambda\dfrac{\partial v}{\partial y} - \lambda\dfrac{\partial w}{\partial z} = g_1, \\[2ex]
\dfrac{\partial \sigma_{yy}}{\partial t} - \lambda\dfrac{\partial u}{\partial x} - (\lambda + 2\mu)\dfrac{\partial v}{\partial y} - \lambda\dfrac{\partial w}{\partial z} = g_2, \\[2ex]
\dfrac{\partial \sigma_{zz}}{\partial t} - \lambda\dfrac{\partial u}{\partial x} - \lambda\dfrac{\partial v}{\partial y} - (\lambda + 2\mu)\dfrac{\partial w}{\partial z} = g_3, \\[2ex]
\dfrac{\partial \sigma_{xy}}{\partial t} - \mu\left(\dfrac{\partial v}{\partial x} + \dfrac{\partial u}{\partial y}\right) = g_4, \\[2ex]
\dfrac{\partial \sigma_{yz}}{\partial t} - \mu\left(\dfrac{\partial v}{\partial z} + \dfrac{\partial w}{\partial y}\right) = g_5, \\[2ex]
\dfrac{\partial \sigma_{xz}}{\partial t} - \mu\left(\dfrac{\partial u}{\partial z} + \dfrac{\partial w}{\partial x}\right) = g_6, \\[2ex]
\rho\dfrac{\partial u}{\partial t} - \dfrac{\partial \sigma_{xx}}{\partial x} - \dfrac{\partial \sigma_{xy}}{\partial y} - \dfrac{\partial \sigma_{xz}}{\partial z} = \rho g_7, \\[2ex]
\rho\dfrac{\partial v}{\partial t} - \dfrac{\partial \sigma_{xy}}{\partial x} - \dfrac{\partial \sigma_{yy}}{\partial y} - \dfrac{\partial \sigma_{yz}}{\partial z} = \rho g_8, \\[2ex]
\rho\dfrac{\partial w}{\partial t} - \dfrac{\partial \sigma_{xz}}{\partial x} - \dfrac{\partial \sigma_{yz}}{\partial y} - \dfrac{\partial \sigma_{zz}}{\partial z} = \rho g_9,
\end{cases}
\tag{1}
$$

where u, v, and w are the wavefield of particle velocities in x, y, and z directions, respectively; λ and μ are the Lamé coefficients and ρ is the density; $g_i(x,y,z,t)$ are the known sources; σ_{xx}, σ_{yy}, and σ_{zz} are the normal stress components while σ_{xy}, σ_{xz}, and σ_{yz} are the shear stresses. For the convenient of discussion, we rewrite Eq. (1) as the following compact form:

$$\frac{\partial \mathbf{u}}{\partial t} + A\frac{\partial \mathbf{u}}{\partial x} + B\frac{\partial \mathbf{u}}{\partial y} + C\frac{\partial \mathbf{u}}{\partial z} = \mathbf{g}, \tag{2}$$

where $\mathbf{g} = (g_1, \cdots, g_9)^T$, $\mathbf{u} = (\sigma_{xx}, \sigma_{yy}, \sigma_{zz}, \sigma_{xy}, \sigma_{yz}, \sigma_{xz}, u, v, w)^T$, and the matrices A, B, and C are all 9×9 matrices and can be obtained obviously [27].

The propagation velocities of the elastic waves are determined by the eigenvalues s_i of matrices A, B, and C and are given by

$$s_1 = -v_p, \quad s_2 = -v_s, \quad s_3 = -v_s, \quad s_4 = s_5 = s_6 = 0, \quad s_7 = v_s, \quad s_8 = v_s, \quad s_9 = v_p, \tag{3}$$

where

$$v_p = \sqrt{\frac{\lambda + 2\mu}{\rho}}, \quad v_s = \sqrt{\frac{\mu}{\rho}} \tag{4}$$

are the velocities of the compression (P) wave and the shear (S) wave velocities, respectively.

2.2 The generation of a stencil

Suppose that the 3D computational domain Ω is meshed by N_E conforming tetrahedral elements $T^{(m)}$:

$$\Omega = \bigcup_{m=1}^{N_E} T^{(m)}. \tag{5}$$

In practical computations, the integrals in the FV scheme on physical tetrahedral element $T^{(m)}$ are usually changed to be computed on its reference element. **Figure 1** shows a physical tetrahedron $T^{(m)}$ in the physical system, and $x - y - z$ is transformed into a reference element T_E in the reference system $\xi - \eta - \zeta$. Let (x_i, y_i, z_i) for $i = 1, 2, 3, 4$ be the coordinates of physical element $T^{(m)}$. The transformations between $x - y - z$ system and $\xi - \eta - \zeta$ system will be given in the final
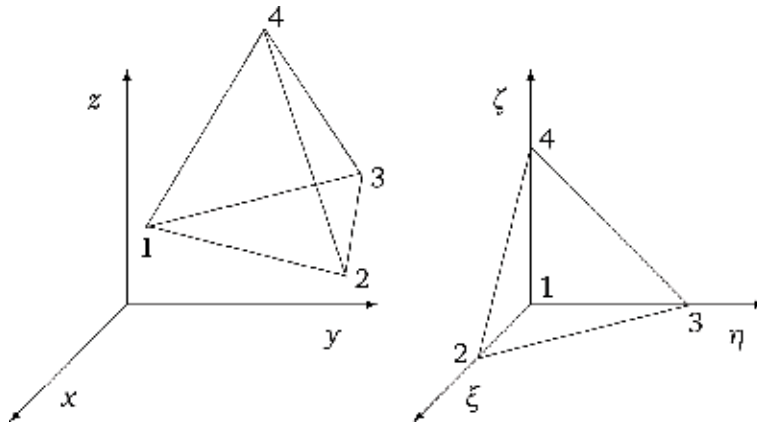
Figure 1.
The physical element $T^{(m)}$ (left) in the physical coordinate system $x - y - z$ is transformed into a reference element T_E (right) in the reference coordinate system $\xi - \eta - \zeta$.

subsection of Section 2. For convenience, let $\mathbf{x} = (x, y, z)$ and $\boldsymbol{\xi} = (\xi, \eta, \zeta)$. And denote the transformation from $\xi - \eta - \zeta$ system to $x - y - z$ system by

$$\mathbf{x} = \mathbf{x}\left(T^{(m)}, \boldsymbol{\xi}\right), \tag{6}$$

and its corresponding inverse transformation by

$$\boldsymbol{\xi} = \boldsymbol{\xi}\left(T^{(m)}, \mathbf{x}\right). \tag{7}$$

The detailed expressions of the transformations (6) and (7) will be given in Section 2.5.

Inside each T_E the solutions of Eq. (2) are approximated numerically by using a linear combination of polynomial basis functions $\phi_l(\xi, \eta, \zeta)$ and the time-dependent coefficients $\hat{\mathbf{w}}_l^{(m)}(t)$:

$$\mathbf{u}^{(m)}(\xi, \eta, \zeta, t) = \sum_{l=1}^{N_p} \hat{\mathbf{w}}_l^{(m)}(t)\phi_l(\xi, \eta, \zeta), \tag{8}$$

where N_p is the degree of freedom of a complete polynomial.

In order to construct a high-order polynomial, we need to choose a stencil. Traditionally, the elements being adjacent to the element $T^{(m)}$ are selected to form a stencil. In [20] three types of stencils, i.e., the central stencil, the primary sector stencil, and the reverse stencil, are investigated. These stencils usually choose $2N$ neighbors for the 3D reconstruction. Here N is the degree of a complete polynomial. Due to geometrical issues, the reconstruction matrix resulting from these stencils may be not invertible. This may happen when all elements are aligned in a straight line [20]. In the following, we propose to partition $T^{(m)}$ or in fact its corresponding reference element T_E into finer subelements to form a stencil. The subdivision algorithm guarantees the number of subelements is greater than the degrees of freedom of a complete polynomial. Moreover, this algorithm is easy to implement especially in 3D and for all elements whether they are internal or boundary elements.

Let N_e be the number of subelements in $T^{(m)}$ after subdividing. For a complete polynomial of degree N in 3D, a reconstruction requires at least N_p subelements, where

$$N_p = (N+1)(N+2)(N+3)/6. \tag{9}$$

In our algorithm, we guarantee N_e is always greater than N_p. As shown in **Figure 2**, we divide each edge of the reference element T_E into M uniform segments. Thus we have $N_e := M^3$ tetrahedral subelements in T_E. Note that a small subcubic in T_E consists of six tetrahedrons. With the transformations of Eqs. (6) and (7), we denote all subelements in $T^{(m)}$ for a fixed m by $T^{(m(k))}$ for $k = 1, \cdots, N_e$. In **Table 1**, the degree of a complete polynomial N and its corresponding degrees of freedom N_p are listed. Correspondingly, the number of M and N_e are also listed in **Table 1**. This algorithm for generating the stencil is easily implemented for all coarse tetrahedrons. Moreover, the reconstruction matrix resulting from this stencil is always invertible and remains unchanged for all elements $T^{(m)}$ for $m = 1, \cdots, N_E$. Note that the reconstruction matrix may be not invertible if all elements are aligned on a straight line [15]. However, this will not happen here for our algorithm.
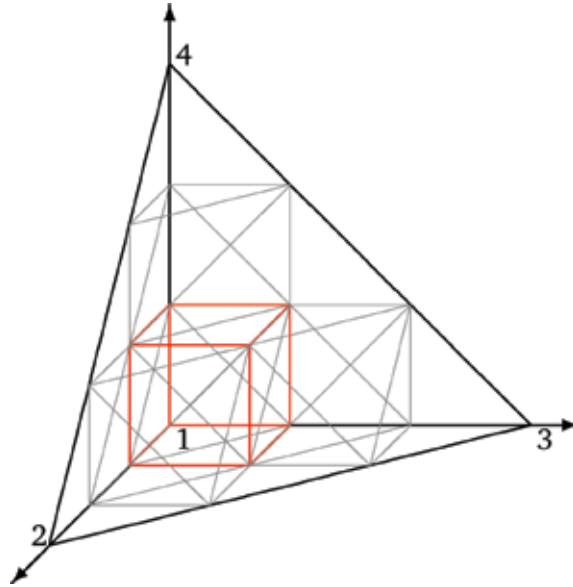
Figure 2.
The stencil obtained by subdividing the reference element T_E into $M^3 = 3^3$ tetrahedral subelements, where $M = 3$ is the number of uniform segments on each edge of T_E. Note that a small subcubic (red) in T_E consists of six tetrahedrons.

N	1	2	3	4
N_p	4	10	20	35
M	2	3	3	4
N_e	8	27	27	64

Table 1.
The degree of a complete polynomial N and its corresponding degrees of freedom N_p are listed. Correspondingly, the number of uniform segments M on each edge and the number of subelements N_e are also listed.

2.3 The high-order polynomial reconstruction

The high-order polynomial is reconstructed in each element $T^{(m)}$ or T_E. For the stencil designed above, we have

$$T^{(m)} = \bigcup_{k=1}^{N_e} T^{(m(k))},\tag{10}$$

where $k = 1, \cdots, N_e$ is the index for subelements in $T^{(m)}$. The FV method will use the cell-averaged quantities, i.e.,

$$\overline{\mathbf{u}}^{(m(k))} = \frac{1}{|T^{(m(k))}|} \int_{T^{(m(k))}} \mathbf{u}^{(m)}(\mathbf{x})dV, \quad k = 1, \cdots, N_e,\tag{11}$$

to reconstruct a high-order polynomial, where $|T^{(m(k))}|$ represents the volume of the subelement $T^{(m(k))}$. The time variable t in $\mathbf{u}^{(m)}$ is omitted for discussion convenience. The reconstruction requires integral conservation for $\mathbf{u}^{(m)}$ in each subelement $T^{(m(k))}$, i.e.,

$$\int_{T^{(m(k))}} \mathbf{u}^{(m)}\left(\mathbf{x}\left(T^{(m)}, \boldsymbol{\xi}\right)\right) dV = |T^{(m(k))}|\overline{\mathbf{u}}^{(m(k))}, \tag{12}$$

$$\forall T^{(m(k))} \subset T^{(m)}, \quad k = 1, \cdots, N_e.$$

To solve the reconstruction problem, inspired by the DG method [15–17, 23, 28, 29], we use hierarchical orthogonal basis functions. The basis functions $\phi_l(\xi, \eta, \zeta)$ of a complete polynomial of degree N ($N = 1, 2, 3, 4$) in the reference coordinate system can be found in [27]. We remark that the basis functions are orthonormal and satisfy the following property:

$$\int_{T_E} \phi_l(\xi, \eta, \zeta) d\xi d\eta d\zeta = \begin{cases} \dfrac{\sqrt{6}}{6}, & l = 1, \\ \\ 0, & l \neq 1. \end{cases} \tag{13}$$

Transforming equation (12) in the physical coordinate system $x - y - z$ into the reference coordinate system $\xi - \eta - \zeta$ and noticing Eq. (8), we obtain

$$\sum_{l=1}^{N_p} \left(\int_{\tilde{T}^{(m(k))}} \phi_l(\xi, \eta, \zeta) d\xi d\eta d\zeta \right) \hat{\mathbf{w}}_l^{(m)} = |\tilde{T}^{(m(k))}|\overline{\mathbf{u}}^{(m(k))}, \tag{14}$$

$$\forall \tilde{T}(m(k)) \subset \tilde{T}(m) = T_E, \quad k = 1, \cdots, N_e,$$

where $\tilde{T}(m)$ is in fact the reference element T_E and $\tilde{T}(m(k))$ is the transformed element corresponding to the subelement $T^{(m(k))}$.

The integration in Eq. (14) over $\tilde{T}(m(k))$ in $\boldsymbol{\xi}$ system can be computed efficiently if it is performed over its reference element in a second reference system $\tilde{\boldsymbol{\xi}}$. Denote the transformation from $\tilde{\boldsymbol{\xi}}$ to $\boldsymbol{\xi}$ and its inverse by $\boldsymbol{\xi} = \boldsymbol{\xi}(\tilde{T}(m(k)), \tilde{\boldsymbol{\xi}})$ and $\tilde{\boldsymbol{\xi}} = \tilde{\boldsymbol{\xi}}(\tilde{T}(m(k)), \boldsymbol{\xi})$, respectively. Transforming Eq. (14) into $\tilde{\boldsymbol{\xi}}$ system and rewriting the result as a compact form, we have

$$G\hat{\mathbf{w}} = \overline{\mathbf{u}}, \tag{15}$$

where G is the $N_e \times N_p$ matrix with entries G_{kl} given by

$$G_{kl} = \frac{1}{|T_E|} \left(\int_{T_E} \phi_l\left(\boldsymbol{\xi}\left(\tilde{T}^{(m(k))}, \tilde{\boldsymbol{\xi}}\right)\right) d\tilde{\xi} d\tilde{\eta} d\tilde{\zeta} \right), \qquad k = 1, \cdots, N_e; \ l = 1, \cdots, N_p, \tag{16}$$

and

$$\overline{\mathbf{u}} := \left(\overline{\mathbf{u}}^{(m(1))}, , \overline{\mathbf{u}}^{(m(2))}, \cdots, \overline{\mathbf{u}}^{(m(N_e))} \right)^T, \quad \hat{\mathbf{w}} := \left(\hat{\mathbf{w}}_1^{(m)}, \hat{\mathbf{w}}_2^{(m)}, \cdots, \hat{\mathbf{w}}_{N_p}^{(m)} \right)^T. \tag{17}$$

We need at least N_p subelements in the stencil since the reconstructed number of degrees of freedom is N_p. As listed in **Table 1**, N_e subelements are used to form the stencil. Note that N_e is definitely larger than N_p, which is helpful to improve the reconstruction robustness [20, 21]. Thus Eq. (15) is an overdetermined problem. We use the constrained least squared technique to solve it.

From the orthogonality of basis functions and the property of Eq. (13), we remark that Eq. (15) is subject to the following constraint condition [27]:

$$\sqrt{6}\hat{\mathbf{w}}_1^{(m)} = \sum_{k=1}^{N_e} \frac{\overline{\mathbf{u}}^{(m(k))}}{N_e}. \tag{18}$$

With the constraint, Eq. (15) is solved by the Lagrange multiplier method [19, 20, 27]. And the system can be written as

$$\begin{pmatrix} 2G^T G & -R^T \\ R & 0 \end{pmatrix} \begin{pmatrix} \hat{\mathbf{w}} \\ \lambda_p \end{pmatrix} = \begin{pmatrix} 2G^T \overline{\mathbf{u}} \\ \tilde{R}\overline{\mathbf{u}} \end{pmatrix}, \tag{19}$$

where λ_p is the Lagrangian multiplier and both R and $\tilde{R}$ are $1 \times N_e$ matrices:

$$R = \left(\sqrt{6}, 0, \cdots, 0\right), \quad \tilde{R} = \left(\frac{1}{N_e}, \cdots, \frac{1}{N_e}\right). \tag{20}$$

The coefficient matrix on the left-hand side of Eq. (19) is the so-called reconstruction matrix [19, 20].

2.4 The spatial discrete formulation

We now derive the semi-discrete finite volume scheme based on Eqs. (2) and (8). Integrating over each subelement $T^{(m(k))}$ on both sides of Eq. (2), we have

$$\int_{T^{(m(k))}} \frac{\partial \mathbf{u}}{\partial t} dV + \int_{T^{(m(k))}} \left(A\frac{\partial \mathbf{u}}{\partial x} + B\frac{\partial \mathbf{u}}{\partial y} + C\frac{\partial \mathbf{u}}{\partial z}\right) dV = 0, \quad k = 1, \cdots, N_e. \tag{21}$$

Using Eq. (8) and integration by parts yield

$$\int_{T^{(m(k))}} \frac{\partial \mathbf{u}}{\partial t} dV + \int_{\partial T^{(m(k))}} \mathbf{F}^h dS = 0, \tag{22}$$

where dS denotes the infinitesimal element in the face integral and $\mathbf{F}^h$ is the numerical flux, and we adopt the widely used Godunov flux [15, 19, 20, 23]

$$\mathbf{F}^h = \frac{1}{2} T\left(A^{(m(k))} + |A^{(m(k))}|\right) T^{-1} \sum_{l=1}^{N_p} \hat{\mathbf{w}}_l^{(m)} \phi_l^{(m)}$$

$$+ \frac{1}{2} T\left(A^{(m(k))} - |A^{(m(k))}|\right) T^{-1} \sum_{l=1}^{N_p} \hat{\mathbf{w}}_l^{(m_j)} \phi_l^{(m_j)}, \tag{23}$$

where m_j is the index number of coarse tetrahedral element neighboring subelement $T^{(m(k))}$. The notation $|A^{(m(k))}|$ denotes applying the absolute value operator of the eigenvalues given in Eq. (3), i.e.,

$$|A^{(m(k))}| = R|\Lambda|R^{-1}, \quad |\Lambda| = \text{diag}(|s_1|, \cdots, |s_9|), \tag{24}$$

where R is the matrix and its columns are made up of the eigenvectors associated with eigenvalues in Eq. (3), i.e.,

$$R = \begin{pmatrix} \lambda+2\mu & 0 & 0 & 0 & 0 & 0 & 0 & 0 & \lambda+2\mu \\ \lambda & 0 & 0 & 0 & 1 & 0 & 0 & 0 & \lambda \\ \lambda & 0 & 0 & 0 & 0 & 1 & 0 & 0 & \lambda \\ 0 & \mu & 0 & 0 & 0 & 0 & 0 & \mu & 0 \\ 0 & 0 & 0 & 1 & 0 & 0 & 0 & 0 & 0 \\ 0 & 0 & \mu & 0 & 0 & 0 & \mu & 0 & 0 \\ v_p & 0 & 0 & 0 & 0 & 0 & 0 & 0 & -v_p \\ 0 & v_s & 0 & 0 & 0 & 0 & 0 & -v_s & 0 \\ 0 & 0 & v_s & 0 & 0 & 0 & -v_s & 0 & 0 \end{pmatrix}. \tag{25}$$

And T is the rotation matrix given by

$$T = \begin{pmatrix} n_x^2 & s_x^2 & t_x^2 & 2n_x s_x & 2s_x t_x & 2n_x t_x \\ n_y^2 & s_y^2 & t_y^2 & 2n_y s_y & 2s_y t_y & 2n_y t_y \\ n_z^2 & s_z^2 & t_z^2 & 2n_z s_z & 2s_z t_z & 2n_z t_z \\ n_y n_x & s_y s_x & t_y t_x & n_y s_x + n_x s_y & s_y t_x + s_x t_y & n_y t_x + n_x t_y \\ n_z n_y & s_z s_y & t_z t_y & n_z s_y + n_y s_z & s_z t_y + s_y t_z & n_z t_y + n_y t_z \\ n_z n_x & s_z s_x & t_z t_x & n_z s_x + n_x s_z & s_z t_x + s_x t_z & n_z t_x + n_x t_z \end{pmatrix}, \tag{26}$$

where (n_x, n_y, n_z) is the normal vector of the face and (s_x, s_y, s_z) and (t_x, t_y, t_z) are the two tangential vectors. T^{-1} denotes the inverse of T.

Inserting Eqs. (23) into (22) and rewriting the result into a splitting form of easy computation in the reference system ξ, we have

$$\frac{\partial}{\partial t}\overline{\mathbf{u}}^{(m(k))}|T^{(m(k))}| + \sum_{j=1}^{4} \mathbf{F}_j^h = 0 \tag{27}$$

with

$$\mathbf{F}_j^h = T^j A^{(m(k))} \left(T^j\right)^{-1} |S_j| \sum_{l=1}^{N_p} F_l^{-,j} \hat{\mathbf{w}}_l^{(m)}, \qquad m = m_j, \tag{28}$$

and

$$\mathbf{F}_j^h = \frac{1}{2}T^j \left(A^{(m(k))} + |A^{(m(k))}|\right) \left(T^j\right)^{-1} |S_j| \sum_{l=1}^{N_p} F_l^{-,j} \hat{\mathbf{w}}^{(m)}$$
$$+ \frac{1}{2}T^j \left(A^{(m(k))} - |A^{(m(k))}|\right) \left(T^j\right)^{-1} |S_j| \sum_{l=1}^{N_p} F_l^{+,i,p} \hat{\mathbf{w}}_l^{(m_j)}, \qquad m \neq m_j, \tag{29}$$

where S_j is the area of the j-th ($j = 1, 2, 3, 4$) face of subelement $T^{(m(k))}$. $F_l^{-,j}$ and $F_l^{+,i,p}$ are the left flux matrix and the right state flux matrix, respectively, which are given by

$$F_l^{-,j} = \int_{\partial(T_E)_j} \phi_l\big(\xi\big(\tilde{T}(m(j)), \tilde{\xi}(j)(\chi, \tau)\big)\big)d\chi d\tau, \quad j = 1, 2, 3, 4, \tag{30}$$

$$F_l^{+,i,p} = \int_{\partial(T_E)_j} \phi_l\left(\xi\left(\tilde{T}(m(i)),\tilde{\xi}(i)\left(\tilde{\chi}^{(p)},\tilde{\tau}^{(p)}\right)\right)\right)d\chi d\tau, \quad i=1,2,3,4; \quad p=1,2,3.$$

$$(31)$$

where χ and τ are the face parameters. The transformation of the face parameters χ and τ to the face parameters $\tilde{\chi}$ and $\tilde{\tau}$ in the neighbor tetrahedron depends on the orientation of the neighbor face with respect to the local face of the considered tetrahedron. And the mapping is given in **Table 2**. For a given tetrahedral mesh with the known indices i and p, there are only 4 of 12 possible matrices $F^{+,i,p}$ per element [15, 20]. Comparing with the traditional FV method, the method with the splitting form described above has much less computations of face integrations. Note that only our proposed FV method can be written as a splitting form. Theoretical analysis shows our method can save about half computational time under the condition of the same number of elements [27].

2.5 The time discretization

Equation (27) is in fact a semi-discrete ordinary differential equation (ODE) system. In order to solve it formally, we denote the spatial semi-discrete part in Eq. (27) by a linear operator L. Then Eq. (27) can be written as a concise ODE form:

$$\frac{d\mathbf{u}}{dt} = L(\mathbf{u},t).$$

$$(32)$$

Traditionally, the classic fourth-order explicit RK (ERK) method

$$\begin{aligned}
\mathbf{k}^{(1)} &= L(\mathbf{u}^n,,t^n),\\
\mathbf{k}^{(2)} &= L\left(\mathbf{u}^n + \frac{1}{2}\Delta t\mathbf{k}^{(1)}, t^n + \frac{1}{2}\Delta t\right),\\
\mathbf{k}^{(3)} &= L\left(\mathbf{u}^n + \frac{1}{2}\Delta t\mathbf{k}^{(2)}, t^n + \frac{1}{2}\Delta t\right),\\
\mathbf{k}^{(4)} &= L\left(\mathbf{u}^n + \Delta t\mathbf{k}^{(3)}, t^n + \Delta t\right),\\
\mathbf{u}^{n+1} &= \mathbf{u}^n + \frac{1}{6}\Delta t\left(\mathbf{k}^{(1)} + 2\mathbf{k}^{(2)} + 2\mathbf{k}^{(3)} + \mathbf{k}^{(4)}\right)
\end{aligned}$$

$$(33)$$

can be applied to advance $\mathbf{u}$ from $\mathbf{u}^n$ to $\mathbf{u}^{n+1}$. Here Δt is the time step. Now we use the low-storage version of ERK (LSERK) to solve Eq. (32):

$$\begin{aligned}
\mathbf{u}^{(0)} &= \mathbf{u}^n,\\
&\begin{cases} \mathbf{k}^{(i)} = a_i\mathbf{k}^{(i-1)} + \Delta tL\left(\mathbf{p}^{(i-1)}, t^n + c_i\Delta t\right),\\ \mathbf{p}^{(i)} = \mathbf{p}^{(i-1)} + b_i\mathbf{k}^{(i)}, \quad\quad i=1,\cdots,5, \end{cases}\\
\mathbf{u}^{(n+1)} &= \mathbf{p}^{(5)}.
\end{aligned}$$

$$(34)$$

p	1	2	3
$\tilde{\chi}$	τ	$1-\chi-\tau$	χ
$\tilde{\tau}$	χ	τ	$1-\chi-\tau$

Table 2.
Transformation of the face parameters χ and τ to the face parameters $\tilde{\chi}$ and $\tilde{\tau}$.

As we can see the LSERK only requires one additional storage level, while ERK has four. The coefficients required in Eq. (34) are listed in **Table 3** [30].

As to the stability condition, it is controlled by the Courant-Friedrichs-Lewy (CFL) condition [15, 19];

$$\Delta t \leq \frac{1}{2N+1} \frac{h_{\min}}{v_p},\tag{35}$$

where v_p is the P wave velocity and $h_{\min}$ is the minimum diameter of the circumcircles of tetrahedral elements. This condition is a necessary condition for discrete stability, and a bit more restrictive form is actually used in numerical computations.

The absorbing boundary conditions (ABCs) in computations are required as the computational domain is finite. There are two typical ABCs to be adopted here. One is flux type ABCs [16, 19]. That is to say, the following numerical flux in Eq. (23) at all tetrahedral faces that coincide with domain boundary

$$\mathbf{F}^h = \frac{1}{2} T \Big(A^{(m(k))} + |A^{(m(k))}| \Big) T^{-1} \sum_{l=1}^{N_p} \hat{\mathbf{w}}_l^{(m)} \phi_l^{(m)},\tag{36}$$

which allows only for outgoing waves and is equivalent to the first order ABCs. Though the absorbing effects of this method vary the angles of incidence, it is still effective in many cases [19]. The advantage of this type ABCs is that it merged into the FVM framework naturally and there is almost no additional computational cost. Another type is the perfectly matched layer (PML) technique originally developed by [31], which is very popular in recent more 10 years.

2.6 Coordinate transformation

The transformation between different coordinate systems is frequently used. For ease of reading, we present the formulations here. Let (x_i, y_i, z_i) for $i = 1, 2, 3, 4$ be the coordinates of a physical element. The transformation from $\xi - \eta - \zeta$ system to $x - y - z$ system is defined by

$$\begin{cases} x = x_1 + (x_2 - x_1)\xi + (x_3 - x_1)\eta + (x_4 - x_1)\zeta, \\ y = y_1 + (y_2 - y_1)\xi + (y_3 - y_1)\eta + (y_4 - y_1)\zeta, \\ z = z_1 + (z_2 - z_1)\xi + (z_3 - z_1)\eta + (z_4 - z_1)\zeta, \end{cases}\tag{37}$$

then the transformation from $x - y - z$ system to $\xi - \eta - \zeta$ system can be solved for ξ, η and ζ from Eq. (37) by the Cramer ruler, i.e.,

i	a_i	b_i	c_i
1	0	0.1496590219992291	0
2	-0.4178904744998519	0.3792103129996273	0.1496590219992291
3	-1.1921516946426769	0.8229550293869817	0.3704009573642048
4	-1.6977846924715279	0.6994504559491221	0.6222557631344432
5	-1.5141834442571558	0.1530572479681520	0.9582821306746903

Table 3.
Coefficients for the low-storage five-stage fourth-order ERK method.

$$\xi = \frac{|J_1|}{|J|}, \qquad \eta = \frac{|J_2|}{|J|}, \qquad \zeta = \frac{|J_3|}{|J|}, \qquad (38)$$

where

$$|J_1| = \begin{vmatrix} x - x_1 & x_3 - x_1 & x_4 - x_1 \\ y - y_1 & y_3 - y_1 & y_4 - y_1 \\ z - z_1 & z_3 - z_1 & z_4 - z_1 \end{vmatrix}, \qquad |J_2| = \begin{vmatrix} x_2 - x_1 & x - x_1 & x_4 - x_1 \\ y_2 - y_1 & y - y_1 & y_4 - y_1 \\ z_2 - z_1 & z - z_1 & z_4 - z_1 \end{vmatrix}, \qquad (39)$$

$$|J_3| = \begin{vmatrix} x_2 - x_1 & x_3 - x_1 & x - x_1 \\ y_2 - y_1 & y_3 - y_1 & y - y_1 \\ z_2 - z_1 & z_3 - z_1 & z - z_1 \end{vmatrix}, \qquad |J| = \begin{vmatrix} x_2 - x_1 & x_3 - x_1 & x_4 - x_1 \\ y_2 - y_1 & y_3 - y_1 & y_4 - y_1 \\ z_2 - z_1 & z_3 - z_1 & z_4 - z_1 \end{vmatrix}. \qquad (40)$$

Note that J is the determinant of the Jacobian matrix of the transformation being equal to six times the volume of the tetrahedron element $T^{(m)}$.

The coordinate transformation from the second reference coordinate $\tilde{\xi} - \tilde{\eta} - \tilde{\zeta}$ to $\xi - \eta - \zeta$ system is defined by

$$\begin{cases} \xi = \xi_1 + (\xi_2 - \xi_1)\tilde{\xi} + (\xi_3 - \xi_1)\tilde{\eta} + (\xi_4 - \xi_1)\tilde{\zeta}, \\ \eta = \eta_1 + (\eta_2 - \eta_1)\tilde{\xi} + (\eta_3 - \eta_1)\tilde{\eta} + (\eta_4 - \eta_1)\tilde{\zeta}, \\ \zeta = \zeta_1 + (\zeta_2 - \zeta_1)\tilde{\xi} + (\zeta_3 - \zeta_1)\tilde{\eta} + (\zeta_4 - \zeta_1)\tilde{\zeta}, . \end{cases} \qquad (41)$$

then the transform from $\xi - \eta - \zeta$ system to $\tilde{\xi} - \tilde{\eta} - \tilde{\zeta}$ system can be solved for $\tilde{\xi} - \tilde{\eta} - \tilde{\zeta}$ from Eq. (41) by Cramer ruler similarly. Denote

$$|\tilde{J}| = \begin{vmatrix} \xi_2 - \xi_1 & \xi_3 - \xi_1 & \xi_4 - \xi_1 \\ \eta_2 - \eta_1 & \eta_3 - \eta_1 & \eta_4 - \eta_1 \\ \zeta_2 - \zeta_1 & \zeta_3 - \zeta_1 & \zeta_4 - \zeta_1 \end{vmatrix}, \qquad (42)$$

which is the determinant of the Jacobian matrix of the transformation being equal to six times the volume of the subelement $\tilde{T}(m(k))$ for $k = 1, \cdots, N_e$. In Eqs. (41) and (42), (ξ_i, η_i, ζ_i) for $i = 1, 2, 3, 4$, denote the vertex coordinates of $\tilde{T}(m(k))$ in $\xi - \eta - \zeta$ system.

3. Numerical computations

In this section we give three numerical examples to illustrate the performance of the developed method above. The convergence test of the proposed method can be found in [27]. Though the method is developed for the 3D case, it can be simplified to 2D without essential difficulty. The principle is the same. The first example is a test for a 2D model with uneven topography. The other two examples are for two 3D models.

Example 1. The first example is a two-layered model with the inclined interface shown in **Figure 3a**. The range of the model is $x \in [-1.6km, 1.6km]$ and $z \in [-1.6km, 1.8km]$. The surface of the model is uneven to imitate the real topography. The v_p and v_s velocities are 3000 m/s and 2000 m/s in the upper layer and 2400 m/s and 1600 m/s in the lower layer, respectively. The densities ρ are 2200 kg/m³ and 1800 kg/m³ in the upper and lower layer, respectively. **Figure 3b** is the coarser triangular meshes for this model. A coarser version of the mesh is
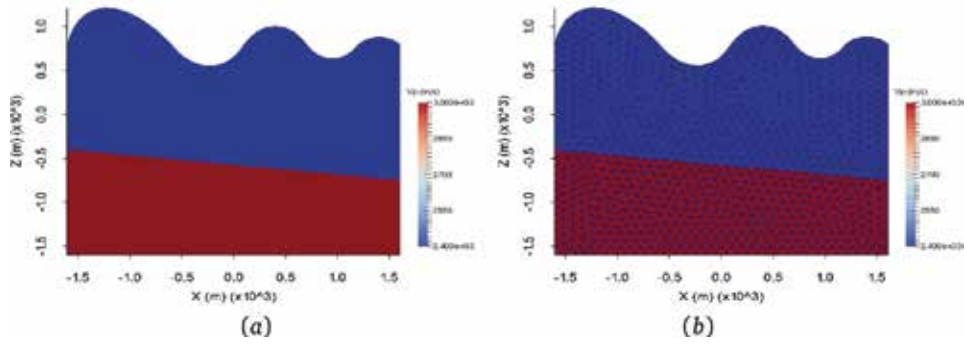
Figure 3.
A two-layered model with curved surface topography (a) and the triangular meshes (b).

shown here as the finest mesh in computations cannot be seen clearly. The triangular meshes can fit the curve topography very well. Note that none triangular element crosses the interface. In computations the P_4 polynomial reconstruction is applied. The computational domain is meshed by 113472 coarse elements. Each coarse element is subdivided into 25 subelements further. So there are 2,836,800 fine elements totally. The time step is $\Delta t = 5 \times 10^{-5}$ s. The source is located at $(x, z) = (0, 0.2km)$ with time history

$$f(t) = -2\alpha(t - t_0)e^{-\alpha(t-t_0)^2}, \qquad t_0 = 0.08, \quad \alpha = \left(\pi f_0\right)^2, \qquad (43)$$

where $f_0 = 20$ Hz is the main frequency. In order to simulate point source excitation, a spatial local distribution function defined by

$$G(\mathbf{x}) = \begin{cases} \exp\left(-7\|\mathbf{x} - \mathbf{x}_0\|_2^2/r_0^2\right), & \|\mathbf{x} - \mathbf{x}_0\|_2^2 \leqslant r_0^2, \\ 0, & \|\mathbf{x} - \mathbf{x}_0\|_2^2 > r_0^2, \end{cases} \qquad (44)$$

is applied, where $\mathbf{x}_0 = \left(x_0, y_0, z_0\right)$ are positions of the source center. The source is added to the u component; that is to say, all source terms except g_7 in Eq. (1) are all zero. **Figure 4** is the snapshots of u and v components at propagation time 0.25 s. **Figure 5** is the snapshots of u and v components at propagation time 0.30 s. We can see the P wave and S wave propagate toward out of the model. The reflected and transmitted waves due to the tilted physical interface are also very clear. These are the expected physical phenomena of wave propagation in elastic media.
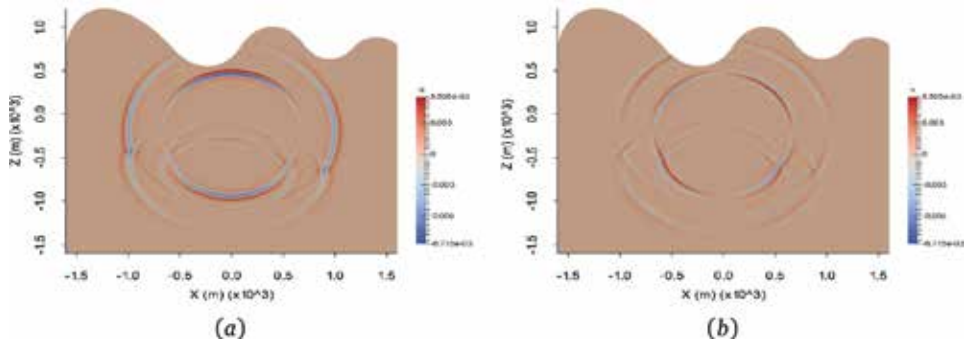
Figure 4.
Snapshots of u component (a) and v component (b) at propagation time 0.25s.
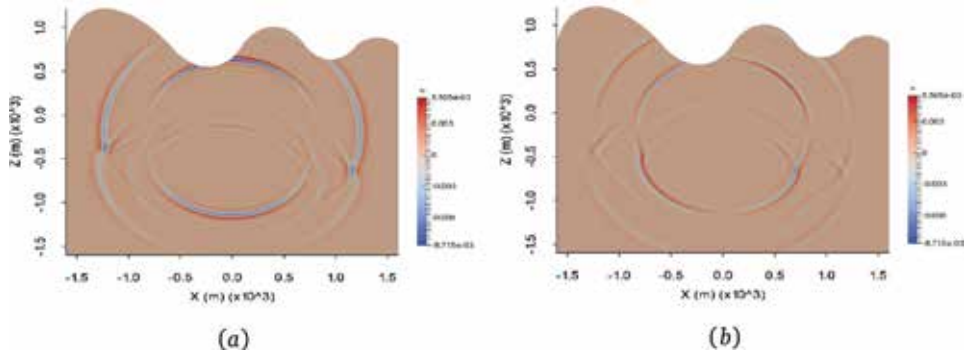
Figure 5.
Snapshots of u component (a) and v component (b) at propagation time 0.30s.

Example 2. The second example is a cuboid model. The physical size of the model is $(x, y, z) \in [0, 2km] \times [0, 2km] \times [0, 1km]$. The model and its unstructured tetrahedral meshes are shown in **Figure 6**. There are totally 836,612 coarse tetrahedrons to mesh the model. A coarser mesh is shown as the actual mesh in computations is too fine to see clearly. Each coarse tetrahedron is subdivided into $N_e = 27$ subelements as we adopt P_3 polynomial reconstruction. The parameters for λ, μ, and ρ are 10^9 Pa, 10^9 Pa, and 1000 kg/m^3. The time step in computations is 10^{-4} s. The source is located in the center of the model with time history given by

$$f(t) = \sin(40\pi t)e^{-100t^2}. \tag{45}$$

It is applied to the u component. The 3D snapshots of u, v, and w components at propagation time 0.42 s are shown in **Figure 7**. From these figures, we can clearly see two types of waves, i.e., the compressive wave and the shear wave. The splitting PML in nonconvolutional form is adopted here [32], and the boundary reflections are absorbed obviously and effectively. The message passing interface (MPI) parallelization based on spatial domain decomposition is applied. The CPU time for extrapolation 1000 time steps is about 33, 310 s with 128 processors each with 2.6 GHz main frequency.
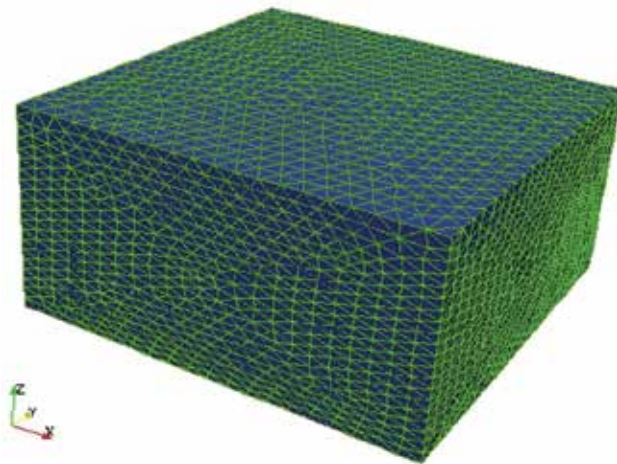
Figure 6.
A cubic model and its unstructured tetrahedral meshes.
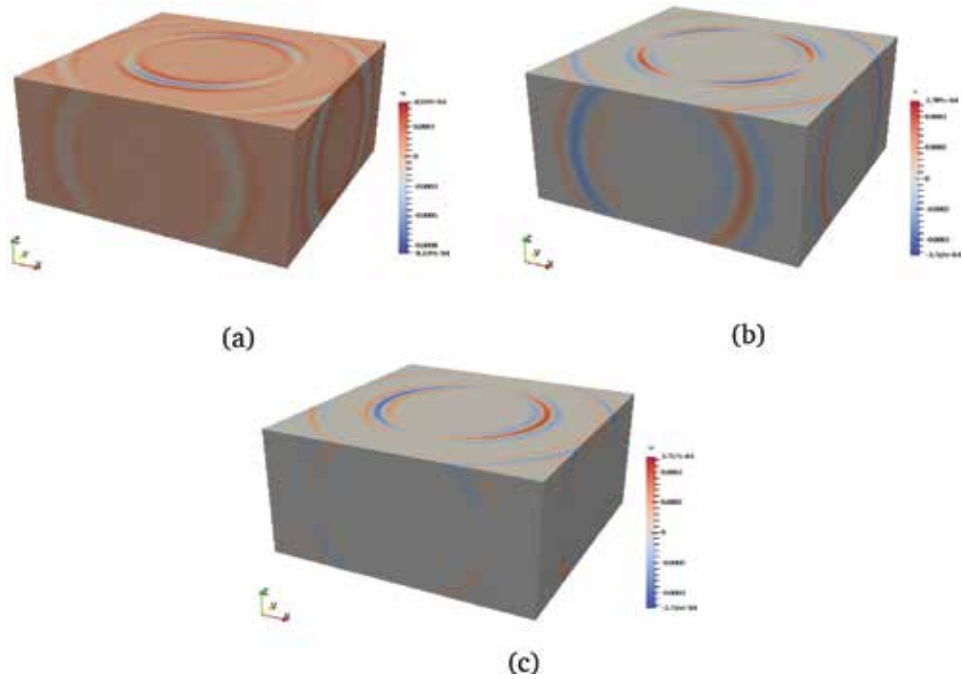
Figure 7.
The 3D snapshots of u component (a), v component (b), and w component (c) at propagation time 0.42 s in a cuboid model. The source is located in the center of the model.

Example 3. The third example is a real geological model in China. As shown in **Figure 8a**, it has a very complex topography. The physical scope of the model is $x \in [0, 2.0km]$, $y \in [0, 3.5km]$, and $z \in [0, 1.1km]$. The corresponding 3D mesh is shown in **Figure 8b**. A coarser version of the mesh is given as the actual mesh in computations is too fine to see clearly in the figure. The model is meshed with 210,701 relative coarse tetrahedral elements. Each coarse tetrahedron is subdivided into $N_e = 64$ subelements as we adopt P_4 polynomial reconstruction, and thus there are 13,484,864 fine elements totally. The time step Δt is 10^{-4} s. The source is situated at $(x_0, y_0, z_0) = (750m, 1300m, 300m)$ with the same time history in Eq. (45). The media velocities of v_p and v_s are $v_p = 3000$ m/s and $v_s = 2000$ m/s. The MPI parallelization based on spatial domain decomposition is applied. The
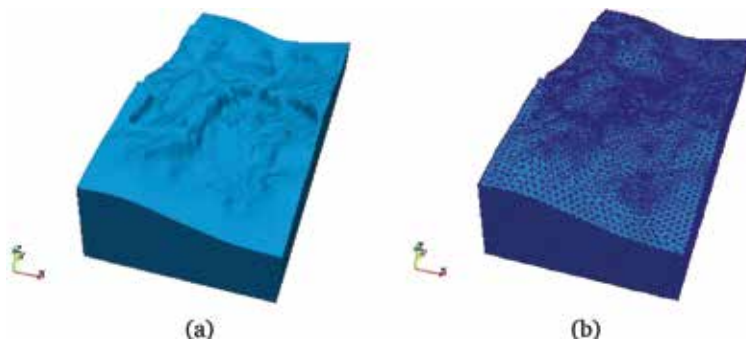
Figure 8.
A real 3D model with complex topography. (a) model and (b) unstructured tetrahedral meshes.
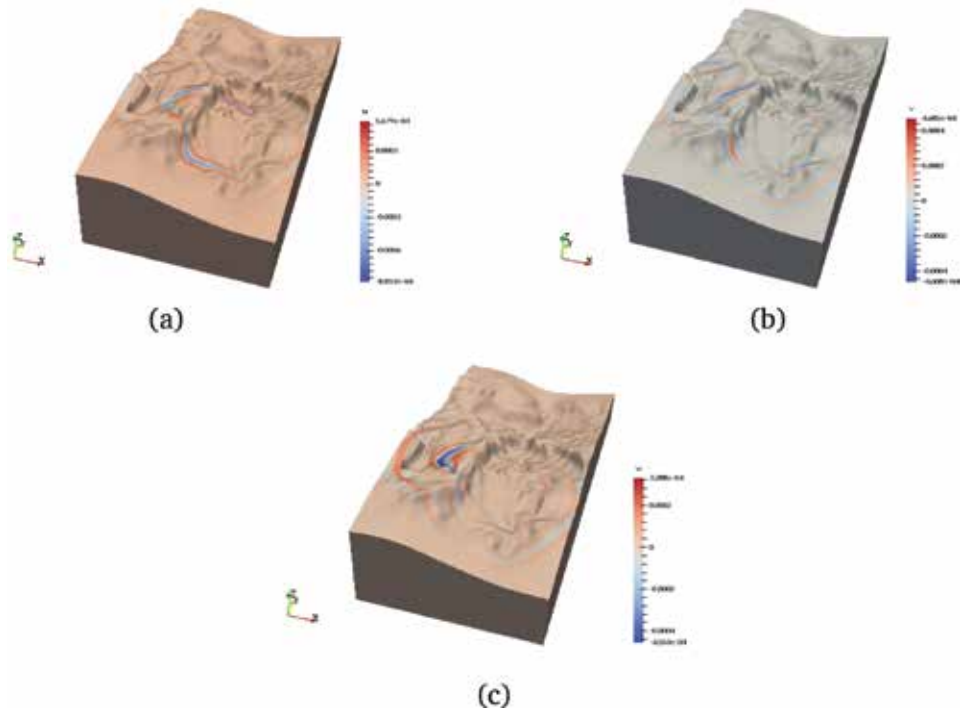
Figure 9.
3D snapshots of u, v, and w components at propagation time 0.80 s in a real 3D model. The results are obtained by the method in this chapter with P_4 reconstruction. (a) u component, (b) v component, (c) w component.

nonconvolutional splitting PML [32] is adopted. The 3D snapshots of u, v, and w components at propagation time 0.80 s are shown in **Figure 9**. The CPU time for extrapolation 10,000 time steps is 100, 449 s with 256 processors each with 2.6 GHz main frequency. From **Figure 9**, we can see clearly the propagation of P wave and S wave.

4. Conclusions

A new efficient high-order finite volume method for the 3D elastic wave simulation on unstructured meshes has been developed. It combines the advantages of the DG method and the traditional FV method. It adapts irregular topography very well. The reconstruction stencil is generated by refining each coarse tetrahedron which can be implemented effectively for all tetrahedrons whether they are internal or boundary elements. The hierarchical orthogonal basis functions are exploited to perform the high-order polynomial reconstruction on the stencil. The resulting reconstruction matrix remains unchanged for all tetrahedrons and can be precomputed and stored before time evolution. The method preserves a very local property like the DG method, while it has high computational efficiency like the FV method. These advantages facilitate 3D large-scale parallel computations. Numerical computations including a 3D real physical model show its good performance. The method also can be expected to solve other linear hyperbolic equations without essential difficulty.

Acknowledgements

Author details

Wensheng Zhang

1 LSEC, ICMSEC, Academy of Mathematics and Systems Science, Chinese Academy of Sciences, Beijing, China

2 School of Mathematics Sciences, University of Chinese Academy Sciences, Beijing, China

*Address all correspondence to: zws@lsec.cc.ac.cn

IntechOpen

References

[1] Minkoff SE. Spatial parallelism of a 3D finite difference velocity-stress elastic wave propagation code. SIAM Journal on Scientific Computing. 2002;**24**:1-19. DOI: 10.1137/S1064827501390960

[2] Virieux J. P-SV wave propagation in heterogeneous media: Velocity-stress finite-difference method. Geophysics. 1986;**51**:889-901. DOI: 10.1190/1.1442147

[3] Klin P, Priolo E, Seriani G. Numerical simulation of seismic wave propagation in realistic 3-D geo-models with a Fourier pseudo spectral method. Geophysical Journal International. 2010;**183**:905-922. DOI: 10.1111/j.1365-246X.2010.04763.x

[4] Zhang W. Stability conditions for wave simulation in 3-D anisotropic media with the pseudospectral method. Communications in Computational Physics. 2012;**12**:703-720. DOI: 10.4208/cicp.120610.090911a

[5] Bécache E, Joly P, Tsogka C. A new family of mixed finite elements for the linear elastodynamic problem. SIAM Journal on Numerical Analysis. 2002;**39**:2109-2132. DOI: 10.2307/4101053

[6] Cohen G, Joly P, Roberts JE, Tordjman N. Higher order triangular finite elements with mass lumping for the wave equations. SIAM Journal on Numerical Analysis. 2001;**38**:2047-2078. DOI: 10.1137/s0036142997329554

[7] Cohen G, Fauqueux S. Mixed finite elements with mass-lumping for the transient wave equation. Journal of Computational Acoustics. 2000;**8**:171-188. DOI: 10.1142/s0218396x0000011x

[8] Cohen G, Fauqueux S. Mixed spectral finite elements for the linear elasticity system in unbounded domains. SIAM Journal on Scientific Computing. 2005;**26**:864-884. DOI: 10.1137/S1064827502407457

[9] Zhang W, Chung E, Wang C. Stability for imposing absorbing boundary conditions in the finite element simulation of acoustic wave propagation. Journal of Computational Mathematics. 2014;**32**:1-20. DOI: 10.4208/jcm.1310-m3942

[10] Dubiner M. Spectral methods on triangles and other domains. Journal of Scientific Computing. 1991;**6**:345-390. DOI: 10.1007/BF01060030

[11] Komatitsch D, Tromp J. Introduction to the spectral element method for three-dimensional seismic wave propagation. Geophysical Journal International. 1999;**139**:806-822. DOI: 10.1046/j.1365-246x.1999.00967.x

[12] Komatitsch D, Martin R, Tromp J, Taylor MA, Wingate BA. Wave propagation in 2-D elastic media using a spectral element method with triangles and quadrangles. Journal of Computational Acoustics. 2001;**9**:703-718. DOI: 10.1142/S0218396X01000796

[13] Komatitsch D, Tromp J. Spectral-element simulations of global seismic wave propagation—I. Validation. Geophysical Journal International. 2002;**149**:390-412. DOI: 10.1046/j.1365-246X.2002.01653.x

[14] Seriani G. 3-D large-scale wave propagation modeling by spectral-element method on Cray T3E multiprocessor. Computer Methods in Applied Mechanics and Engineering. 1998;**164**:235-247. DOI: 10.1016/S0045-7825(98)00057-7

[15] Dumbser M, Käser M. An arbitrary high-order discontinuous Galerkin method for elastic waves on unstructured meshes-II: The three-dimensional isotropic case.

Geophysical Journal International. 2006;**167**:319-336. DOI: 10.1111/j.1365-246X.2006.03120.x

[16] Käser M, Dumbser M. An arbitrary high-order discontinuous Galerkin method for elastic waves on unstructured meshes. I: The two-dimensional isotropic case with external source terms. Geophysical Journal International. 2006;**166**:855-877. DOI: 10.1111/j.1365-246X.2006.03051.x

[17] Käser M, Dumbser M, Puente J, Igel H. An arbitrary high-order discontinuous Galerkin method for elastic waves on unstructured meshes—III: Viscoelastic attenuation. Geophysical Journal International. 2007;**168**:224-242. DOI: 10.1111/j.1365-246X.2006.03193.x

[18] Ye R, de Hoop MV, Petrovitch CL, Pyrak-Nolte LJ, Wilcox LC. A discontinuous Galerkin method with a modified penalty flux for the propagation and scattering of acousto-elastic waves. Geophysical Journal International. 2016;**205**:1267-1289. DOI: 10.1093/gji/ggw070

[19] Dumbser M, Käser M, de la Puente J. Arbitrary high-order finite volume schemes for seismic wave propagation on unstructured meshes in 2D and 3D. Geophysical Journal International. 2007;**171**:665-694. DOI: 10.1111/j.1365-246X.2007.03421.x

[20] Dumbser M, Käser M. Arbitrary high order non-oscillatory finite volume schemes on unstructured meshes for linear hyperbolic systems. Journal of Computational Physics. 2007;**221**:693-723. DOI: 10.1016/j.jcp.2006.06.043

[21] Käser M, Iske A. ADER schemes on adaptive triangular meshes for scalar conservation laws. Journal of Computational Physics. 2005;**205**:486-508. DOI: 10.1016/j.jcp.2004.11.015

[22] Zhang W, Zhuang Y, Chung ET. A new spectral finite volume method for

elastic modelling on unstructured meshes. Geophysical Journal International. 2016;**206**:292-307. DOI: 10.1093/gji/ggw148

[23] Dumbser M, Käser M, Toro EF. An arbitrary high-order discontinuous Galerkin method for elastic waves on unstructured meshes—V: Local time stepping and p-adaptivity. Geophysical Journal International. 2007;**171**:695-717. DOI: 10.1111/j.1365-246X.2007.03427.x

[24] Liu Y, Vinokur M, Wang ZJ. Spectral (finite) volume method for conservation laws on unstructured grids. V: Extension to three-dimensional systems. Journal of Computational Physics. 2006;**212**:454-472. DOI: 10.1016/j.jcp.2003.09.012

[25] Wang ZJ. Spectral (finite) volume method for conservation laws on unstructured grids: Basic formulation. Journal of Computational Physics. 2002;**178**:210-251. DOI: 10.1006/jcph.2002.7041

[26] Wang ZJ, Liu Y. Spectral (finite) volume method for conservation laws on unstructured grids. II: Extension to two-dimensional scalar equation. Journal of Computational Physics. 2002;**179**:665-697. DOI: 10.1006/jcph.2002.7082

[27] Zhang W, Zhuang Y, Zhang L. A new high-order finite volume method for 3D elastic wave simulation on unstructured meshes. Journal of Computational Physics. 2017;**340**:534-555. DOI: 10.1016/j.jcp.2017.03.050

[28] Puente J, Käser M, Dumbser M, Igel H. An arbitrary high-order discontinuous Galerkin method for elastic waves on unstructured meshes-IV: Anisotropy. Geophysical Journal International. 2007;**169**:1210-1228. DOI: 10.1111/j.1365-246X.2007.03381.x

[29] Puente J, Dumbser M, Käser M, Igel H. Discontinuous Galerkin method for

propagation in poroelastic media. Geophysics. 2008;**73**:T77-T97. DOI: 10.1190/1.2965027

[30] Hesthaven JS, Warburton T. Nodal Discontinuous Galerkin Methods. New York: Springer-Verlag; 2008. 502 p. DOI: 10.1007/978-0-387-72067-8

[31] Bérenger JP. A perfectly matched layer for the absorption of electromagnetic waves. Journal of Computational Physics. 1994;**114**: 185-200. DOI: 10.1006/jcph.1996.0181

[32] Collino F, Tsogka C. Application of the perfectly matched absorbing layer model to the linear elastodynamic problem in anisotropic heterogeneous media. Geophysics. 2001;**66**:294-307. DOI: 10.1190/1.1444908

Cylindrical Surface Wave: Revisiting the Classical Biot's Problem

Jeremiah Rushchitsky

Abstract

The problem on a surface harmonic elastic wave propagating along the free surface of cylindrical cavity in the direction of cavity axis is considered. In the case of isotropic medium, this is the classical Biot's problem of 1952. First, the Biot pioneer work is revisited: the analytical part of Biot's findings is shown in the main fragments. The features are using two potentials and representation of solution by Macdonald functions of different indexes. Then the new direct generalization of Biot's problem on the case of transversely isotropic medium within the framework of linear theory of elasticity is proposed. Transition to the transverse isotropy needs some novelty—necessity of using the more complex representations of displacements through two potentials. Finally, a generalization of Biot's problem on the case of isotropic and transversely isotropic media in the framework of linearized theory of elasticity with allowance for initial stresses is stated. This part repeats briefly the results of A.N. Guz with co-authors of 1974. The main features are using the linearized theory of elasticity and one only potential. All three parts are shown as analytical study up to the level when the numerical methods have to be used.

Keywords: surface harmonic cylindrical wave, classical Biot's problem, generalization to the case of transversely isotropic medium

1. Introduction

Note first that the seismic waves include mainly the primary and secondary body waves and different kinds of surface waves. This chapter is devoted to one kind of surface waves. The problem is stated as follows: the infinite medium with cylindrical circular cavity having the symmetry axis Oz and constant radius is analyzed. An attenuating in depth of medium surface harmonic wave propagates along the cavity surface in direction Oz. In this case, the problem becomes mathematically the axisymmetric one. This problem is solved by Biot in 1952 [1] with assumption that the medium is isotropic. The context of this chapter includes four parts. The subchapter 1 "Introduction" is the standard one. The subchapter 2 is named: "Main Stages of Solving the Classical Biot's Problem on Surface Wave along Cylindrical Cavity." Here, the analytical part of Biot's findings is shown in the main fragments. The features are using two potentials and representation of solution by Macdonald functions of different indexes. The subchapter 3 "Direct Generalization of Biot's Problem on the Case of Transversely Isotropic Media within the

Framework of Linear Theory of Elasticity" contains the new approach to the classical Biot's problem and represents the direct generalization of this problem that uses the Biot's scheme of analysis. Transition to the case of transverse isotropy needs some novelty—necessity of using the more complex representations of displacements through two potentials. The subchapter 4 "Genera-lization of Biot's Problem on the case of Isotropic and Transversely Isotropic Media within the framework of Linearized Theory of Elasticity with Allowance for Initial Stresses" repeats briefly the results of A.N. Guz with co-authors (1974). They considered a generalization of the Biot's problem on the case of elastic media with allowance for the initial stresses. The main features are using the linearized theory of elasticity, one only potential, and Macdonald function of one index.

2. Main stages of solving the classical Biot's problem on surface wave along a cylindrical cavity

2.1 Statement of problem and main equations in potentials

A cylindrical system of coordinates $Or\vartheta z$ is chosen, and a harmonic wave is considered that has the phase variable $\sigma = k(z - vt)$, unknown wave number $k = (\omega/v)$, unknown phase velocity v, and arbitrary (but given) frequency ω and ampitude A. It is supposed that the wave propagates in an infinite medium with cylindrical cavity of constant radius r_o in the direction of vertical coordinate z and possibly attenuates in the direction of radial coordinate r. In this linear statement and in assumption that deformations are small, the problem is axisymmetric, and deformations are described by two displacements $(u_r(r,z,t), u_\varphi(r,z,t) = 0$ and $u_z(r,z,t))$ and two Lame equations of the form

$$\frac{C_{11} - C_{12}}{2}\left(\Delta_{rz}u_r - \frac{1}{r^2}u_r\right) + \frac{C_{11} + C_{12}}{2}\left(u_{r,r} + \frac{1}{r}u_r + u_{z,z}\right)_{,r} = \rho u_{r,tt}, \qquad (1)$$

$$\frac{1}{2}(C_{11} - C_{12})\Delta_{rz}u_z + \frac{1}{2}(C_{11} + C_{12})\left(u_{r,r} + \frac{1}{r}u_r + u_{z,z}\right)_{,z} = \rho u_{z,tt}, \qquad (2)$$

or

$$(\lambda + 2\mu)\left(u_{r,rr} + \frac{1}{r}u_{r,r} - \frac{1}{r^2}u_r + u_{z,rz}\right) + \mu(u_{r,zz} - u_{z,rz}) = \rho u_{r,tt} \qquad (3)$$

$$(\lambda + 2\mu)\left(u_{r,rz} + \frac{1}{r}u_{r,z} + u_{z,zz}\right) - \mu\left[\frac{1}{r}(u_{r,z} - u_{z,r}) + (u_{r,rz} - u_{z,rr})\right] = \rho u_{z,tt}. \qquad (4)$$

Further the potentials $\Phi(r,z,t)$, $\Psi(r,z,t)$ are introduced

$$u_r = \Phi_{,r} - \Psi_{,z}, \quad u_z = \Phi_{,z} + \Psi_{,r} + (1/r)\Psi. \qquad (5)$$

When Eq. (5) is substituted into Eqs. (3) and (4), then two uncoupled linear wave equations are obtained:

$$\Delta_{rz}\Phi - (1/v_L)^2\Phi_{,tt} = 0, \qquad (6)$$

$$\Delta_{rz}\Psi - (1/r^2)\Psi - (1/v_T)^2\Psi_{,tt} = 0. \qquad (7)$$

Here the standard notations of Laplace operator Δ_{rz} and velocities of longitudinal and transverse waves in isotropic elastic medium $v_L = \sqrt{(\lambda + 2\mu)/\rho}$, $v_T = \sqrt{\mu/\rho}$ are used.

2.2 Solving the wave equations in the form of Macdonald functions

The solution of Eqs. (6) and (7) is found in the form of harmonic waves in the direction of vertical coordinate:

$$\Phi(r,z,t) = \Phi^*(r)e^{i(kz-\omega t)}, \quad \Psi(r,z,t) = \Psi^*(r)e^{i(kz-\omega t)}, \tag{8}$$

$\Phi(r,z,t) = \Phi^*(r)\cos k(z - vt), \quad \Psi(r,z,t) = \Psi^*(r)\sin k(z - vt).$

A substitution of representations (8) into the wave Eqs. (6) and (7) gives the equations relative to the unknown amplitudes $\Phi^*(r)$, $\Psi^*(r)$

$\Phi^*,_{rr} + (1/r)\Phi^*,_r - \left(k^2 - k_L^2\right)\Phi^* = 0.$

$$\left(\Phi^*,_{rr} + (1/r)\Phi^*,_r - k^2\left(1 - (v/v_L)^2\right)\Phi^* = 0\right), \tag{9}$$

$$\Psi^*,_{rr} - (1/r)\Psi^*,_r - \left[k^2 - k_T^2 + (1/r^2)\right]\Psi^* = 0$$
$$\left(\Psi^*,_{rr} - (1/r)\Psi^*,_r - \left\{k^2\left[1 - (v/v_T)^2\right] + (1/r^2)\right\}\Psi^* = 0\right) \tag{10}$$

These equations correspond to the Bessel equation for Macdonald functions $K_\lambda(x)$ (modified Bessel functions of the second kind [2–4])

$$y'' + (1/x)y' - \left[1 + \left(\lambda^2/x^2\right)\right]y = 0 \tag{11}$$

More exactly, Eqs. (9) and (10) have the solutions in the form of Macdonald functions, if the conditions.

$$k^2 - k_L^2 > 0, \, k^2 - k_T^2 > 0 \left(k^2\left(1 - (v/v_L)^2\right) > 0, \, k^2\left(1 - (v/v_T)^2\right) > 0\right) \tag{12}$$

are fulfilled. According to conditions (12), the wave number of cylindrical wave must be real, and the wave velocity must be less of the velocities of classical longitudinal and transverse plane waves.

Further the wave Eqs. (9) and (10) are considered separately. The first equation is written in the form

$$\Phi^*,_{rr} + (1/r)\Phi^*,_r - m_L^2\Phi^* = 0 \quad m_L = k\sqrt{\left(1 - (v/v_L)^2\right)} \tag{13}$$

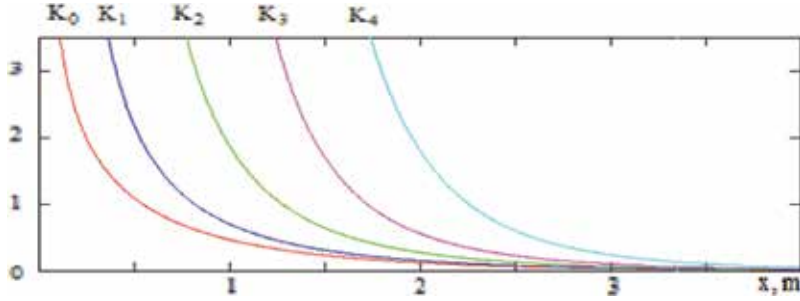This equation has the solution in the form of Macdonald function:

$$\Phi^*(r) = A_\Phi K_0(m_L r) \tag{14}$$

of zeroth order and unknown argument $x = m_L r$, which includes the unknown phase velocity of wave.

The second equation can be written in the form

$$\Psi^*,_{rr} - (1/r)\Psi^*,_r - \left\{m_T^2 + (1/r^2)\right\}\Psi^* = 0 \quad m_T = k\sqrt{\left(1 - (v/v_T)^2\right)}. \tag{15}$$

Figure 1.
Plots of the first five Macdonald functions.

The corresponding solution under conditions (12) is expressed by the Macdonald function $K_1\left(r\sqrt{k^2 - k_T^2}\right)$

$$\Psi^*(r) = A_\Psi K_1(m_T r) \tag{16}$$

of the first order and unknown argument $x = m_T r$, which includes the unknown wave velocity. The amplitude coefficient A_Ψ is assumed to be constant and arbitrary.

Note that the Macdonald functions have the property of attenuation with increasing arguments which is shown in **Figure 1**. Therefore, the propagation along the vertical coordinate z waves (15) and (16) can be considered as the waves with amplitudes $\Phi^*(r)$, $\Psi^*(r)$, which attenuate with increasing the radial coordinate r.

This means that amplitudes can decrease essentially with increasing the distance from the surface of cylindrical cavity. In this sense, the waves (15) and (16) are the surface ones. This forms also the sense of conditions (12). The same conditions are used in the analysis of classical Rayleigh surface wave which propagates along the plane surface of isotropic elastic medium [5–9]. But the Rayleigh wave attenuates as an exponential function when being moved from the free surface, whereas the cylindrical surface Biot's wave attenuates as the Macdonald functions. At that, the arguments in exponential function and Macdonald functions are identical and depend on the wave velocity.

2.3 Boundary conditions: equations for unknown wave number

The boundary conditions correspond to the absence of stresses on surface $r = r_o$

$$\sigma_{rr}(r = r_o, z, t) = 0, \quad \sigma_{rz}(r = r_o, z, t) = 0. \tag{17}$$

The stresses

$$\sigma_{rr} = 2\mu u_{r,r} + \lambda((u_r/r) + u_{r,r} + u_{z,z}), \quad \sigma_{rz} = \mu(u_{r,z} + u_{z,r}) \tag{18}$$

are written through the potentials

$$\sigma_{rr} = (\lambda + 2\mu)(\Phi_{,rr} - \Psi_{,rz}) + \lambda\{(1/r)(\Phi_{,r} - \Psi_{,z}) + \Phi_{,zz} + \Psi_{,rz} + (1/r)\Psi_{,z}\}, \tag{19}$$

$$\sigma_{rz} = \mu\left[(\Phi_{,rz} - \Psi_{,zz}) + \Phi_{,zr} + \Psi_{,rr} + (1/r)\Psi_{,r} - (1/r^2)\Psi\right]. \tag{20}$$

Then the boundary conditions (17) can be written in the form.

$$[2\mu(\Phi,_{rr} - \Psi,_{rz}) + \lambda\Delta\Phi]_{r=r_o} = 0, \mu\left[2(\Phi,_{rz} - \Psi,_{zz}) + \Delta\Psi - (1/r^2)\Psi\right]_{r=r_o} = 0 \quad (21)$$

In the work [1], Biot has used the expressions.

$\Delta\Phi - (1/v_L)^2\Phi,_{tt} = 0, \Delta\Psi - (1/r^2)\Psi - (1/v_T)^2\Psi,_{tt} = 0$ and rewrite Eq. (21) in such a way $\left[(\Phi,_{rr} - \Psi,_{rz}) + (\lambda/2\mu)(1/v_L)^2\Phi,_{tt}\right]_{r=r_o} = 0,$

$\left[2(\Phi,_{rz} - \Psi,_{zz}) + (1/v_T)^2\Psi,_{tt}\right]_{r=r_o} = 0.$

Then the substitution of solutions (14) and (16) into the boundary conditions (21) gives two homogeneous algebraic equations relative to the unknown constant amplitude coefficients

$$\left[1 - (v/v_L)^2 - \frac{\lambda}{\mu}(v/v_L)^2\frac{K_0(m_Lr_o)}{K_0(m_Lr_o) + K_2(m_Lr_o)}\right]A_\Phi - \sqrt{\left(1 - (v/v_L)^2\right)}A_\Psi = 0,$$
$$(22)$$

$$2\sqrt{\left(1 - (v/v_L)^2\right)}A_\Phi + \left(2 - (v/v_T)^2\right)\frac{K_1(m_Tr_o)}{K_1(m_Lr_o)}A_\Psi = 0. \quad (23)$$

An analysis of these equations that describe the cylindrical surface wave is very similar to the analysis that has been carried out by Rayleigh for the classical wave propagating along the plane surface. Some novelty in analysis of systems (22) and (23) is consideration of the system relative to quantities $K_1(m_Lr_o)A_\Phi$ and $K_1(m_Sr_o)A_\Psi$

$$\left\{\left(1 - (v/v_L)^2\right)\left[\frac{K_0(m_Lr_o)}{K_1(m_Lr_o)} + \frac{1}{m_Lr_o}\right] - \frac{\lambda}{2\mu}(v/v_L)^2\frac{K_0(m_Lr_o)}{K_1(m_Lr_o)}\right\}K_1(m_Lr_o)A_\Phi$$
$$(24)$$
$$+ \sqrt{\left(1 - (v/v_S)^2\right)}\left[\frac{K_0(m_Tr_o)}{K_1(m_Tr_o)} + \frac{1}{m_Tr_o}\right]K_1(m_Tr_o)A_\Psi = 0,$$

$$2\sqrt{\left(1 - (v/v_L)^2\right)}K_1(m_Lr_o)A_\Phi + \left(2 - (v/v_T)^2\right)K_1(m_Tr_o)A_\Psi = 0. \quad (25)$$

Solving of systems (24) and (25) gives two results. First, the solution is found accurate within one amplitude factor. Second, an equation for determination of phase velocity of cylindrical surface wave can be obtained in an explicit form.

The work of Biot (1952) has demonstrated some art in handling the Macdonald functions and has written Eq. (24) through only functions of the zeroth and first orders. For that, the known formulas

$$K_0'(x) = -K_1(x), \quad K_1'(x) = -K_0''(x),$$
$$K_0''(x) + (1/x)K_0'(x) = K_0(x), \quad K_0''(x) = (1/x)K_1(x) + K_0(x)$$
$$(26)$$

have been used [3]. As a result, the equation for determination of phase velocity of cylindrical wave has the form

$$\left(2 - (v/v_T)^2\right)\left\{\left[2 - (v/v_T)^2\right]\frac{K_0(m_Lr_o)}{K_1(m_Lr_o)} + \frac{\left(1 - (v/v_L)^2\right)}{m_Lr_o}\right\}$$
$$(27)$$
$$- 4\sqrt{\left(1 - (v/v_L)^2\right)}\sqrt{\left(1 - (v/v_T)^2\right)}\left[\frac{K_0(m_Tr_o)}{K_1(m_Tr_o)} + \frac{1}{m_Tr_o}\right] = 0.$$

Let us write the corresponding equation for the Rayleigh wave [5–9] as

$$4\sqrt{1-(v/v_L)^2}\sqrt{1-(v/v_S)^2}-\left[2-(v/v_S)^2\right]^2=0. \qquad (28)$$

Thus, a presence of Macdonald functions in Eq. (27) complicates essentially an analysis of this equation because according to relations $m_L=k\sqrt{\left(1-(v/v_L)^2\right)}$, $m_S=k\sqrt{\left(1-(v/v_T)^2\right)}$ these functions have the unknown velocity in argument.

If the cavity radius is not small, then the Macdonald functions can be represented by the simple formula $K_0(r)=K_1(r)=e^{-r}\sqrt{\pi/2r}$, and Eq. (27) is reduced to the Rayleigh Eq. (28).

Strictly speaking, the analytical part of analysis is ended by obtaining Eq. (27). Further analysis can be continued with the aim of the numerical methods. Biot in [1] has shown some comments and conclusions based on resources of the 1950s.

A possibility of analytical approach is still saved in the problem on existence of the appropriate wave velocity. First of all, Eq. (27) depends on the elastic constants, and this dependence can be shown in the form of dependence on the ratio of known velocities (v_L/v_T). If the notation $(v^2/v_T^2)=z$ is used, then Eq. (27) can be written in the form

$$\left(2-z(v_L/v_T)^2\right)\left\{(2-z)\frac{K_0\left(r_ok\sqrt{1-z(v_L/v_T)^2}\right)}{K_1\left(r_ok\sqrt{1-z(v_L/v_T)^2}\right)}+\frac{\left(1-z(v_L/v_T)^2\right)}{r_ok\sqrt{1-z(v_L/v_T)^2}}\right\}$$
$$-\;4\;\sqrt{(1-z)}\sqrt{1-z(v_L/v_T)^2}\left[\frac{K_0\left(r_ok\sqrt{1-z}\right)}{K_1\left(r_ok\sqrt{1-z}\right)}+\frac{1}{r_ok\sqrt{1-z}}\right]=0. \qquad (29)$$

It seems appropriate to recall here the most known ways of proving the existence of velocity of the classical Rayleigh wave. An initial equation is always Eq. (28). Two different notations $(v^2/v_T^2)=z$ and $v=(1/\theta)$ are used, which generate two different representations of Eq. (28)

$$z\left\{z^3-8(z-1)\left[z-2\left(1-(v_T^2/v_L^2)\right)\right]\right\}=0, \qquad (30)$$

$$\left(2\theta^2-(1/v_T^2)\right)^2-4\theta^2\sqrt{\theta^2-(1/v_T^2)}\sqrt{\theta^2-(1/v_L^2)}=0. \qquad (31)$$

Finding the real root of Eq. (30) is the key step in the analysis of the Rayleigh wave [5–9] . For more than 100 years of analysis of this wave, many methods of proving the existence of real velocity of wave were elaborated.

First of all, the sufficiently useful and exact empirical Viktorov's formula [5].

$$(v/v_T)=\sqrt{z}\approx\frac{0.87+1.12v}{1+v}\quad(v\text{ the Poisson ratio}) \qquad (32)$$

should be shown.

Let us show further briefly some phenomenological methods. Note that the restriction on the Rayleigh wave velocity is already obtained from a statement of the problem—it is less of the velocity of plane transverse wave. This restriction can be written in the form $z<1$ or $\theta>(1/c_T)$.

Method 1 (graphical method [10, 11]). Eq. (30) is considered as a sum of two summands $Z_1 + Z_2 = 0$. The first summand $Z_1 = z^3$ describes a cubic parabola; the lower branch of which lies in the first quadrant of the plane zOZ_1. The second summand describes a quadratic parabola $Z_2 = -8(z-1)\{z - 2[1 - (c_T^2/c_L^2)]\}$, which is concave in the direction of coordinate axis OZ_2. Further the ratio $(c_T^2/c_L^2) = (\mu/(\lambda + 2\mu))$ can be estimated from below and top $0 \leq c_T^2/c_L^2 \leq 1/2$ with allowance for the shear modulus μ that is positive. These parabolas are intersected on the interval $(0; 1)$. More exactly, one of the roots $z = z_C$ of Eq. (30) can be estimated $0.764 \leq \left(z = (c/c_T)^2\right) \leq 0.912$. Here, the minimal value corresponds to the case when the parabola is tangent to the abscissa axis, and the maximal value corresponds to the case when the parabola is moved partially into the fourth quadrant. Thus, the velocity of Rayleigh wave is close to the velocity of plane transverse wave, but always less of its $0.874 \leq (c/c_T) \leq 0.955$.

Method 2 (method of finding the interval, on ends of which the equation possesses the different by sign values [2, 11]). This method is based on the analysis of Eq. (30). The value of equation that corresponds to the point $c_R = c_T$ is positive and equal to 1. The second point is chosen as $c_R = \varepsilon c_T$, where ε is assumed as the small quantity (this point is close to 0). When this value is substituted into Eq. (30), then expression $-2\varepsilon^2[1 - (c_T^2/c_L^2)]$ is always negative. Hence, at least one root of equation lies in the interval $(\varepsilon c_T, c_T)$.

Method 3 (another method of finding the interval, on ends of which the equation possesses the different by sign values [5]). This method is based on the analysis of Eq. (31). The right point is chosen as $\theta = ((1/c_T))$ (similar to method 2). Then Eq. (31) possesses the positive value. The left point corresponds to $\theta \to \infty$. Further an expression (31) is expanded into the power series near the point at infinity. This series starts with the term $-2\theta^2[(1/c_T^2) - (1/c_L^2)]$, which is always negative. So this equation possesses in the chosen points the different sign values. Thus, at least one root of the equation lies in the interval $((1/c_T), \infty)$.

Method 4 (method based on assumption relative to the Poisson ratio [7]). This assumption consists in the choice of value of Poisson ratio that is often used in the analysis of seismic waves in Earth's crust $\nu = \lambda/[2(\lambda + \mu)] = (1/4) \to \lambda = \mu$. Then cubic Eq. (31) (the zeroth root $\theta_1 = 0$ is ignored from a physical considerations) can be solved exactly, and the roots possess the values $\theta_2 = 4, \quad \theta_3 = 2 + (2/\sqrt{3})$, $\theta_4 = 2 - (2/\sqrt{3})$. Since the condition $\theta < 1$ has been fulfilled, then the corresponding root is equal to $\theta_4 = 0.8453$.

The main conclusion from the shown above methods is that they really allow to establish an existence of real root of Rayleigh equation (the real value of velocity of harmonic Rayleigh wave). They give the positive answer on the question whether the Rayleigh wave exists. In the case of other surface waves including the cylindrical wave under consideration, the experience of the classical Rayleigh wave analysis can be quite useful.

3. Cylindrical wave propagating along the surface of the cylindrical cavity in the direction of vertical axis: The case of transversal isotropy of medium

Let us return to the initial statement of problem and consider an infinite medium with cylindrical circular cavity that has the symmetry axis Oz and radius r_o. The medium is assumed to be the transversely isotropic elastic one. It is assumed further that the wave is harmonic in time, and attenuating deep into medium wave

propagates in the direction of axis Oz along the cavity surface. Such a problem can be considered as some generalization of Biot's [1] problem that is solved in the assumption of isotropy of medium on the case of transversal isotropy of medium. Therefore, it seems expedient to recall some facts from the theory of elasticity of transversally isotropic medium.

3.1 Some information on transversally isotropic medium

Let us consider the case when Ox_3 is the axis of symmetry and Ox_1x_2 is the plane of isotropy. This symmetry corresponds to the hexagonal crystalline system. The matrix of elastic properties is characterized by 5 independent elastic constants C_{11}, C_{12}, C_{13}, C_{33}, C_{44} and 12 non-zero components [11–13]:

$$C_{IK} = \begin{vmatrix} C_{11} & C_{12} & C_{13} & 0 & 0 & 0 \\ C_{12} & C_{11} & C_{13} & 0 & 0 & 0 \\ C_{13} & C_{13} & C_{33} & 0 & 0 & 0 \\ 0 & 0 & 0 & C_{44} & 0 & 0 \\ 0 & 0 & 0 & 0 & C_{44} & 0 \\ 0 & 0 & 0 & 0 & 0 & (1/2)(C_{11} - C_{12}) \end{vmatrix}. \tag{33}$$

Then the constitutive relations $\sigma \sim \varepsilon$ have the form [12, 14].

$$\begin{aligned} \sigma_{11} &= C_{11kl}\varepsilon_{kl} = C_{11}\varepsilon_{11} + C_{12}\varepsilon_{22} + C_{13}\varepsilon_{33}, \\ \sigma_{22} &= C_{22kl}\varepsilon_{kl} = C_{12}\varepsilon_{11} + C_{22}\varepsilon_{22} + C_{13}\varepsilon_{33}, \\ \sigma_{33} &= C_{33kl}\varepsilon_{kl} = C_{13}\varepsilon_{11} + C_{13}\varepsilon_{22} + C_{33}\varepsilon_{33}, \\ \sigma_{12} &= (C_{11} - C_{12})\varepsilon_{12}, \sigma_{13} = 2C_{44}\varepsilon_{13}, \sigma_{23} = 2C_{44}\varepsilon_{23}, \end{aligned} \tag{34}$$

or in notations $\sigma \sim u$ [12, 14].

$$\begin{aligned} \sigma_{11} &= C_{11}u_{1,1} + C_{12}u_{2,2} + C_{13}u_{3,3}, \sigma_{22} = C_{12}u_{1,1} + C_{11}u_{2,2} + C_{13}u_{3,3}, \\ \sigma_{33} &= C_{13}u_{1,1} + C_{13}u_{2,2} + C_{11}u_{3,3}, \sigma_{12} = (1/2)(C_{11} - C_{12})(u_{1,2} + u_{2,1}), \\ \sigma_{13} &= C_{44}(u_{1,3} + u_{3,1}), \sigma_{23} = (1/2)C_{44}(u_{2,3} + u_{3,2}). \end{aligned} \tag{35}$$

Also, five independent elastic technical constants are often used.
$E_x = E_y$, $E_x = E_y$, E_z, G_{xy}, $G_{xz} = G_{yz}$, v_{xy}, $v_{xz} = v_{yz}$, $G_{xy} = E_x/(1 + 2v_{xy})$. They are evaluated through C_{NM} by the following formulas:
The longitudinal Young modulus that corresponds to tension along the symmetry axis Oz

$$E_z = C_{33} - \left[2(C_{13})^2/(C_{11} + C_{12}) \right]. \tag{36}$$

The transverse Young modulus that corresponds to tension in the isotropy plane Oxy

$$E_x = (C_{11} - C_{12})\left[(C_{11} + C_{12})C_{33} - 2(C_{13})^2 \right]/\left[C_{11}C_{33} + (C_{13})^2 \right]. \tag{37}$$

The shear modulus that corresponds to the shear along the isotropy plane Oxy

$$G_{xy} = C_{66} = (1/2)(C_{11} - C_{12}). \tag{38}$$

The shear modulus that corresponds to the shear along the symmetry axis Oz

$$G_{xz} = C_{44}. \tag{39}$$

The Poisson ratio that corresponds to the shear along the symmetry axis Oz under tension in the isotropy plane and characterizes the shortening in this plane

$$v_{xz} = C_{13}/(C_{11} + C_{12}). \tag{40}$$

Sometimes, the corresponding Lame moduli are used.

$$\begin{aligned} \lambda_{xy} + 2\mu_{xy} = C_{11}, \quad \lambda_{xy} = C_{12}, \quad \mu_{xy} = (1/2)(C_{11} - C_{12}) \\ \lambda_{xz} + 2\mu_{xz} = C_{33}, \quad \lambda_{xz} = C_{13}, \quad \mu_{xz} = C_{44}. \end{aligned} \tag{41}$$

The Poisson ratio (40) is determined by the known formula of isotropic theory $v_{xz} = \lambda_{xz}/2(\lambda_{xy} + \mu_{xy})$.

The Poisson ratio v_{xy} that corresponds to the shear along the symmetry axis Oz under tension along the isotropy plane is determined also by the classical formula $v_{xy} = \lambda_{xy}/(\lambda_{xy} + \mu_{xy})$.

The constants $C_{11}, C_{12}, C_{13}, C_{33}, C_{44}$ are represented through the technical constants E, E', v, v', G' by the formulas.

$$\begin{aligned} C_{11} &= \frac{1 - (v')^2(E/E')}{1 - v^2 + (1 + 2v)(v')^2(E/E')}E, \quad C_{12} = \frac{v - (v')^2(E/E')}{1 - v^2 + (1 + 2v)(v')^2(E/E')}E, \\ C_{13} &= \frac{v'(1 - v)}{1 - v^2 + (1 + 2v)(v')^2(E/E')}E, \\ C_{33} &= \frac{1 - v^2}{1 - v^2 + (1 + 2v)(v')^2(E/E')}E', \quad C_{44} = G'. \end{aligned} \tag{42}$$

Let us comment briefly some features of transversally isotropic materials. They can be divided on the natural and artificial ones. An example of the classical natural material is the rock. An example of the modern material is a family of fibers "Kevlar®." Kevlar® KM2 [15] is characterized by elastic constants
$E_x = 1.34 \, GPa, \quad E_z = 84.62 \, GPa, \quad G_{xz} = 24.40 \, GPa, \quad v_{xy} = 0.24, \quad v_{xz} = 0.60.$

An example of composite materials can be four fibrous composites of micro- and nanolevels, which are described in [15]. The corresponding elastic constants for some variants of these materials are as follows [15]:

10% of carbon microfibers
$E_x = 3.59 \, GPa, \quad E_z = 25.22 \, GPa, \quad G_{xz} = 1.17 \, GPa, \quad v_{xy} = 0.39, \quad v_{xz} = 0.58.$

10% of graphite microwhiskers
$E_x = 3.69 \, GPa, \quad E_z = 102.4 \, GPa, \quad G_{xz} = 1.14 \, GPa, \quad v_{xy} = 0.39, \quad v_{xz} = 0.62.$

10% of zig-zag carbon nanotubes
$E_x = 3.70 \, GPa, \quad E_z = 67.21 \, GPa, \quad G_{xz} = 1.14 \, GPa, \quad v_{xy} = 0.39, \quad v_{xz} = 0.62.$

10% of chiral carbon nanotubes
$E_x = 3.67 \, GPa, \quad E_z = 126.4 \, GPa, \quad G_{xz} = 1.14 \, GPa, \quad v_{xy} = 0.39, \quad v_{xz} = 0.62.$

The shown above values are typical for the transversally isotropic materials, and therefore they are briefly commented below.

Comment 1. The Young modulus in the direction along the symmetry axis E_z exceeds essentially the Young modulus in the isotropy plane E_x (from 6 to 34 times in examples above but can in some cases exceed 100 times).

Comment 2. The Lame moduli λ_x and λ_z repeat the relations between E_x and E_z.

Comment 3. The Poisson ratio v_{xz} along the symmetry axis Oz exceeds the classical red line in 0.5 for values of this ratio.

Comment 4. The shear moduli G_{xy} and G_{xz} are differed quite moderately.

3.2 The basic formulas for elastic transversely isotropic medium with axial symmetry

Let us write the basic formulas for the case of symmetry axis Oz. Then displacements are characterized by two components $u_r(r,z,t)$, $u_z(r,z,t)$. The motion equations in stresses have the form.

$$\sigma_{rr,r} + \sigma_{rz,z} + (1/r)(\sigma_{rr} - \sigma_{\varphi\varphi}) = 0,\ \sigma_{rz,r} + (1/r)\sigma_{\varphi z,\varphi} + \sigma_{zz,z} + (1/r)\sigma_{rz} = 0. \quad (43)$$

The substitution of constitutive equations.

$$\sigma_{rr} = C_{11}u_{r,r} + C_{12}(1/r)u_r + C_{13}u_{z,z},\ \sigma_{zz} = C_{13}u_{r,r} + C_{13}(1/r)u_r + C_{33}u_{z,z},$$
$$\sigma_{rz} = (1/2)C_{44}(u_{z,r} + u_{r,z}),\ \sigma_{\varphi z} = \sigma_{r\varphi} = 0 \quad (44)$$

into the motion Eqs. (43) gives the motion equations in displacements

$$C_{11}\left[u_{r,rr} + (1/r)u_{r,r} - (1/r^2)u_r\right] + C_{44}u_{r,zz} + [C_{13} + C_{44}]u_{z,rz} = \rho u_{r,tt}, \quad (45)$$

$$C_{44}(u_{z,rr} + (1/r)u_{z,r}) + C_{33}u_{z,zz} + [C_{13} + C_{44}](u_{r,rz} + (1/r)u_{r,z}) = \rho u_{z,tt}. \quad (46)$$

Note that Eqs. (45) and (46) include only four constants (the constant C_{12} is not represented in these equations). This means that displacements and strains are described by only four constants. But the stress state is already described by all five constants.

3.3 Three classical ways of introducing the potentials in transversely isotropic elasticity

The basic equations of the theory of transversely isotropic elasticity are frequently analyzed by the use of potentials. The potentials are introduced in theory of elasticity mainly for static problems. Transition to the dynamic problems is associated with complications that are sometimes impassable. Because the problem on waves is related to the dynamic ones, let us show further the possible complications with introducing the potentials.

Way 1 [12]. It is proposed for the axisymmetric problems of equilibrium (not motion) and is based on introducing one only potential $\varphi(r,z)$ as the function of stresses. The formulas for stresses include four unknown parameters a, b, c, d, which is characteristic for representations in the transversely isotropic elasticity.

$$\sigma_{rr} = -\left\{\varphi_{,rr} + b(1/r)\varphi_{,r} + a\varphi_{,zz}\right\}_{,z},\ \sigma_{\theta\theta} = -\left\{b\varphi_{,rr} + (1/r)\varphi_{,r} + a\varphi_{,zz}\right\}_{,z}, \quad (47)$$

$$\sigma_{zz} = -\left\{c\varphi_{,rr} + c(1/r)\varphi_{,r} + d\varphi_{,zz}\right\}_{,z},\ \sigma_{rz} = -\left\{\varphi_{,rr} + (1/r)\varphi_{,r} + a\varphi_{,zz}\right\}_{,r}. \quad (48)$$

The next step consists in substitution of formulas (47) and (48) into the first equation of equilibrium and the equations that are obtained from the Cauchy relations and formulas for the strain tensor. This permits to determine the unknown parameters through the elastic constants represented in the equilibrium equations. Further, the second equation of equilibrium gives the biharmonic equation for finding the potentials

$$\Delta_{s1}\Delta_{s2}\varphi = 0, \tag{49}$$

where $\Delta_{sN}\varphi = \varphi_{,rr} + (1/r)\varphi_{,r} + \left(1/(s_N)^2\right)\varphi_{,zz}$ $N = 1; 2$ are some "complicated" copies of classical expressions $\Delta\varphi = \varphi_{,rr} + (1/r)\varphi_{,r} + \varphi_{,zz}$ associated with the Laplace operator. Two constants s_N are determined from the algebraic equations

$$s^4 - [(a+c)/d]s^2 + (1/d) = 0,$$

$$s_{1,3} = \pm\sqrt{\frac{a+c+\sqrt{(a+c)^2-4d}}{2d}}, \quad s_{2,4} = \pm\sqrt{\frac{a+c-\sqrt{(a+c)^2-4d}}{2d}}. \tag{50}$$

Thus, a transition from the isotropic case to the transversely isotropic one complicates the procedure of solving the static problems. Here a necessity of solving the classical biharmonic equation is changed on necessity of solving some generalization of this equation in the form (49).

Way 2 [12, 16]. This way is also proposed for the static problems. Here, two potentials are introduced which are linked immediately with displacements

$$u_r = \phi_{1,r} + \phi_{2,r}, \quad u_z = k_1\phi_{1,z} + k_2\phi_{2,z}. \tag{51}$$

A substitution of representations (51) into equations of equilibrium (45), (46)

$$C_{11}\left[u_{r,rr} + (1/r)u_{r,r} - (1/r^2)u_r\right] + C_{44}u_{r,zz} + [C_{13} + C_{44}]u_{z,rz} = 0,$$

$$C_{44}(u_{z,rr} + (1/r)u_{z,r}) + C_{33}u_{z,zz} + [C_{13} + C_{44}](u_{r,rz} + (1/r)u_{r,z}) = 0$$

allows to determine the unknown constants k_1, k_2. An idea consists in that both equations must be transformed in identical equations relative to the potentials by comparing some coefficients

$$\frac{k_{1(2)}(C_{13}+C_{44}) + C_{44}}{C_{11}} = \frac{kC_{33}}{k_{1(2)}C_{44} + (C_{13}+C_{44})} = V.$$

This expression gives the quadratic equation for $k_{1(2)}$ and V

$$V^2 + \frac{C_{13}(2C_{44}+C_{33}) - C_{11}C_{33}}{C_{11}C_{44}}V + \frac{C_{33}}{C_{11}} = 0. \tag{52}$$

Note that the simple link $V_N = (1/s_N)$ exists between constants V_N and s_N, which makes the ways 1 and 2 very similar. Then the potentials fulfill the equations

$$\Delta_{rzN}\varphi_N = \varphi_{N,rr} + (1/r)\varphi_{N,r} + \left(1/(V_N)^2\right)\varphi_{N,zz}. \tag{53}$$

The stresses are expressed through new potentials in such a way

$$\sigma_{rr} = -(C_{11}-C_{12})(1/r)(\phi_{1,rr} + \phi_{2,rr}) - C_{44}((1+k_1)\phi_{1,zz} + (1+k_2)\phi_{2,zz}),$$

$$\sigma_{\theta\theta} = -(C_{11}-C_{12})(1/r)(\phi_{1,rr} + \phi_{2,rr}) - ((C_{13}k_1 - C_{12}V_1)\phi_{1,zz} + (C_{13}k_2 - C_{12}V_2)\phi_{2,zz}),$$

$$\sigma_{zz} = ((C_{33}k_1 - C_{13}V_1)\phi_{1,zz} + (C_{33}k_2 - C_{13}V_2)\phi_{2,zz}),$$

$$\sigma_{rz} = C_{44}((1+k_1)\phi_{1,rz} + (1+k_2)\phi_{2,rz}).$$

$$\tag{54}$$

Way 3 [1, 16]. This way is proposed for equations of motion, but only for the isotropic theory of elasticity. It can be used for the static problems of transversely

isotropic theory of elasticity. The initial equations here are the equations of motion (43) without inertial summands

$$C_{11}\left[u_{r,rr} + (1/r)u_{r,r} - (1/r^2)u_r\right] + C_{44}u_{r,zz} + [C_{13} + C_{44}]u_{z,rz} = 0, \tag{55}$$

$$C_{44}(u_{z,rr} + (1/r)u_{z,r}) + C_{33}u_{z,zz} + [C_{13} + C_{44}](u_{r,rz} + (1/r)u_{r,z}) = 0. \tag{56}$$

The potentials are introduced like (51), but the representations are complicated by necessity of introducing two new unknown parameters:

$$u_r = \Phi,_r - \Psi,_z, \quad u_z = n\Phi,_z + m\Psi,_r + m(1/r)\Psi, \tag{57}$$

A substitution of representations (57) into equations of motion (45) and (46) gives equations relative to the potentials. Eq. (45) gives two equations:

$$\Phi,_{rr} + (1/r)\Phi,_r + \frac{C_{44} + n(C_{13} + C_{44})}{C_{11}}\Phi,_{zz} = 0, \tag{58}$$

$$\Psi,_{rr} + (1/r)\Psi,_r - (1/r^2)\Psi + \frac{C_{44}}{C_{11} - m(C_{13} + C_{44})}\Psi,_{zz} = 0, \tag{59}$$

whereas Eq. (46) gives three equations:

$$\Phi,_{rr} + (1/r)\Phi,_r + \frac{nC_{33}}{nC_{44} + (C_{13} + C_{44})}\Phi,_{zz} = 0, \tag{60}$$

$$\Psi,_{rrz} + (1/r)\Psi,_{rz} - (1/r)^2\Psi,_z + \frac{C_{33}m - (C_{13} + C_{44})}{C_{44}m}\Psi,_{zzz} = 0, \tag{61}$$

$$\Psi,_{rr} + (1/r)\Psi,_r - (1/r)^2\Psi + \frac{C_{33}m - (C_{13} + C_{44})}{C_{44}m}\Psi,_{zz} = 0. \tag{62}$$

The last two equations are identical. Eqs. (58) and (60) and (59) and (62) have to be identical. This means that the coefficients in these equations have to be identical. As a result, two equations can be obtained for the determination of unknown constants n, m.

$$\frac{C_{44} + n(C_{13} + C_{44})}{C_{11}} = \frac{nC_{33}}{nC_{44} + (C_{13} + C_{44})} \rightarrow$$

$$n^2 - n\frac{C_{11}C_{33} - (C_{44})^2 - (C_{13} + C_{44})^2}{C_{44}(C_{13} + C_{44})} + 1 = 0, \tag{63}$$

$$n_{1,2} = \frac{C_{11}C_{33} - (C_{44})^2 - (C_{13} + C_{44})^2}{2C_{44}(C_{13} + C_{44})}$$

$$\times \left(1 \pm \sqrt{1 - 4\left[\frac{C_{44}(C_{13} + C_{44})}{C_{11}C_{33} - (C_{44})^2 - (C_{13} + C_{44})^2}\right]^2}\right), \tag{64}$$

$$\frac{C_{44}}{C_{11} - m(C_{13} + C_{44})} = \frac{C_{33}m - (C_{13} + C_{44})}{C_{44}m} \rightarrow m^2$$

$$+ m\left[\frac{(C_{44})^2 + C_{11}C_{33} + (C_{13} + C_{44})^2}{C_{33}(C_{13} + C_{44})}\right] + \frac{C_{11}}{C_{33}} = 0. \tag{65}$$

$$m_{1,2} = -\frac{(C_{44})^2 + C_{11}C_{33} + (C_{13} + C_{44})^2}{2C_{33}(C_{13} + C_{44})}$$

$$\times \left\{ 1 \pm \sqrt{1 - 4\frac{C_{11}}{C_{33}}\left[\frac{C_{33}(C_{13} + C_{44})}{(C_{44})^2 + C_{11}C_{33} + (C_{13} + C_{44})^2}\right]^2} \right\}. \tag{66}$$

The unknown potentials $\Phi(r,z)$ and $\Psi(r,z)$ have to be determined from the simple Eqs. (63) and (65) which are the classical Bessel equations of orders 0 and 1 and arguments depending on some rational combination of elastic constants.

Thus, three ways of introduction of potentials in the static problems of transversely isotropic theory of elasticity are shown. The different attempts to transfer these ways into the dynamic problems meet some troubles—the presence of inertial summands generates new additional conditions for the unknown constants in representations of potentials. Introducing the new constants does not help—the number of conditions is still more than the number of all constants.

3.4 Solving the problem on the propagation in the direction of vertical axis surface cylindrical wave for the case of transversal isotropy of medium

Consider now equations of motion (45) and (46) and introduce the potentials by the formula (57). A substitution of formula (57) into equations of motion gives five equations relative to the potentials. Eq. (57) gives two equations:

$$\Phi_{,rr} + (1/r)\Phi_{,r} + \frac{C_{44} + n(C_{13} + C_{44})}{C_{11}}\Phi_{,zz} = \frac{\rho}{C_{11}}\Phi_{,tt}, \tag{67}$$

$$\Psi_{,rr} + (1/r)\Psi_{,r} - (1/r^2)\Psi + \frac{C_{44}}{C_{11} - m(C_{13} + C_{44})}\Psi_{,zz} = \frac{\rho}{C_{11} - m(C_{13} + C_{44})}\Psi_{,tt}. \tag{68}$$

Eq. (46) gives three equations:

$$\Phi_{,rr} + (1/r)\Phi_{,r} + \frac{nC_{33}}{nC_{44} + (C_{13} + C_{44})}\Phi_{,zz} = \frac{n\rho}{nC_{44} + (C_{13} + C_{44})}\Phi_{,tt}, \tag{69}$$

$$\Psi_{,rrz} + (1/r)\Psi_{,rz} - (1/r)^2\Psi_{,z} + \frac{C_{33}m - (C_{13} + C_{44})}{C_{44}m}\Psi_{,zzz} = \frac{\rho}{C_{44}}\Psi_{,ztt}, \tag{70}$$

$$\Psi_{,rr} + (1/r)\Psi_{,r} - (1/r)^2\Psi + \frac{C_{33}m - (C_{13} + C_{44})}{C_{44}m}\Psi_{,zz} = \frac{\rho}{C_{44}}\Psi_{,tt}. \tag{71}$$

Two last equations are identical. Also the equations for potential Φ must be identical as well as the equations for potential Ψ must be identical. Let us assume additionally that the problem in hand considering the solution in the form of harmonic in time cylindrical wave with unknown wave number k and known frequency ω:

$$\Phi(r,z,t) = \widehat{\Phi}(r)e^{i(kz-\omega t)}, \quad \Psi(r,z,t) = \widehat{\Psi}(r)e^{i(kz-\omega t)}. \tag{72}$$

Note that characterization of an attenuation of wave depth down functions $\widehat{\Phi}(r)$, $\widehat{\Psi}(r)$ is unknown. They must be found from equations, which are obtained by substitution of representations (72) into Eqs. (67) and (71):

$$\widehat{\Phi}_{,rr} + (1/r)\widehat{\Phi}_{,r} - \left[\frac{C_{44} + n(C_{13} + C_{44})}{C_{11}}k^2 - k_{L(11)}^2\right]\widehat{\Phi} = 0, \qquad (73)$$

$$k_{L(11)} = \left(\omega/v_{L(11)}\right), \, v_{L(11)} = \sqrt{C_{11}/\rho},$$

$$\widehat{\Phi}_{,rr} + (1/r)\widehat{\Phi}_{,r} - \frac{n}{nC_{44} + (C_{13} + C_{44})}\left(C_{33}k^2 - C_{11}k_{L(11)}^2\right)\widehat{\Phi} = 0, \qquad (74)$$

$$\widehat{\Psi}_{,rr} + (1/r)\widehat{\Psi}_{,r} - (1/r^2)\,\widehat{\Psi} - \frac{C_{44}}{C_{11} - m(C_{13} + C_{44})}\left(k^2 - k_{T(44)}^2\right)\widehat{\Psi} = 0, \qquad (75)$$

$$k_{T(44)} = \left(\omega/v_{L(44)}\right), \, v_{L(44)} = \sqrt{C_{44}/\rho},$$

$$\widehat{\Psi}_{,rr} + (1/r)\widehat{\Psi}_{,r} - (1/r)^2\,\widehat{\Psi} - \left[\frac{C_{33}m - (C_{13} + C_{44})}{C_{44}m}k^2 - k_{T(44)}^2\right]\widehat{\Psi} = 0. \qquad (76)$$

As a result, two equations can be obtained that permit to determine the constants n, m

$$n^2 - 2N_1 n + N_2 = 0, \, m^2 + 2M_1 m + M_2 = 0, \qquad (77)$$

$$N_{\pm}(M_{\pm}) = N_1(M_1) \pm \sqrt{[N_1(M_1)]^2 - N_2(M_2)}, \qquad (78)$$

$$2N_1 = \frac{\left[C_{11}C_{33} - (C_{13} + C_{44})^2\right]k^2 - C_{11}[C_{11} - C_{44}]k_{L(11)}^2 - (C_{44})^2}{C_{44}(C_{13} + C_{44})k^2}, \qquad (79)$$

$$N_2 = \frac{C_{44} - C_{11}k_{L(11)}^2}{C_{44}k^2} = 0$$

$$2M_1 = \frac{\left[(C_{44})^2 - C_{11}C_{33} - (C_{13} + C_{44})^2\right]k^2 - \left[(C_{44})^2 - C_{11}C_{44}\right]k_{T(44)}^2}{(C_{13} + C_{44})\left(C_{33}k^2 - C_{44}k_{T(44)}^2\right)}, \qquad (80)$$

$$M_2 = \frac{C_{11}}{\left(C_{33}k^2 - C_{44}k_{T(44)}^2\right)}k^2.$$

Note that restriction on the kind of solution (it has to be a wave) allows to unite two different conditions into one—conditions for equaling coefficients in summands with the second derivative by time t and vertical coordinate z. In this case, the number of unknown constants coincides with the number of conditions which are necessary for the determination of potentials. As a result, the wave attenuation-transformed potentials can be determined from the equations of Bessel type:

$$\widehat{\Phi}_{,rr} + (1/r)\widehat{\Phi}_{,r} - M_{L(11)}^2\,\widehat{\Phi} = 0, \quad M_{L(11)} = \sqrt{\frac{C_{44} + n(C_{13} + C_{44})}{C_{11}}k^2 - k_{L(11)}^2}, \qquad (81)$$

$$\widehat{\Psi}_{,rr} + (1/r)\widehat{\Psi}_{,r} - \left[(1/r^2) + M_{T(44)}^2\right]\widehat{\Psi} = 0,$$

$$M_{T(44)} = \sqrt{\frac{C_{44}}{C_{11} - m(C_{13} + C_{44})}\left(k^2 - k_{T(44)}^2\right)}, \qquad (82)$$

A success in the determination of transformed potentials is accompanied by a complication of conditions which provide the wave attenuation. They have the form.

$$\frac{C_{44} + n(C_{13} + C_{44})}{C_{11}}k^2 - k^2_{L(11)} > 0, \quad \frac{C_{33}m - (C_{13} + C_{44})}{C_{44}m}k^2 - k^2_{T(44)} > 0. \qquad (83)$$

Let us recall that the similar conditions for the case of isotropic medium $k^2 - k^2_L > 0, k^2 - k^2_T > 0$ are slightly simpler and coincide with the corresponding conditions of classical Rayleigh surface wave [5–9, 17]. A complexity of conditions (83) is increased by the complex form of dependence of constants n, m on the wave number k.

If the conditions (83) are fulfilled, then the solution of wave equations for potentials can be written in the form.

$$\widehat{\Phi}(r) = \widehat{A}_\Phi K_0(M_{L(11)}r), \quad \widehat{\Psi}(r) = \widehat{A}_\Psi K_1(M_{T(44)}r). \qquad (84)$$

With allowance for formulas (84), the representations of potentials becomes more definite

$$\Phi(r,z,t) = \widehat{A}_\Phi K_0(M_{L(11)}r)e^{i(kz-\omega t)}, \quad \Psi(r,z,t) = \widehat{A}_\Psi K_1(M_{T(44)}r)e^{i(kz-\omega t)}. \qquad (85)$$

The formula (85) completes the first analytical part of solving the problem on cylindrical surface wave.

3.5 Boundary conditions: equations for the unknown wave number

This part of analysis can be treated as the second analytical part. The boundary conditions have the form identical for all kinds of symmetry of properties. That is, they have the form (17) or (21). The formulas for stresses depend already on the symmetry of medium. The expressions for stresses through the potential reflect the features of introducing the potentials. In this case, they have the form

$$\sigma_{rr} = (\lambda + 2\mu)(\Phi_{,rr} - \Psi_{,rz}) + \lambda \left\{ \begin{array}{l} (1/r)(\Phi_{,r} - \Psi_{,z}) + \\ + n\Phi_{,zz} + m\Psi_{,rz} + m(1/r)\Psi_{,z} \end{array} \right\}, \qquad (86)$$

$$\sigma_{rz} = \mu \left[(\Phi_{,rz} - \Psi_{,zz}) + n\Phi_{,zr} + m\Psi_{,rr} + m(1/r)\Psi_{,r} - m(1/r^2)\Psi \right]. \qquad (87)$$

Further, the representations (86) and (87) should be substituted into the boundary conditions, and the formulas on differentiation of Macdonald functions [3] should be taken into account:

$$\left[dK_0(M_{L(11)}rx)/dr \right] = -M_{L(11)}K_1(M_{L(11)}rx),$$

$$\left[d^2K_0(M_{L(11)}r)/dr^2 \right] = M_{L(11)}(1/r)K_1(M_{L(11)}r) + (M_{L(11)})^2 K_0(M_{L(11)}r),$$

$$\left[dK_1(M_{T(44)}r)/dr \right] = -(1/r)K_1(M_{T(44)}r) - M_{T(44)}K_0(M_{T(44)}r).$$

Then the boundary conditions are transformed into the algebraic equations relative to quantities $K_1(M_{L(11)}r_o)\widehat{A}_\Phi, K_1(M_{T(44)}r_o)\widehat{A}_\Psi$

$$\left[M_{L(11)} \frac{1}{r_o} + \frac{v_L^2}{v_T^2} \left(\begin{array}{c} \left(M_{L(11)}\right)^2 - \\ -\frac{v_L^2 - v_T^2}{v_L^2} nk^2 \end{array} \right) \frac{K_0\left(M_{L(11)}r_o\right)}{K_1\left(M_{L(11)}r_o\right)} \right] \widehat{A}_\Phi K_1\left(M_{L(11)}r_o\right) - ik \frac{v_L^2 - v_T^2}{v_T^2}$$

$$\times \left[\begin{array}{c} \left(2(1-m) + \frac{v_T^2}{v_L^2 - v_T^2} \right) \frac{1}{r_o} + \\ + \left((1-m) + \frac{v_T^2}{v_L^2 - v_T^2} \right) M_{T(44)} \frac{K_0\left(M_{T(44)}r_o\right)}{K_1\left(M_{T(44)}r_o\right)} \end{array} \right] \widehat{A}_\Psi K_1\left(M_{T(44)}r_o\right) = 0,$$

$$(88)$$

$$(1+n)ik \frac{K_0\left(M_{L(11)}r_o\right)}{K_1\left(M_{L(11)}r_0\right)} K_1\left(M_{L(11)}r_o\right)\widehat{A}_\Phi + \left[m\left(M_{T(44)}\right)^2 + k^2 \right] K_1\left(M_{T(44)}r\right)\widehat{A}_\Psi = 0.$$

$$(89)$$

When the determinant of linear homogeneous system of Eqs. (88) and (89) is equaled to zero, then the equations for the unknown wave number can be obtained:

$$(1+n)k^2 \frac{v_L^2 - v_T^2}{v_T^2} \frac{K_0\left(M_{L(11)}r_o\right)}{K_1\left(M_{L(11)}r_0\right)} \left[\begin{array}{c} \left(2(1-m) + \frac{v_T^2}{v_L^2 - v_T^2} \right)(1/r_o) \\ + \left((1-m) + \frac{v_T^2}{v_L^2 - v_T^2} \right) M_{T(44)} \frac{K_0\left(M_{T(44)}r_o\right)}{K_1\left(M_{T(44)}r_o\right)} \end{array} \right]$$

$$- \left[m\left(M_{T(44)}\right)^2 + k^2 \right] \left[\begin{array}{c} M_{L(11)} \frac{1}{r_o} + \\ \frac{v_L^2}{v_T^2} \left(\left(M_{L(11)}\right)^2 - \frac{v_L^2 - v_T^2}{v_L^2} nk^2 \right) \frac{K_0\left(M_{L(11)}r_o\right)}{K_1\left(M_{L(11)}r_o\right)} \end{array} \right] = 0.$$

$$(90)$$

Note that the sufficiently complex expression relative to the wave number is hidden coefficients $M_{L(11)}, M_{T(44)}$ of Macdonald's functions $\frac{K_0\left(M_{L(11)}r_o\right)}{K_1\left(M_{L(11)}r_0\right)}, \frac{K_0\left(M_{T(44)}r_o\right)}{K_1\left(M_{T(44)}r_o\right)}$. Therefore, the analytical part of analysis is finished on these formulas. Further, the numerical approaches have to be utilized.

Note also that the simple and convenient condition from analysis of classical surface Rayleigh wave [6–10, 17], when the wave number depends only on ratio $\left(v_L^2/v_T^2\right)$, does not exist in the analysis of cylindrical surface wave. Here, the parameters $M_{L(11)}, M_{T(44)}$ depend on the complicated form on all elastic constants. Of course, the Macdonald functions can be represented approximately through their arguments. But only the numerical methods can give the final result—the value of wave number or phase velocity.

4. Solving the problem on propagating in the direction of symmetry axis surface wave within the framework of linearized theory of elasticity with allowance for initial stresses

Note that analysis of cylindrical surface wave in isotropic medium was first carried out by Biot [1] in 1952 and the transversally isotropic medium with initial stresses was first carried out by Guz et al. in 1974 [18].

Let us show below an analysis of the problem in hand that is carried out in Subchapter "Longitudinal Waves" of Chapter 4 "Waves in Cylindrical Media" of volume 2 of edition [19]. Here, the cylinder of circular cross-section is considered, and the longitudinal wave is defined as the wave propagating in the direction of cylinder axis Oy_3. The problem is assumed to be axisymmetric and is described within the framework of linearized theory of elasticity for bodies with initial stresses. The cylindrical coordinates (r', θ, y_3) are introduced, and displacements are taken in the form

$$u_{r'} = u_{r'}(r', y_3, t), \quad u_\theta = 0, \quad u_{y_3} = u_{y_3}(r', y_3, t) \tag{91}$$

The medium is assumed isotropic or transversally isotropic. The main relations for transversal isotropy are described by independent constant

$$\omega_{1111}, \omega_{1122}, \omega_{1133}, \omega_{1221}, \omega_{1313}, \omega_{1331}, \omega_{3113}, \omega_{3333}. \tag{92}$$

Note that as shown in (92), eight constants are necessary in the linearized theory, but in the framework of linear theory, they have the form (33), and their number is five.

Further, the general solutions of basic equations in displacements are utilized. These equations have the form (3.174) [19]

$$\omega_{lma\beta}(\partial^2 u_\alpha / \partial x_k \partial x_\beta) = \rho \delta_{ma}(\partial^2 u_\alpha / \partial \tau^2) \tag{93}$$

where only eight independent constants (92) must be taken into account.

The corresponding equations of linear theory of elasticity for the case of transversally isotropic medium without of initial stresses are written above as Eqs. (45) and (46).

The general solutions for the case of axial symmetry are expressed through one potential in the form (4.13) [19]

$$u_{r'} = -(\partial^2 / \partial r' \partial y_3) X', \tag{94}$$

$$u_3 = (\omega'_{1111} + \omega'_{1313})^{-1} [\omega'_{1111} \Delta'_1 + \omega'_{3113}(\partial^2 / \partial y_3^2) - \rho'(\partial^2 / \partial \tau^2)] X',$$
$$\Delta' = (\partial^2 / \partial r'^2) + (1/r')(\partial / \partial r').$$

Note that in Section 3 of this chapter, two potentials Φ, Ψ are introduced by formula (57), which corresponds and generalizes the procedure used in Biot's analysis [1].

The longitudinal harmonic wave is described analytically through the potential in the form (101) [19]

$$X'(r', y_3, \tau) = X'_{(1)}(r') e^{i(ky_3 - \omega\tau)}, \tag{95}$$

where the unknown amplitude $X'_{(1)}(r')$ has to be determined by substitution of solution (4.13) [19] into the second Eq. (3.362) [19] (for potential X'). This gives Eq. (4.16) [19]:

$$\left\{ (\omega'_{1111}\omega'_{1331})(\Delta'_1 - k^2\xi'_2 2)(\Delta'_1 - k^2\xi'_3 2) \right.$$
$$\left. -k^2\rho' C_{cp}^2 [(\omega'_{1111} + \omega'_{1331})\Delta'_1 - k^2(\omega'_{1111} + \omega'_{3113})] + \rho'^2 C_{cp}^2 \right\} X'_{(1)} = 0, \tag{96}$$

$$C_{cp} = \omega/k, \quad \xi_{2,3}'^2 = c' \pm \sqrt{c'^2 - (\omega_{3333}'\omega_{3113}'/\omega_{1111}'\omega_{1331}')},$$

$$c' = (1/2) \begin{bmatrix} (\omega_{3333}'/\omega_{1331}') + (\omega_{3113}'/\omega_{1111}') \\ -\left((\omega_{1111}' + \omega_{1331}')^2/\omega_{1111}'\omega_{1331}'\right) \end{bmatrix},$$

which further is written in the form

$$\left(\Delta_1' - \zeta_2'^2\right)\left(\Delta_1' - \zeta_3'^2\right) = 0 \tag{97}$$

The unknown quantities $\zeta_{2,3}'$ must be found from the linear algebraic equation of the fourth degree (4.20) [19].

$$\omega_{1111}'\omega_{1331}'(\zeta')^4 + k^4\left(\rho'C_{cp}^2 - \omega_{3333}'\right)\left(\rho'C_{cp}^2 - \omega_{3113}'\right)$$
$$+ k^2\begin{bmatrix} \omega_{1111}'\left(\rho'C_{cp}^2 - \omega_{3333}'\right) + \omega_{1331}'\left(\rho'C_{cp}^2 - \omega_{3113}'\right) \\ +(\omega_{1111}' + \omega_{3113}')^2 \end{bmatrix}(\zeta')^2 = 0, \tag{98}$$

The solution (95) describes the surface wave, if amplitude $X_{(1)}'(r')$ attenuates with increasing the radius. This is provided by the condition that quantities $\zeta_{2,3}'$ is unequal and pure imaginary. Then the potential gains the form (4.22) [19].

$$X_{(1)}'(r') = B_{10}J_0\left(|\zeta_2'|r'\right) + B_{20}K_0\left(|\zeta_2'|r'\right) + B_{30}J_0\left(|\zeta_3'|r'\right) + B_{40}K_0\left(|\zeta_3'|r'\right), \tag{99}$$

The shown part of analysis from introducing the potential by formula (94) to representation of solution by formula (99) inclusive can be compared with analogous part of analysis from Section 3 of this chapter (from introducing the potentials by formula (57) to the solution in the form of (85)). It is easy to see a difference in representations (99) and (85): formula (99) uses the Bessel functions and in particular the Macdonald function of zero index, whereas formula (85) uses (like the Biot's solution (14)) the Macdonald functions (16) of the zero and first indexes.

The next part of analysis of cylindrical wave consists in substitution of solution into boundary conditions of the form (99) [19]

$$Q_{r'r'}' = 0, \quad Q_{r'3}' = 0 \text{ when } r' = R_1', R_2'. \tag{100}$$

The case of oscillatory behavior of wave in the direction of radius is considered with pointing that the case of surface wave is the same type. A substitution of solution (99) into conditions (4.79) [19] gives the dependence of velocity of surface wave or its wave number on frequency—a dispersion equation in the form of determinant of the fourth order in the form (4.26) [19].

$$\det|\alpha_{ij}| \equiv \Delta(\omega, k) = 0; \quad i, j = 1, 2, 3, 4. \tag{101}$$

This finishes the analytical part of analysis shown in [19]. It corresponds to the part of Section 3.5 of this chapter, where the explicit form of dispersive equations is proposed in the form (90) that includes the Macdonald functions of the zero and first orders which represent some generalization of dispersion Eq. (27) obtained by Biot.

5. Conclusions

This chapter proposes three fragments of analytical analysis of the cylindrical surface wave propagating in the vertical direction of circular cylindrical cavity. The

first fragment shows the analytical part of pioneer work of Biot. It represents the classicism of mathematical procedures and physical comments of Biot. Properly speaking, the clear and understandable Rayleigh's scheme is saved, but it is complemented by some findings reflecting the features of cylindrical waves. Two next fragments show the more late development of the Biot's problem. They are different by influence of the Biot's procedure. The approach shown in Section 3 is more close to the Biot's analytical scheme, whereas Section 4 proposes as an independent scheme that is more close to the Rayleigh scheme. Nevertheless, all fragments testify the mathematical complexity in solving the problem on the cylindrical surface waves. Thus, revisiting the old Biot's problem shows that it still generates new scientific and practical problems.

Author details

Jeremiah Rushchitsky
S.P. Timoshenko Institute of Mechanics, Kyiv, Ukraine

*Address all correspondence to: rushch@inmech.kiev.ua

IntechOpen

References

[1] Biot MA. Propagation of elastic waves in a cylindrical bore containing a fluid. Journal of Applied Physics. 1952;**23**(9):997-1005. DOI: 10.1063/1.1702365

[2] Achenbach JD. Wave Propagation in Elastic Solids. Amsterdam: North-Holland; 1973. 425 p

[3] FWJ O, Lozier DW, Bousvert RF, Clark CW, editors. NIST (National Institute of Standards and Technology). Handbook of Mathematical Functions. Cambridge: Cambridge University Press; 2010. 968 p

[4] Rushchitsky JJ. Nonlinear Elastic Waves in Materials. Series: Foundations of Engineering Mechanics. Heidelberg: Springer; 2014. 455 p. DOI: 10.1007/978-3-319-00464-8

[5] Sedov LI. A Course in Continuum Mechanics. Vol. I-IV. Amsterdam: Wolters Noordhoff Publishing; 1971

[6] Viktorov IA. Rayleigh and Lamb Waves. NY: Plenum Press; 1967. 168 p

[7] Nowacki W. Theoria sprazystosci. Warszawa: PWN; 1970. 769 p (in Polish)

[8] Rushchitsky JJ, Tsurpal SI. Waves in Materials with Microstructure. Kiev: S. P. Timoshenko Institute of Mechanics; 1998. 377 p (in Ukrainian)

[9] Fedorov FI. Theory of Elastic Waves in Crystals. NY: Academic Press; 1975. 388 p

[10] Dieulesaint E, Royer D. Ondes elastiques dans les solides. Application au traitement du signal. Paris: Masson et Cie; 1974. 424 p (in French)

[11] Royer D, Dieulesaint E. Elastic Waves in Solids. Vols. I and II. Advanced Texts in Physics. Berlin: Springer; 2000

[12] Lekhnitsky SG. Theory of Elasticity of Anisotropic Elastic Body. San Francisco: Golden Day Inc; 1963. 404 p

[13] Kiselev AP. Rayleigh wave with a transverse structure. Proceedings of the Royal Society of London. Series A. 2004;**460**(2050):3059-3064. DOI: 10.1098/rspa.2004.1353

[14] Guz AN, Rushchitsky JJ. Short Introduction to Mechanics of Nanocomposites. Rosemead, CA: Scientific & Academic Publishing; 2013. 280 p

[15] Cheng M, Chen W. Weerasoorlya Mechanical properties of Kevlar ® KM2. Journal of Engineering Materials and Technology. 2005;**127**(2):197-203. DOI: 10.1115/1.1857937

[16] Elliot HA. Three-dimensional stress distribution in hexagonal aelotropic crystals. Mathematical Proceedings of the Cambridge Philosophical Society. 1948;**44**(4):522-533. DOI: 10.1017/50305004100024531

[17] Rushchitsky JJ. Theory of Waves in Materials. Copenhagen: Ventus Publishing ApS; 2011. 270 p. DOI: 10.13140/RG.2.1.3162.8647

[18] Guz AN, Kushnir VP, Makhort FG. On propagation of waves in cylinders with initial stresses. Izvestiya, Academy of Sciences, USSR. Seriya Mekhanika Tverdogo Tiela. 1974;**5**:67-74 (In Russian)

[19] Guz AN. Elastic Waves in Bodies with Initial Stresses. 2 Vols. Naukova Dumka: Kiev; 1986. 376 and 536 p (in Russian)

Chapter 3

Appearance of Catastrophes and Plasticity in Porous and Cracked Media

Boris Sibiryakov

Abstract

This chapter is devoted to study the properties of structured continuum, with specific surface and characteristic size of structure. This linear dimension means the absence of automatic transforming difference relations into differential equations. It is impossible to apply conservation laws at any point of the real structural body, because any closed points in vicinity of inner surface can represent both solid and liquid (gas) phases. We need use some representative minimal volume, which characterized the complicate body at hole. This approach leads to differential equations of motion of the infinite order. Solutions of them, along usual P and S waves, contain many waves with abnormally low velocities, which are not bounded below. It is shown that in such media, weak perturbations can increase or decrease without limit. The reason of the infinite order of differential equations is many degrees of freedom in such media. Catastrophes correspond to unstable solutions equations of motion. Plasticity begins in elastic state like continuous phenomenon, and there is a finite distance between the sliding lines on the contrary with classic plasticity, where distances between sliding lines are infinitely small.

Keywords: structure of pore space, porous and cracked media, instability, plasticity

1. Introduction

The main idea of continuous mechanics is that any volume is the representative one. It means that the integral of loadings, which concentrates on the surface and bounds mentioned volume, is equal to zero in statics or to inertial forces in dynamics. The evident disagreement that the surface forces and inertial ones apply to different points (inertial forces apply to center of gravity of volume) overcomes due to an assumption about infinite small sizes of the mentioned volume. This assumption gives us a possibility to equal the volume forces (divergence of the stress tensor), which was created by the internal stresses, and the inertial forces, according to the second Newton law. Mathematical technique is based on the Gauss theorem about relation between the field flux across surface and divergence of this field in the volume, which is bounded by closed surface. However, in the structured bodies, there is a fundamentally different situation. The representative volume must contain some set of elementary structures. Otherwise, a small volume will contain only one of the phases, for example, liquid in the pores or the solid skeleton without liquid, and will not characterize the properties of the structured body. The

characteristic size of the structure leads to fact that the average distance is between one of the cracks to another and one pore to another given by the specific surface of the sample. It is necessary to connect the integral geometric properties of a medium with physical processes of such bodies deforming. On the contrary with a classic continuum of Cauchy and Poisson, the new continuum for structured or blocked media must contain many degrees of freedom. It is evident because elementary blocks may translate the motion by contact interactions, by rotations, and by group of particle's motion. It means that the energy contents not in first derivatives (strains) only. The potential energy contents in the second derivatives (curvatures) and other orders of ones. It means that the equation of motion of a blocked medium should contain many derivatives; in other words, the equation of motion may have been very high, probably, the infinite order. The static and dynamic processes in the classic continuum are divided by the Great Wall of China from each other. The equation of equilibrium never will pass in the equation of motion. However, it is evident that the dynamic processes often arise very slow and are quasi-static motions. It would be nice to destroy this mentioned wall by a newly structured continuum. It would be a good idea to destroy the abovementioned wall by means of justification of the newly structured continuum. The seismic emission, which causes due to static loading, maybe not a bad example of such phenomena, which are existed between statics and dynamics.

2. Equations of motion for structured media

In **Figure 1**, an element of the volume of structured body is shown, in which l_0 is the average distance between one pore and another. Earlier presented was the result about the relation between the specific surface and the average length between cracks and pores. There is a theorem of integral geometry, which relates the specific surface σ_0 and l_0, namely [1]

$$\sigma_0 l_0 = 4(1-f) \tag{1}$$

where f is the porosity. Hence, if there is a specific surface of sample, there is automatically the average range of microstructure l_0.

The distinction between classic and structured continuums is clear, see **Figure 1**. In the volume, which is inside into surface C, there is equation of equilibrium, because all forces delete to each other. In the volume, which is inside into surface D, there is equilibrium, because forces do not compensate to each other (on the one
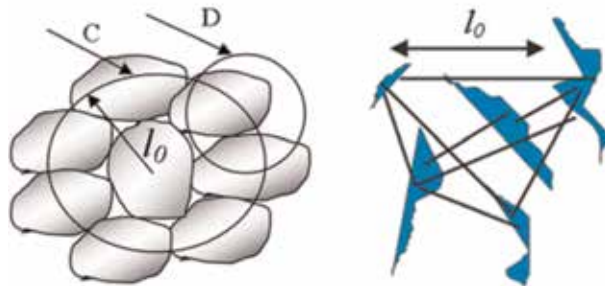
Figure 1.
Representative element of structured body for granular medium (left) and average distance l_o from one crack to another (right). On surface C, the equation of equilibrium is complied, and on surface D, it is not satisfied.

side of grain, we have forces; and on the other part of boundary surface D, we have no forces).

The idea of creation of the new model of space is as follows: consider some finite volume of the body (a sphere on a figure with radius l_0). Surface forces act on a sphere of radius l_0, while inertial forces applied at the center of the structure. There is no way for the volume element to tend to zero and to match the points of application of surface forces and inertial forces, as in the classical continuum. Therefore, since we must consider the representative finite volume, we have a problem of different positions of surface and inertial forces.

We need to translate the surface forces to the center of the structure by a special operator, and after this, it is possible to apply the law of conservation for some structural image continuum and to act as in a typical classical model of space. The main feature of this approach is to fill all the space, including the pores and cracks by field force. Because of it, we have a continuous image of a very complex media and a possibility to apply the physical laws into an image of the media.

The one-dimensional operator of field translation from point x into point $x \pm l_0$ is given by the symbolic formula [1]

$$u(x \pm l_0) = \exp(l_0 D_x) \tag{2}$$

The operator is $D_x = \frac{\partial}{\partial x}$. The difference operator $\Delta_1(x)$ is a difference between two translation operators

$$\Delta_1 = \frac{1}{l_0}\left[u\left(x + \frac{l_0}{2}\right) - u\left(x - \frac{l_0}{2}\right)\right]$$

$$= \frac{u(x)}{l_0}\left[\exp\left(\frac{l_0}{2}D_x\right) - \exp\left(-\frac{l_0}{2}D_x\right)\right] = u(x)\frac{\sinh\left(\frac{l_0}{2}D_x\right)}{\left(\frac{l_0}{2}\right)} \tag{3}$$

This is a first difference for finite distance between two points. The second difference may be represented as quadrate of the first difference,

$$\Delta_2 = u(x)\frac{\sinh\left(\frac{l_0}{2}D_x\right)^2}{\left(\frac{l_0}{2}\right)^2} \tag{4}$$

The formally expansion in Taylor's series gives a finite increment of field. This expansion contains the infinite number of derivatives with different powers of l_0. The factor l_0 relates with the specific surface of the sample. The three-dimensional operator of field's translation for some cube with length of l_0 may be constructed as follows:

$$P[u(x)] = \frac{u(x)}{6}\left[\cosh\left(\frac{l_0}{2}D_x\right) + \cosh\left(\frac{l_0}{2}D_y\right) + \cosh\left(\frac{l_0}{2}D_z\right)\right] \tag{5}$$

The analogous operator of translation for some spheres is given by expression

$$P(l_0 D_x; l_0 D_y; l_0 D_z) = \frac{1}{4\pi}\int_0^{2\pi}\int_0^{\pi} \exp\left[l_0\left(D_x sin\theta cos\varphi + D_y sin\theta sin\varphi + D_z cos\theta\right)\right] sin\theta d\theta d\varphi \tag{6}$$

Because there is a Poisson formula [2]

$$\int\limits_{0}^{2\pi}\int\limits_{0}^{\pi} f[(\alpha sin\theta cos\varphi + \beta sin\theta sin\varphi + \gamma cos\theta)]sin\theta d\theta d\varphi = 2\pi \int\limits_{0}^{\pi} f(Rcosp)sinpdp = 2\pi \int\limits_{-1}^{1} f(Rt)dt$$

(7)

In the formula (7), parameters $\alpha, \beta,$ and γ are some quantities. However, in Eqs. (6) and (7), parameters play the role of differential operators. The relation between quantities and operators is established by Maslov [3]. Hence, P operator maybe rewritten as follows [4]

$$P(l_0 D_x; l_0 D_y; l_0 D_z) = \frac{1}{2}\int\limits_{-1}^{1} \exp\left(l_0\sqrt{\Delta}, t\right)dt = \int\limits_{0}^{1} \cosh\left(l_0\sqrt{\Delta}, t\right)dt$$

$$= \frac{\sinh\left(l_0\sqrt{\Delta}\right)}{l_0\sqrt{\Delta}} = E + \frac{l_0^2}{3!}\Delta + \frac{l_0^4}{5!}\Delta\Delta + ...$$

(8)

In the classic continuum, we apply the impulse conservation law to any element of the medium. In this situation, we need to fill all pores over space by a force field. Instead of real stresses, which are changing very fast from one point to another, we can construct the continual image of real stresses. Namely, we use a continuous field, which is constructed by the application of the operator P to the real complicated force field. For this continuous image of real stress, $P(\sigma_{ik})$, we can apply the impulse conservation law. In the classic continuous model, this operation is made by nature itself. This model of a continuum requires some mathematical operations in order to create the continuum medium. Using operator P, we can write the equation of motion of micro-inhomogeneous body, because for an average stresses in structure, the law of impulse conservation takes the usual form, namely [4]

$$\frac{\partial}{\partial x_k}[P(\sigma_{ik})] = \rho\ddot{u}_i$$

(9)

In a more detailed form Eq. (9) can be rewritten as follows

$$\frac{\partial}{\partial x_k}\left[\left(E + \frac{l_0^2}{3!}\Delta + \frac{l_0^4}{5!}\Delta\Delta + ...\right)\sigma_{ik}\right] = \rho\ddot{u}_i$$

(10)

No wonder that Eq. (9) contains derivatives of the infinite order. This circumstance is due to many degrees of freedom for structured bodies. At $l_0 \to 0$, we have the usual equations of motion for classic continuous model of space.

3. Fundamental solutions

We can pass to the image space, following Hooke's law and applying the Fourier transform along three coordinates, as [5]

$$u_i(x, y, z) = \frac{1}{(2\pi)^3}\iiint\limits_{-\infty}^{\infty} \exp\left[i\left(n_x x + n_y y + n_z z\right)\right]U_i\left(n_x, n_y, n_z\right)dn$$

(11)

where $n^2 = n_x^2 + n_y^2 + n_z^2; dn = dn_x dn_y dn_z$. The operator P leads to

$$Pu_i(x,y,z) = \frac{1}{(2\pi)^3} \iiint\limits_{-\infty}^{\infty} \frac{\sinh(l_0 n)}{l_0 n} \exp\left[i(n_x x + n_y y + n_z z)\right] U_i(n_x, n_y, n_z) dn \quad (12)$$

This allows us to calculate the Fourier transform for the fundamental solution of the system Eq. (9):

$$G_{ij} = \frac{1}{\mu n^2 - \rho\omega^2 \frac{l_0 n}{\sin(l_0 n)}} \left[\delta_{ij} - \frac{(\lambda+\mu)n_i n_j}{(\lambda+2\mu)n^2 - \rho\omega^2 \frac{l_0 n}{\sin(l_0 n)}} \right] \frac{l_0 n}{\sin(l_0 n)} \quad (13)$$

At very small values, $l_0 n$, the sine and argument ratio approaches unity, and the Fourier transform becomes an ordinary equation for Green's tensor in an elastic continuum. The inverse Fourier transform is obtained by integration of Eq. (13) which includes simple poles corresponding to P and S waves and a set of simple poles where the sine in the denominator of Eq. (13) becomes zero. The residuals are in the simple poles, $n^2 = k_S^2 l_0 n$, where k_S^2 is the wave number of both P and S waves. At very small l_0, the ratio $\frac{l_0 n}{\sin(l_0 n)} \to 1$ and denominators in Eq. (13) become the classical equations that define the poles corresponding to compression and shear waves velocities (**Figure 2**). Assuming $n/k_s = m$ and $k_s l_0 = \varepsilon$, we obtain the equation for complex roots that describe waves from a focused source in porous and cracked solids as
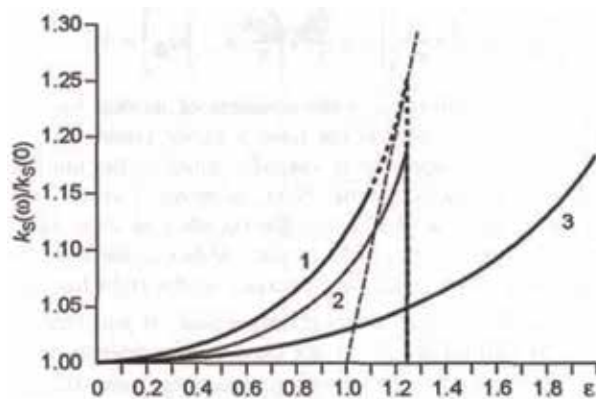
$$msin(\varepsilon m) = \varepsilon \quad (14)$$

If $m = x + iy$ is assumed to be a complex value, for the real and imaginary parts, we have the transcendental equations

$$xsin\varepsilon x cosh\varepsilon y - ysinh\varepsilon y cos\varepsilon x = \varepsilon^2$$
$$ysin\varepsilon x cosh\varepsilon y + xsinh\varepsilon y cos\varepsilon x = 0 \quad (15)$$

We can rewrite Eq. (15) in a different form with $x^* = \varepsilon x$ and $y^* = \varepsilon y$ as new variables

$$\frac{\tan x^*}{x^*} = -\frac{\tanh y^*}{y^*}; \quad \sin^2 x^* + \sinh^2 y^* = \frac{\varepsilon^4}{x^{*2} + y^{*2}} \quad (16)$$
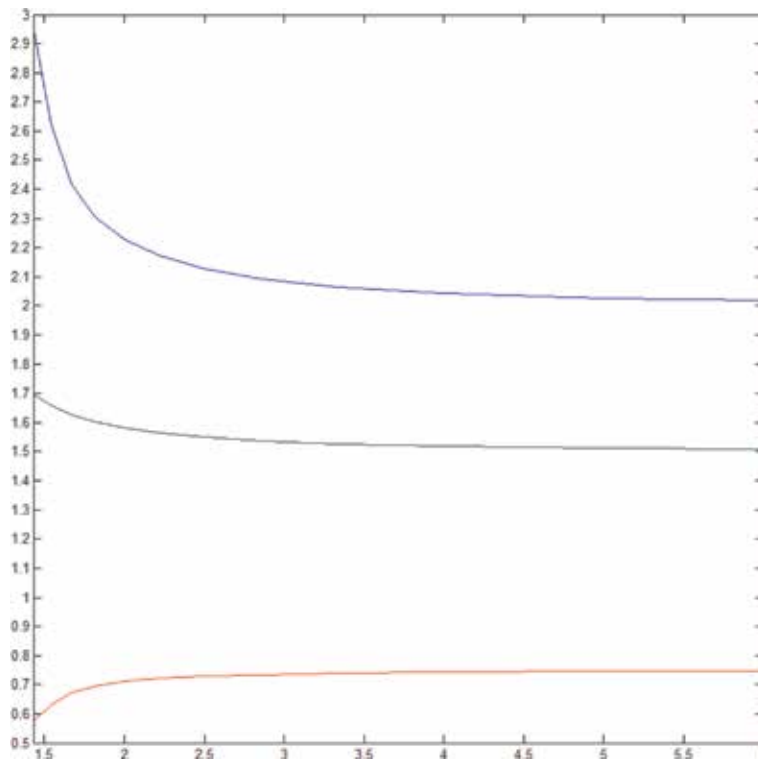

Figure 2.
Wave number ratio as a function of dimensionless ratio $\varepsilon = 2\pi l_o/\lambda_s$. Curves: 1—wave number ratio $k_s(\omega)/k_s(0)$, i.e., S-wave velocity decreasing with frequency; 2—$\gamma = V_s/V_p$ increasing with frequency; and 3—wave number ratio $k_s(\omega)/k_s(0)$ of P waves.

Equation (15) obviously has many real roots corresponding to $y = 0$. Indeed, at small ε, Eq. (15) gives the solution $m = 1$, which corresponds to the ordinary P- or S-wave velocity. At large values of m, Eq. (15) is satisfied only if εm approaches a value divisible by n, i.e., at near-zero sine that defines the characteristic anomalous velocity. The unbounded value of the wave number means that normal P and S waves coexist with arbitrarily small P and S velocity anomalies. The existence of these anomalies in a micro-heterogeneous medium has its physical explanation: energy is stored in strain (first derivatives of displacement) as well as in the curvature of higher derivatives. Therefore, there appear as velocities related to flexural and torsion waves and to numerous waves associated with oscillation of groups of particles (blocks) (**Figure 3**).

The growing of ratio $\gamma = V_S/V_P$ causes a very interesting phenomenon, namely an apparent negative Poisson value, for waves with the length not very small compared to size of a grain. The growing value of $\gamma = V_S/V_P$ means that the Poisson ratio is decreasing up to negative values [6] (**Figure 4**).

At the same time, Eqs. (14) and (15) likewise have complex roots. The first Eq. (15) shows that complex roots arise only at some values of e, which are not so small, as they satisfy the inequality $\varepsilon x > \pi/2$. **Table 1** lists complex roots corresponding to some relatively small ε. Note that the parameter ε can be expressed via the linear size-to-wavelength ratio (l_0/λ_s).

Complex roots can mean either damping or unlimited growth of wave amplitude, of course, in the presence of an energy-unbounded source. The minimum damping (growth) corresponds to $(2.0288)^{-1}$ or about a half of the normal velocity. The same process can be expected to cause both excitation and damping in porous and cracked media, depending on the phase of stationary oscillations.

Figure 3.
The decreasing P-wave velocity (the upper line) and S-wave velocity (the middle curve) and the growth of their ratio $\gamma = V_S/V_P$ (the lower line) due to increasing size of microstructure. The ratio $\gamma = V_S/V_P$ more than 0.705 corresponds to the negative Poisson ratio [6]. The vertical scale is the wave velocities (km/s) and a horizontal scale is the ratio between the size of the microstructure and wavelength.
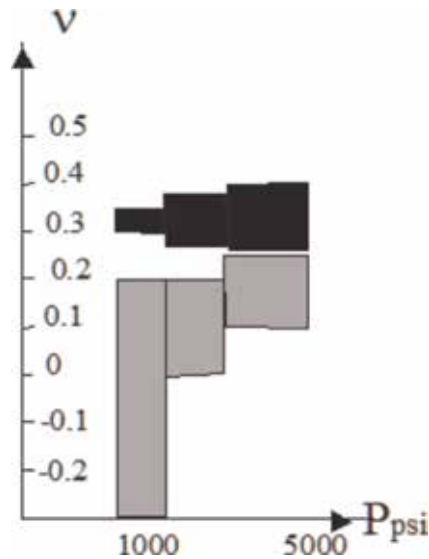
Figure 4.
Gregory experimental data. Poison ratio (the vertical axis) versus pressure. Black color corresponds to water saturated porous shales and gray color corresponds to dry shales with the same porosity. In this case, negative Poisson ratios are possible.

ε	x	y
0.2147	2.0288	0.0548
0.2507	2.0645	0.5838
0.2771	2.1064	0.8880
0.3253	2.1560	1.1838
0.3918	2.2157	1.5122

Table 1.
The value epsilon means dimensionless product of structure size into wavenumber of usual S waves in continuous medium. Value x means the real value of product of structural wavenumber into structure size. Value y is the imaginary part of it.

4. One-dimensional case: plane wave and instabilities

In one-dimensional case, the Eq. (10) takes more simple expression

$$u'' \left(E + \frac{l_0^2}{3!}\Delta + \frac{l_0^4}{5!}\Delta\Delta + ... \right) + k_S^2 u = 0 \qquad (17)$$

This equation by substitution $u = \exp(ikx)$ gives us the dispersion equation for an unknown wave number k, or for unknown wave velocity, which depends on the size of structure l_0 or specific surface of sample σ_0:

$$\frac{\sin(kl_0)}{kl_0} = \frac{k_S^2}{k^2} \qquad (18)$$

It is evident that by $l_0 \to 0$, the wave number $k \to k_S$, i.e., the wave velocity is equal to V_P or V_S, elastic wave velocity. However, if l_0 is not a very small value, the wave velocity decreases up to zero by $kl_0 \to m\pi$, if m is the integer number. Hence, this model describes along with usual seismic waves many waves of very small velocities, which are not bound below.

This effect is more for *P* waves than for *S* ones. Eq. (14) shows that if the Poisson ratio is measured on samples by velocities V_P and V_S, their ratio V_S/V_P grows by growing l_0, and this effect can produce abnormally small Poisson's ratio, up to negative volume of it.

It is evident that at $kl = m\pi$, m is the integer number and the value $k \to \infty$. It means that there are waves with arbitrary small velocities not bounded below. Beside it, Eq. (15) has complex roots too, because $\sin(kl_0)$ may be negative, while the second term in Eq. (18) contains $(k_S/k)^2$. Eq. (18) means that the complex roots do not by small values of x, because the right-hand expression is a negative value. In order to be complex roots, an evident condition is necessary, i.e., $tan x > \pi/2$. The physical sense of it means that the complex roots are possible, if the wavelength is four times (or more than four times) more than the size of the structure. These complex roots mean that amplitude of oscillations may be increasing or decreasing up to infinity or, may be, to zero. These roots are responsible for catastrophe's behavior of structured bodies.

Hence, if there is a source of sufficient energy, even some small oscillations can produce catastrophes. It is interesting that nonlinear deforming of samples decreases this effect, because a wave velocity for rocks is decreasing, by growing amplitude of wave. It means that the wave number is growing by the same frequency in the pure elastic process. In **Figure 6**, the real roots of dispersion, Eq. (18) are shown. The vertical axis shows a dimensionless frequency, namely ε, while horizontal axis shows us the real and imaginary parts of wave numbers. In **Figures 5–7** [7], complex roots as a function of dimensionless frequency ε are shown. Every point is a position of some root, namely a real part, an imaginary one, and a dimensionless frequency. The more is the spreading of ε values, the greater is the number of complex roots.
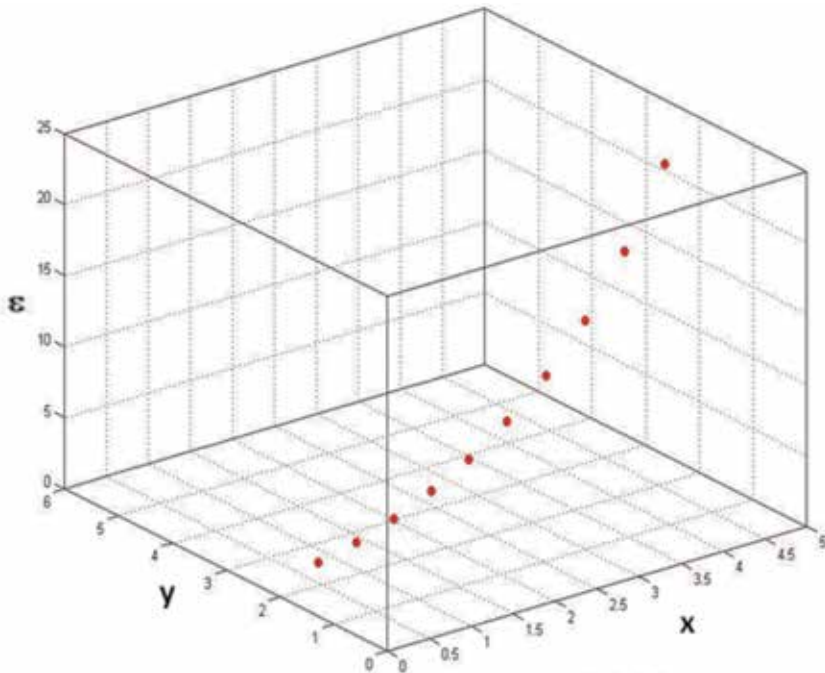
Figure 5.
*The position of complex roots depends on the value ε. The more the value ε, the more numbers of roots. The first value of ε corresponds to values of first row from **Table 1**.*
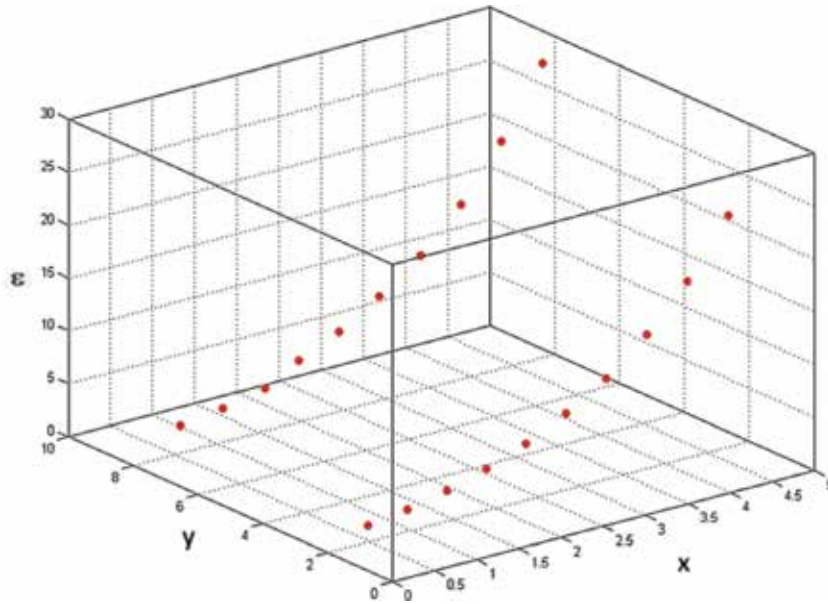
Figure 6.
The position of complex roots depends on the value ε. The more the value ε, the more numbers of roots. The second value of ε corresponds to values of second row from **Table 1**.
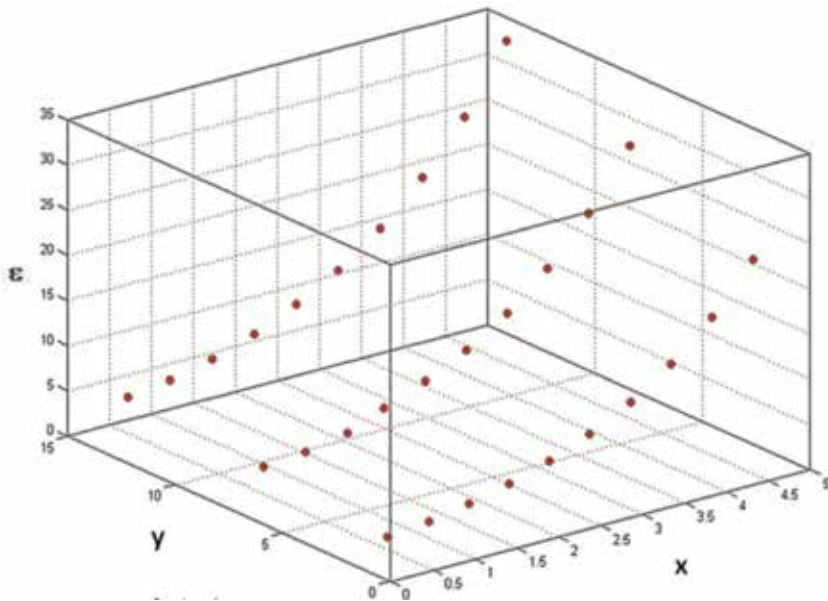
Figure 7.
The position of complex roots depends on the value ε. The more the value ε, the more numbers of roots. The third value of ε corresponds to values of third row from **Table 1**.

5. Pointing vector and equation of equilibrium for blocked media

The equation of equilibrium for micro-structured media can be written from Eq. (9) as

$$\frac{\partial}{\partial x_k}[P(\sigma_{ik})] = P\left[\frac{\partial\sigma_{ik}}{\partial x_k}\right] = 0; \ \frac{\partial\sigma_{ik}}{\partial x_k} = P^{-1}(0) \tag{19}$$

The inverse operator $P^{-1}(0)$ contains zero, but not zero only. It contains some periodic functions and the average value equal to zero. For example, such construction satisfies to Eq. (19)

$$P\left\{\sum \text{Im}\left\{\exp\left[in\frac{\pi}{l_0}(k_1 x + k_2 y + k_3 z)\right]\right\}\right\} = 0 \tag{20}$$

If n is integer number, $k_1 = sin\theta cos\varphi; k_2 = sin\theta cos\varphi; k_3 = cos\theta$. Physical sense of it means that volume forces are equal to zero in average sense, not at any point. Using mentioned inverse operator, we can write the equilibrium equation for blocked media in the form

$$\frac{\partial\sigma_{ik}}{\partial x_k} = \phi\sigma_0^2\sigma_{ik}^0 u_k^0 \sum_{n=1}^{\infty} \text{Im}\left\{\exp\left[in\frac{\pi}{l_0}(k_1 x + k_2 y + k_3 z)\right]\right\} \tag{21}$$

In Eq. (21) σ_0^2 is a quadrat of specific surface; $\sigma_{ik}^0 u_k^0 = A_i^0$ is the pointing vector of usual continuous body, and ϕ is a dimensionless constant, which must be obtained. These values we can put as constants in small structure volume. The integration with respect to spherical angles gives us a result that the imaginary part of exponent is zero in average sense, namely

$$\frac{1}{4\pi}\int_0^{2\pi}\int_0^{\pi} \exp\left[\frac{\pi n}{l_0}i(xsin\theta cos\varphi + ysin\theta sin\varphi + zcos\theta)\right]sin\theta d\theta d\varphi$$

$$\int_0^{\pi} \exp\left(ir\frac{n\pi}{l_0}cosp\right)sinpdp = \frac{1}{2}\int_{-1}^{1} \exp\left(ir\frac{n\pi}{l_0}t\right)dt = \frac{l_0}{n\pi r}\sin\left(\frac{rn\pi}{l_0}\right) + i0 \tag{22}$$

Partial solution of Eq. (22) is a convolution of Green tensor with right hand of Eq. (21), that is,

$$u_i^1(x) = \phi\frac{1}{\mu}\sigma_0^2\sigma_{mk}^0 u_k^0(x)\text{Im}\iiint\Gamma_{mi}(x,y)\exp\left[ik_m(x_m - y_m)\right]dV_y \tag{23}$$

Taking into account that the sizes of area much more, than sizes of structure, the area of integration is the infinite large one. In this case, integral Eq. (13) practically is the Fourier transform of fundamental solution of usual elastic equilibrium equations

$$u_i^{1n}(x) = \phi\frac{1}{\mu}\sigma^2\sigma_{mk}^0 u_k^0(x)\left(\frac{l_0}{n\pi}\right)^2\left[\delta_{mi} - (1 - \gamma^2)k_m k_i\right]\exp\left[\frac{in\pi(k_l x_l))}{l_0}\right] \tag{24}$$

In Eq. (24) the imaginary part of the exponent is used. Hence, the additional value in average sense is equal to zero. Using relation Eq. (1) $\sigma_0 l_0 = 4(1 - f)$, we get a partial solution, which depends on porosity only

$$u_i^{1n}(x) = \phi\frac{1}{\mu}\sigma_{mk}^0 u_k^0(x)\left(\frac{4(1 - f)}{n\pi}\right)^2\left[\delta_{mi} - (1 - \gamma^2)k_m k_i\right]\exp\left[i\frac{n\pi(k_l x_l)}{l_0}\right] \tag{25}$$

If these indexes coincide, $i = m,$ we get

$$<u_i^{1n}(x)> = \frac{\phi}{\mu} U_{i0} \left(\frac{4(1-f)}{n\pi}\right)^2 \left[1 - \frac{1-\gamma^2}{3}\right] \exp\left[\frac{in\pi(k_l x_l))}{l_0}\right] \qquad (26)$$

Take into account that the average value of a quadrat of cosine is $<k_m k_i> = \frac{\delta_{km}}{3}$. There is a summation with respect to n, and U_{i0} is a Pointing vector for usual continuous model of the medium. This value is a small one of the second order compared to usual displacement, because a Pointing vector, divided on the shear module is order to strain, multiplied to size of structure l_0.

Strains. By differentiating of an integral Eq. (23) take into account that the main part of the field contains in fast changing exponent, not in Green tensor itself, i.e.,

$$u_{i,j}^1(x) \approx \frac{\phi}{\mu} \sigma^2 \sigma_{mk}^0 u_k^0(x) i k_j \mathrm{Im} \iiint \Gamma_{mi}(x,y) \exp\left[ik_l(x_l - y_l)\right] dV_y \qquad (27)$$

$$e_{ij}^{1n} = \frac{i}{2}\left(u_{i,j}^1 + u_{j,i}^1\right) = \frac{\phi}{2\mu} \sigma_{mk}^0 \frac{u_k^0(x)}{l_0} \frac{4}{\pi} 4(1-f)^2 \{ \left[\delta_{mi} - (1-\gamma^2)k_m k_i\right]k_j$$

$$+ \left[\delta_{mj} - (1-\gamma^2)k_m k_j\right]k_i \} \frac{1}{n} \exp\left[i\frac{n\pi(k_1 x + k_2 y + k_3 z)}{l_0}\right]$$

$$= \phi \frac{8\gamma^2}{3\pi\mu} \frac{1}{l_0} \left[U_{0i}k_j + U_{0j}k_i\right](1-f)^2 \frac{1}{n} \exp\left[i\frac{n\pi(k_l x_l)}{l_0}\right] \qquad (28)$$

According to Eq. (9) the additional dilatation is

$$\theta^{(n)} = \phi \frac{16\gamma^2}{3\pi\mu} \frac{1}{l_0} [U_{0n}](1-f)^2 \frac{1}{n} \exp\left[i\frac{n\pi(k_l x_l)}{l_0}\right] \qquad (29)$$

Let us integrate the normal component of the Pointing vector on the small sphere with radius r. This integral must be equal to density of potential energy E (divergence of Pointing vector) namely,

$$<U_{0n}> = \frac{E}{\sigma_0} = 4(1-f)El_0 \qquad (30)$$

The average value of fast-changing exponent in Eqs. (28) and (29) on spherical angles is

$$< \exp \frac{1}{n}\left[i\frac{n\pi(k_l x_l)}{l_0}\right]> = \frac{4(1-f)}{\pi n^2} \int_0^{n\pi} \frac{\sin x}{x} dx = \frac{4(1-f)}{\pi n^2} Si(n\pi) \qquad (31)$$

The additional dilatation due to randomly oriented volume forces (an average value of these forces is zero) may be written as

$$\theta = \phi \frac{16\gamma^2}{3\pi\mu} \frac{4(1-f)^3 E}{\pi} \sum_{n=1}^{\infty} \frac{Si(n\pi)}{n^2} \qquad (32)$$

In Eq. (32) the symbol $Si(n\pi)$ means an integral sine of argument $(n\pi)$. The left hand in Eq. (32) is an additional expansion or compression, so called as dilatancy. It depends on the potential energy of the continuous body E, which may contain shear energy only, but it produces additional expansion or compression. It is a quadrat effect too.

More strong effect is related with product of high-changing volume force (equal to zero in average) into displacement. This product in not equal to zero in average, because it contains a quadrat of high-changing sine, which is equal to number one third in three dimension space.

$$E_n = \phi \frac{1}{\mu} \sigma_{mk}^0 u_k^0(x) \left(\frac{4(1-f)}{n\pi} \right)^2 \left[\delta_{mi} - (1-\gamma^2) k_m k_i \right] \frac{1}{3} \, \phi \sigma_0^2 U_{0i} \qquad (33)$$

If indexes coincide, $m = i$, we get the additional potential energy, due to fluctuations

$$E_n = \frac{\phi^2}{3(\lambda + 2\mu)} \left[U_{01}^2 + U_{02}^2 + U_{03}^2 \right] \sigma_0^2 \left(\frac{4(1-f)}{n\pi} \right)^2 \qquad (34)$$

The summation with respect to index n from unit up to infinity gives

$$E = \frac{8\phi^2}{9(\lambda + 2\mu)} \sigma_0^2 \left[U_{01}^2 + U_{02}^2 + U_{03}^2 \right] (1-f)^2 \qquad (35)$$

In spite of a fact that the Pointing vector is the small value of more high order, than stresses, the high value σ_0^2 (quadrat of specific surface) in Eq. (35) can produce not small common effect. The indefinite factor ϕ depends on the real structure of pore space and macro-stress-strain state. However, in some simple situations, it can calculate elementary. For example, at rigid pressing of globe by spherical force (radial displacements are constants), the stress-strain state is a hydrostatic state in average, but not such state at any point. The compressional energy is proportional to compress module of skeleton and its volume plus the incompressibility of fluid and its volume, namely [8–11]

$$E = \left(\lambda + \frac{2\mu}{3} \right) \frac{\theta_1^2}{2} (1-f) + \rho c^2 \frac{\theta_0^2}{2} f \qquad (36)$$

Indexes unit and zero in Eq. (36) mean solid and liquid parameters. The dilatation of two-phase body gives by the formula

$$\theta = (1-f)\theta_1 + f\theta_0; \theta_0 = \theta_1 \qquad (37)$$

If we have uniform random distribution of phases, the average energy is

$$E = E_1(1-f) + E_0 f \qquad (38)$$

In Eq. (38) f is the porosity and E_1 and E_0 are the energies of solid and liquid. The dispersion of random value relates with random volume forces, i.e.,

$$[E_1 - (E_1(1-f) + E_0 f)]^2 (1-f) + f[E_0 - (E_1(1-f) + E_0 f)]^2 = (E_1 - E_0)^2 f(1-f) \qquad (39)$$

Equation (39) gives the additional energy for very simple macro-hydrostatic state in average. This is the additional of interphase acting. It is equal to additional energy, which is given by Eq. (15). It is reasonable that at unit or zero porosity, an additional energy is equal to zero. The second result is, if the phase energy is equal, the mentioned additional one is equal to zero too. Hence, the indefinite factor ϕ^2 given by the simple equation is

$$\frac{1}{\mu}|E_1 - E_0|\sqrt{f(1-f)} = \frac{8\phi^2}{9(\lambda + 2\mu)}\sigma_0^2 \left[U_{01}^2 + U_{02}^2 + U_{03}^2\right](1-f)^2 \qquad (40)$$

6. The arriving of plasticity

In spite of that, the additional average strains is small, does not means, that these strains are small in the any point of the volume. Equations (28) and (29) show that on the planes $k_1x \pm k_2y \pm k_3z = 2l_0q$ (q is an integer number), the exponent is not a highly changed value, because it is equal to1 or -1.

In plane situation, the role of these planes plays orthogonal lines $k_1x \pm k_2y = 2l_0q$.
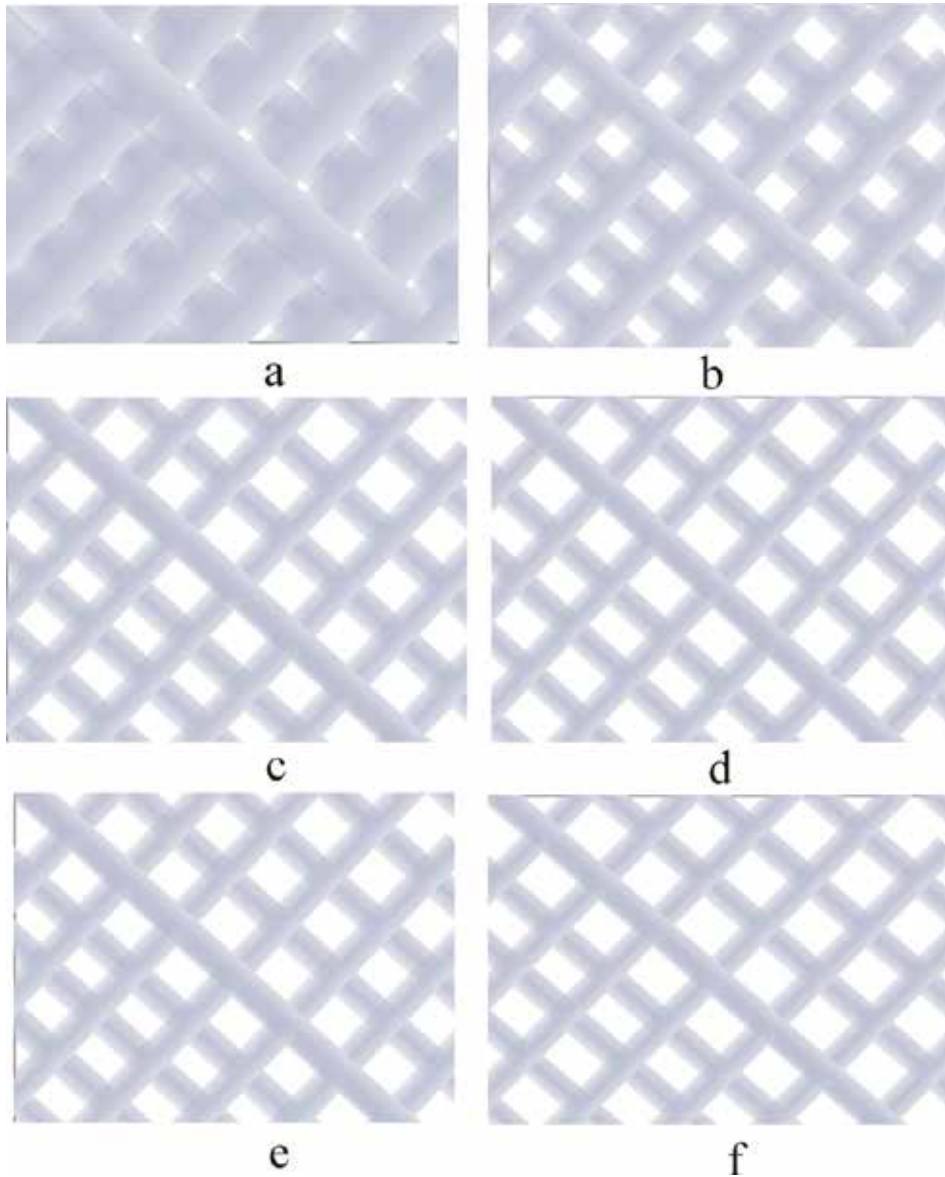
Figures 8.
Successive process of strains localization due to decreasing strains inside of quadrats, making orthogonal lines and increasing them near lines itself.

The series Eqs. (28) and (29) with respect to n in vicinity of mentioned planes are divergent (harmonic) series. It means that the field is decreasing inside of quadrats, making planes, and concentrating in vicinity of planes. Mentioned planes are analogs of slipping lines (lines of Luders) [12] in classic plasticity of the compressible medium. In practical, the number n in Eqs. (28) and (29) is bounded by the elastic limit of the second strain invariant. The field of strains is growing into planes (lines) and decreasing inside of them. This process is called as localization of strains. This localization begins in elasticity, with contrary of classic plasticity and elasticity. The other specific feature of this process is the finite distance between planes (lines). This distance is equal to l_0 (the inverse value of specific surface of sample), while in classic plasticity, this distance is infinitely small. The geological sense of it is interesting. In order to transform the matter from elasticity to plasticity, there is no necessary to have the plastic state at any point of the medium. Plasticity may concentrated near planes, and the other volume can be in elastic state. Rock may flow comparatively light, if they have pores and cracks. On the **Figure 8** shown successive process of localization of strains due to decreasing field inside of quadrats, making by orthogonal lines and increasing them near lines itself.

7. Conclusions

1. The model of the structured continuum with specific surface of the blocked medium or average size of structure, gives us the differential equations of motion of the infinite order. This model includes collective properties of pore space like the porosity and specific surface and predicts besides usual elastic waves many unusual waves with very small velocities.

2. This model predicts the decreasing of the Poisson ratio (up to negative values) due to finite size of microstructure. The reason for this is the decreasing of wave velocity with finite specific surface of the rock.

3. The localization of stresses and strains in structured media begins in elastic state of deforming.

4. The small areas of a stress-strain concentration looks like usual orthogonal sliding lines in classic plasticity. However, they have a finite effective thickness, which depends on the average size of the structure and the elastic strain limit. Besides, there is a finite distance between analogs of sliding lines, which is equal to the average distance from one pore to another one, or between cracks.

Author details

Boris Sibiryakov
Trofimuk Institute of Oil and Gas Geology and Geophysics SB RAS,
Novosibirsk State University, Novosibirsk, Russia

*Address all correspondence to: sibiryakovbp@ipgg.sbras.ru

IntechOpen

References

[1] Santalo L. Integral Geometry and Geometrical Probability. 2nd ed. Cambridge University Press; 2004. 405 p

[2] Gradshteyn IS, Ryzhik IM. Table of Integrals, Series, and Products. In: Zwillinger D, Moll V, editors. Academic Press; 2014. 1184 p

[3] Maslov VP. Operator Methods. Mir. 1976. 559 p

[4] Sibiryakov BP, Prilous BI. The unusual small wave velocities in structural bodies and instability of pore or cracked media by small vibration. WSEAS Transactions on Applied and Theoretical Mechanics. 2007;**7**:139-144

[5] Fokin AG, Shermergor TD. Theory of propagation of elastic waves in nonhomogeneous media. Springer Link. 1990;**25**(5):600-609

[6] Gregory AR. Fluid saturation effect on dynamic elastic properties of sedimentary rocks. Geophysics. 1976;**41**(5):895-921

[7] Sibiryakov BP, Prilous BI, Kopeykin AV. The nature of instability of Blocked Media and Distribution Law of Unstable States. Physical Mesomechanics. 2013;**16**:2:141-151. ISSN: 1029-9599

[8] Biot MA, Willis DJJ. Journal of Applied Mechanics. 1957;**24**:594-601

[9] Biot MA. General solution of the equations of elasticity and consolidation for a porous material. Journal of Applied Mechanics. 1941;**12**:155-164

[10] Gassman F. Uber die Elastizitat Poroser Medien: Vier. der Natur. Gesellschaft in Zurich. 1951;**96**:1-23

[11] Biot MA. Theory of propagation of the elastic waves in a fluid saturated porous solid. 1. Low-frequency range. The Journal of the Acoustical Society of America. 1956;**28**:168-178

[12] Kachanov LM. Fundamentals of the Theory of Plasticity. North-Holland Publishing Company, 1971. XIII, 482 p

Efficient Simulation of Fluids

Pierre Thuillier Le Gac, Emmanuelle Darles,
Pierre-Yves Louis and Lilian Aveneau

Abstract

Fluid simulation is based on Navier-Stokes equations. Efficient simulation codes may rely on the smooth particle hydrodynamic toolbox (SPH), a method that uses kernel density estimation. Many variants of SPH have been proposed to optimize the simulation, like implicit incompressible SPH (IISPH) or predictive-corrective incompressible SPH (PC-ISPH). This chapter recalls the formulation of SPH and focuses on its effective parallel implementation using the Nvidia common unified device architecture (CUDA), while message passing interface (MPI) is another option. The key to effective implementation is a dedicated accelerating structure, and therefore some well-chosen parallel design patterns are detailed. Using a rough model of the ocean, this type of simulation can be used directly to simulate a tsunami resulting from an underwater earthquake.

Keywords: fluid simulation, SPH, CUDA, MPI, Navier-Stokes, tsunami

1. Introduction

Submarine earthquakes may generate tremendous disasters for human, like what occurred during the Tohoku earthquake in 2011. Even if their seismic waves may damage buildings and structures when they occur close to the coast, the tsunami they generally cause are a massive risk for humans. Indeed, the energy produced by a massive undersea quake is transmitted into the water at high speed and results in a high wave when it arrives on the coast.

To avoid human losses, tsunami's simulations can help to inform the governments and society about the risks before and after a submarine earthquake. This chapter presents solutions for implementing such simulations. The main objective is to be able to calculate the propagation of the tsunami wave into the ocean and then to simulate efficiently its effects when the wave reaches the coast. These kinds of simulation can be done in two dimensions considering only the profile of the coast or in three dimensions when all the topography is considered. In both cases, the simulation must handle how water is affected by the earthquake wave.

Viscosity is the measure depicting how a fluid resists deformations. Even water is considered having a non-nil viscosity: so, this parameter must be considered carefully for tsunami simulations. Water simulation relies on Navier-Stokes equations that describe the motion of a viscous fluid. Unfortunately, Navier-Stokes equations cannot be solved directly like it is the case for many differential equations. The only way to obtain a solution at a given time consists of approximating it through simulation. In practice, two family of methods may be used. The first one consists in discretizing the simulation space into small parts and to do the

simulation considering fixed cells in this discrete space (mesh approach). Well-known methods are the finite element, the finite difference, and the finite volume. A second alternative approach is the smoothed particle hydrodynamics (SPH), introduced in astrophysics in 1977 [1, 2], which is applied in computer graphics [3], oceanography, and many other fields. The latter is particularly interesting for tsunami simulation, since the most important part of the simulation is not in the ocean but rather on the ground. This implies that a part of the fluid will cover the coast. This heterogeneity makes the mesh-free SPH approach more adapted.

This chapter is organized as follows. Section 2 presents the basics of SPH, detailing the different involved mathematical expressions and steps and previous implementations proposed in the literature. Section 3 presents a parallel implementation of SPH: it recalls the main parallel patterns and how they are used to obtain a reliable and fast simulation. Before the conclusions, Section 4 presents some results for a simple case of tsunami.

2. SPH formulation

SPH is a Lagrangian approach, meaning that particles representing tiny parts of the fluids may move during the simulation. It is based on density estimation applied to moving particles, leading to an approximation of the Navier-Stokes equations. This section recalls these equations and presents the basics of SPH.

2.1 Navier-Stokes equations

Navier-Stokes equations model the dynamics of a fluid. They rely on the Newton second law, stating that the sum of the forces applied on a body equals the product of its mass by its acceleration ($\sum F = m \cdot a$). In practice, it is a system of two equations: the mass continuity equation and the momentum equation. The first one is given by

$$\frac{\partial \rho}{\partial t} + \nabla(\rho u) = 0 \tag{1}$$

where ρ designs the fluid density, ∇ is the gradient operator, and u is the flow velocity. The momentum equation is

$$\rho\left(\frac{\partial u}{\partial t} + u \cdot \nabla u\right) = -\nabla p + \mu \nabla^2 u + \rho g \tag{2}$$

where $\cdot \nabla$ is the divergence operator, ∇^2 the Laplacian operator, p the pressure, μ the dynamic viscosity coefficient, and g the gravity term. The right part of the momentum equation represents the sum of the forces that the fluid undergoes, where $-\nabla p$ is the pressure force, $\mu \nabla^2 u$ the viscosity force, and ρg the gravitational force. With the fluid velocity function being unknown, it is not possible to compute analytically its divergence. Then, the momentum equation is nonlinear.

Nevertheless, some methods allow to calculate an approximation of these two equations. Most of them regularly discretize the Euclidean space and calculate an approximation by using the finite difference theorem. The advection term (the left part of the momentum equation) is approximated placing particles into the grid and then computing their displacement. In other words, each grid cell contains a given amount of fluid, and the algorithm calculates the exchanges between adjacent cells.

Such a solution is quite difficult to use into environment where some large part (like ocean) and highly detailed parts must be considered together.

Another method to approximate the Navier-Stokes equations is SPH. The Euclidean space is no more discretized. Instead, it considers some moving particles representing the fluid and their interactions. Each particle comes with its specific velocity, pressure, density, and viscosity. Then, the total derivative allows to approach the advection term (those between parentheses on the left part of the momentum equation) by a single derivative term $\frac{du}{dt}$. For a given particle i, the momentum equation becomes

$$\rho_i\left(\frac{du_i}{dt}\right) = -\nabla p_i + \mu_i \nabla^2 u_i + \rho_i g \qquad (3)$$

Therefore, the acceleration a_i of the particle i is given by

$$a_i = \frac{du_i}{dt} = -\frac{\nabla p_i}{\rho_i} + \frac{\mu_i \nabla^2 u_i}{\rho_i} + g \qquad (4)$$

2.2 Introduction to SPH

SPH relies on the kernel density estimation [4]. When we only have some samples of a given function, we can estimate its value at a new location using a kernel function W and the following estimation:

$$f(x) = \frac{1}{n} \sum_{i=1}^{n} W\left(\|x - x_j\|\right) f(x_i) \qquad (5)$$

The kernel function W must be a unit positive function. In other words, it must satisfy the two following properties:

$$\forall x \in \mathbb{R}, \, W(x) \geq 0 \qquad (6)$$

$$\int_{\mathbb{R}} W(x) dx = 1 \qquad (7)$$

We denote W_h a kernel function with bounded support $[0, h]$. This simply means that $W_h(x) = 0$ for all $x < 0$ or $x \geq h$. This mathematical tool is used to approximate any scalar field A_i for any particle i:

$$A_i = \sum_{j=1}^{n} A_j \frac{m_j}{\rho_j} W_h\left(\|x - x_j\|\right) \qquad (8)$$

where m_j and ρ_j are, respectively, the mass and the density of the jth particle. Useful kernels for liquids are given in [3]. From this simple expression, we can deduce the estimation of the gradient and the Laplacian of a scalar A_i:

$$\nabla A_i = \sum_{j=1}^{n} A_j \frac{m_j}{\rho_j} \nabla W_h\left(\|x - x_j\|\right) \qquad (9)$$

$$\nabla^2 A_i = \sum_{j=1}^{n} A_j \frac{m_j}{\rho_j} \nabla^2 W_h\left(\|x - x_j\|\right) \qquad (10)$$

These formulas allow to calculate the density of any particle, the gradient of the pressure, and the Laplacian of the velocity to approximate a solution of the Navier-Stokes equations. For each particle i, the SPH algorithm follows:

- Compute the density ρ_i:

$$\rho_i = \sum_{j=1}^{n} m_j W_h \left(\left\| x - x_j \right\| \right) \tag{11}$$

- Compute the pressure p_i:

$$p_i = k(\rho_i - \rho_0) \tag{12}$$

where k is the gas constant and ρ_0 is the rest density.

- Compute f_i, the sum of the forces at particle i of pressure, viscosity, surface tension, and gravity:

$$f_i^{pressure} = - \sum_{j=1}^{n} m_j \frac{p_i + p_j}{2\rho_j} \nabla W_h \left(\left\| x_i - x_j \right\| \right) \tag{13}$$

$$f_i^{viscosity} = \mu \sum_{j=1}^{n} m_j \frac{u_j - u_i}{\rho_j} \nabla^2 W_h \left(\left\| x - x_j \right\| \right) \tag{14}$$

$$f_i^{surface} = -\sigma \nabla^2 cs_i \frac{n_i}{|n_i|} \tag{15}$$

$$f_i^{gravity} = \rho_i g \tag{16}$$

where σ is the tension coefficient relating to the interface between the fluid and the exterior (the air), n_i is the normal vector to a particle i, and cs_i is the color field of the particle i.

- Compute the velocity u_i and the new particle position x_i using a small integration time step Δt:

$$u_i = u_i + \Delta t \frac{f_i}{\rho_i} \tag{17}$$

$$x_i = x_i + \Delta t u_i \tag{18}$$

The SPH simulation uses these formulas to compute the positions of the particles for a given time length through an iterative procedure. The particles' interactions are very important: we use a rather small support (small h value) for the kernel function in order to limit the number n of neighboring particles. Then, in any good implementation, one of the key elements is the neighboring handling. Using a parallel processor, this can be achieved with a low complexity, allowing to reach short computation times.

2.3 SPH algorithms

SPH method presented in Section 2.2 is quite immediate to implement [3]. Using a small kernel support, the calculation of the forces that apply to a given particle is quite fast, since only a few numbers of neighbors have to be considered. Nevertheless, the neighborhood needs to be efficiently computed and stored to accelerate the calculations. This needs to be done for each time step. To do that, a regular grid is the faster solution. The size of a grid cell is set as the radius of the kernel support. Then, to find the neighbors of a given particle, it is enough to consider the cells

surrounding the one containing this particle. In dimension 2 this leads to 9 cells (including the cell containing the particle) and 27 in dimension 3.

The SPH method described in Section 2.2 has been extended to solve some accuracy problem with incompressible fluids, for instance, predictive-corrective incompressible SPH (PC-ISPH), incompressible SPH (ISPH), and implicit incompressible SPH (IISPH) [5–7]. In Ref. [7], comparisons between these three techniques show that IISPH is faster than PC-ISPH and ISPH, mainly since it allows to use bigger time steps. Hence, this chapter focusses on an implementation of IISPH. This evolved method is also more complex than classical SPH, and then each time step uses more calculations (but they are longer, so it is faster still). More precisely, for each particle it calculates the density ρ_i and the forces of viscosity, surface tension, and gravity like in SPH method. It adds the calculation of the advection velocity, which is the portion of the velocity independent to the pressure exerted by the other particles:

$$u_i^{adv} = u_i + \frac{\Delta t}{m_i} \left(f_i^{viscosity} + f_i^{surface} + f_i^{gravity} \right) \tag{19}$$

The IISPH algorithm calculates the advection factor d_{ii} and the advection coefficient a_{ii}:

$$d_{ii} = -\Delta t^2 \sum_j^n \frac{m_j}{\rho_i^2} W_h(x_i - x_j) \tag{20}$$

$$a_{ii} = \sum_j^n m_j (d_{ii} - d_{ji}) \Delta W_h(x_i - x_j) \tag{21}$$

The IISPH algorithm continues with the calculation of pressure's forces. It is done through at least two corrective loops to enforce the minimization of the difference between the rest density and the sum of the density of all particles. First, this loop calculates the advection density:

$$\rho_i^{adv} = \rho_i + \Delta t \sum_j^n m_j \left(u_i^{adv} - u_j^{adv} \right) \cdot \Delta W_h(x_i - x_j) \tag{22}$$

Second, it calculates the following term per particle that will be used many times in the next steps:

$$\sum_j^n d_{ij} p_j^l = \Delta t^2 \sum_j^n -\frac{m_j}{\rho_j^2} p_j^l \Delta W_h(x_i - x_j) \tag{23}$$

where l is the iteration number of the corrective loop. Notice that for $l = 0$, IISPH uses $p_i^0 = \omega p_i$, with $\omega = 0.5$.

Then, the IISPH corrective loop continues by computing for each particle the pressure force thanks to the following expression:

$$f_i^{pressure} = \sum_j^n -m_i m_j \left(\frac{p_i}{\rho_i^2} + \frac{p_j}{\rho_j^2} \right) \Delta W_h(x_i - x_j) \tag{24}$$

where p_i is the pressure at a particle i:

$$p_i = (1 - \omega) p_i^l + \frac{\omega}{a_{ii}} \left(\rho_0 - \rho_i^{adv} - \sum p_i^l \right) \tag{25}$$

This last term is computed using the displacement factors:

$$\sum p_i^l = \sum_j^n m_j \left(\sum_j^n d_{ij} p_j^l - d_{jj} p_j^l - \sum_{k \neq i}^n d_{jk} p_k^l \right) \cdot W_h \left(x_i - x_j \right) \qquad (26)$$

All these calculations should be made in parallel to reduce the computation times, using a tuned implementation, for instance, using message passing interface (MPI) for high-performance computing (HPC) or using the Nvidia common unified device architecture (CUDA) on graphics processing unit (GPU) for simpler computers.

3. Parallel SPH implementation

An efficient SPH implementation relies on parallelism at some level. A fully parallel solution may become a very efficient solution, as previous works have shown it. While most of the calculations may be done considering a single particle into a single core, finding the neighboring particles that play a role in the density, the pressure, and the external forces needs collaboration between different cores.

Using the texture mechanism available with GPU, working with the neighbors is quite simple and efficient. Nevertheless, this implies to store all the particles into a regular grid at each time step during the simulation. This part is somewhere the most complicated, and the key step for an efficient implementation.

This section first presents the main parallel patterns (MAP, SORT, SCAN, etc.) and then shows how they can be combined to write a new fast parallel SPH solver.

3.1 Parallel patterns

Writing a parallel algorithm is not as simple as writing a sequential algorithm. This truism is based on the necessary consideration of the collaborations between the different processors of a parallel machine: all the processors must work in concert, and not isolated as in a sequential approach. These collaborative aspects are the main difficulty. How to make sure all these processors expect when it's needed and work to the fullest when no synchronization is required?

Rather than writing a parallel algorithm based on classical sequential patterns, parallel patterns make it possible to write a parallel algorithm directly, abstracting the underlying machine. These patterns rely on very simple parallel architecture, called the parallel random-access memory (PRAM). It assumes a synchronization between an infinite set of processors and an infinite amount of memory [8].

3.1.1 Simple parallel patterns

Simple parallel patterns do not need synchronization. This means that, using a GPU or an HPC, they may be run without any difficulties, even with less processors than needed. The simpler one is the MAP, or transform, that consists in applying a given function f to an input data to obtain the output. The key of this pattern is about the localisation of the data: input and output are generally considered as vectors (or arrays). Then, MAP applied to data at the same index:

$$Y_i = f(X_i) \quad \text{(MAP)} \qquad (27)$$

Figure 1 describes this pattern on small arrays.
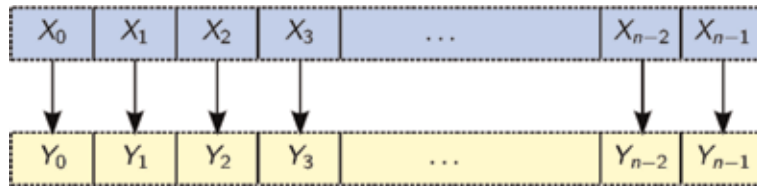
Figure 1.
Illustration of the MAP parallel pattern.
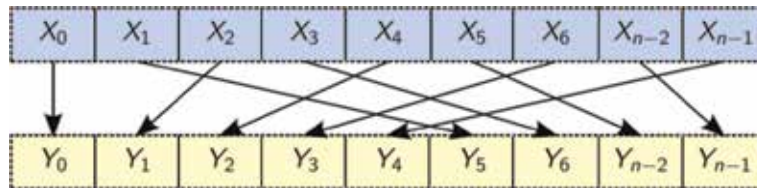
Figure 2.
The SCATTER and GATHER patterns move data using a permutation.

In many occasions, it is necessary to write the result at a new location, another index. When each possible destination index is used once and only once, we obtain a quite simple parallel pattern called SCATTER. It consists of writing the input data from location i to the destination location $map(i)$, map being a permutation function. **Figure 2** illustrates this parallel pattern.

In the same spirit, the GATHER parallel pattern writes at index i data coming from index $map(i)$, using again a permutation function. To differentiate between a SCATTER and a GATHER, you should remember that at first we read contiguous data, while in the second, we write at contiguous location. This is resumed with the following two expressions:

$$Y_{map(i)} = X_i \quad \text{(SCATTER)} \tag{28}$$

$$Y_i = X_{map(i)} \quad \text{(GATHER)} \tag{29}$$

PRAM model is very useful to write efficient algorithms on theory. Nevertheless, at the end these algorithms run on real computers, with a limited amount of memory and a fixed number of processors. Brent's theorem links the theoretical computation time on PRAM model with the one obtained using only p processors: an algorithm made in $O(1)$ using m processors will run in $O\left(\frac{m}{p}\right)$ using only p processors. This allows to predict the behavior of (very) simple algorithm on a GPU.

3.1.2 Advanced parallel patterns

In many cases, some degree of collaboration is needed between processors. This leads to some more complicated parallel patterns. A very common parallel pattern using such a collaboration is the SORT that sorts data according to a given order. It is used in previous SPH implementation for building the neighbors' grid. The SORT pattern is based on the PARTITION pattern that moves values with respect to a given predicate. More precisely, for n values X_i and using the predicate $P_i \in [0, 1]$, the PARTITION pattern moves the values X_i for which $P_i = 1$ at the beginning of the resulting array, the others at the end (see **Figure 3** for a simple example).
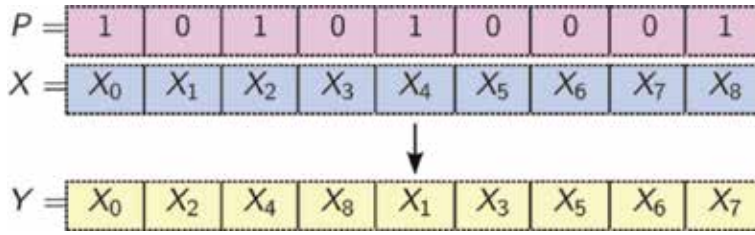
Figure 3.
Illustration of the PARTITION pattern for nine input values; the values with predicate 1 are put at the beginning of the output, the others at the end.

These complex patterns are built using a fundamental pattern called SCAN. It corresponds to a prefix sum of values, according to the following expression:

$$Y_i = \bigoplus_{j=0}^{i} X_j \quad (\text{INCLUSIVE} - \text{SCAN}) \tag{30}$$

The fundamental pattern exists in two versions: inclusive and exclusive ones. The first corresponds to the expression given above, doing a sum-up to the current output position. The exclusive version omits the current position, doing a sum-up to $i - 1$ and using a nil value for Y_0 (generally, using 0):

$$Y_i = \bigoplus_{j=0}^{i-1} X_i \quad (\text{EXCLUSIVE} - \text{SCAN}) \tag{31}$$

Figure 4 shows that these two versions of SCAN are almost the same, except the shift between the resulting arrays: the values obtained with inclusive version correspond to the ones obtained with the exclusive version at the same position plus one.

Another pattern of interest into this chapter is the REDUCE that allows to calculate a single value from an array of values and using any given associative binary function:

$$Y = \bigoplus_{j=0}^{n-1} X_i \quad (\text{REDUCE}) \tag{32}$$

For instance, using $X = [1, 2, 3, 4, 5, 6, 7, 8, 9, 10]$ and the classical integer sum as binary operator, this pattern returns $Y = 55$, the sum of the 10 first non-nil integers.

These complex patterns have roughly speaking all the same complexity, in $O(\log n)$ on a PRAM machine and $O\left(\frac{n}{p} \log \frac{n}{p}\right)$ using p processors only. Nevertheless, since they are built using the SCAN, PARTITION and SORT are in practice more complex and take more time. A fast implementation of the SORT pattern relies on the radix sort algorithm that loops over the number of digits of the maximum key to sort, thus having a practical complexity in $O(32 \log n)$ with 32-bit integers.

X_i	1	1	1	1	1	1	1	1
SCAN	1	2	3	4	5	6	7	8
PRESCAN	0	1	2	3	4	5	6	7

Figure 4.
Differences between the inclusive and exclusive SCAN patterns.

The last programming tool this section covers is the atomic operation notion. A load-modify-write operation cannot be handled in parallel program without caution. Let us consider two processors doing a "plus one" in parallel at the same time. The addition is done by the CPU using registers (local memory to the CPU). Hence the variables to add need to be loaded from the main memory, then added, and then stored into the main memory. If the two processors do the load-modify-write operation at the same time exactly on the same variable, then the result is false. If the processors are not exactly synchronized, the result is certainly false also: to be correct, the two operations must be done sequentially. Atomic operations provide this behavior, performing the read-modify-write operation for one and only one processor at a time.

Obviously, other parallel patterns exist. They are not discussed in this chapter since they are not used in our SPH implementation.

3.2 Grid building

Previous SPH implementations use the SORT pattern to build the neighbors' grid [7, 9, 10]. The first step consists in calculating the grid index of each particle, using a MAP. Next, the particles are sorted with respect to this index. Then, it is necessary to compute the number of particles per cell and the starting position of each cell. In [9], atomic operations are used for these two operations: the minimum for the first particle into each cell and the addition for the number of particles per cell.

In Ref. [7], authors follow a similar approach with the particle sort with respect to their cell index but using a MAP to mark the start and the end of each cell with respect to the sorted cell indices, considering their unicity.

The main problem is that the sorting algorithm takes a large part of the computation time, near 30% according to [10]. In this chapter, we avoid the full sorting by combining simple parallel patterns and atomic operations. Our grid building algorithm is summarized in **Figure 5**.

This algorithm uses the Nvidia Thrust API with some freedom to shorten it. First, at line 8 the number of particles per grid cell is set to zero. Next, like with previous methods at line 9, the index of each particle is calculated with a MAP. Using a second MAP at line 10, the particle cell offset is calculated using an atomic addition. More precisely, we use the CUDA int. atomicAdd(int*cc, int. a) function that adds a to the variable *cc and returns the old content of *cc. Since atomic operations are done in sequence, the number of particles per cell is correctly computed. Moreover, each particle receives the old counter value, which is 0 for the first atomic operation execution, 1 for the second, and so on up to $m - 1$ for the last particle added to the

```
1    void GridBuilding(
2        device_vector<Particle>& Particles,
3        device_vector<unsigned>& cell_start
4    ) {
5        device_vector<Particle> p(Particles);
6        device_vector<unsigned> index(Particles.size());
7        device_vector<unsigned> local_offset(Particles.size());
8        memset(local_offset, 0, local_offset.size());
9        transform(p, index, Particle2Index());
10       transform(index, local_offset, Index2LocalOffset());
11       exclusive_scan(local_offset, cell_start);
12       transform(index, local_offset, local_offset, Local2Global(cell_start));
13       scatter(p, local_offset, Particles);
14   }
```

Figure 5.
Our algorithm to build the neighbors' grid.

cell, *m* being the number of particles added into the cell. These values are used to scatter all the particles to their local position into the grid, at line 13. But, before to do that we need to calculate the global grid offset, corresponding to the position of the first particle of each cell. This is done using an exclusive SCAN at line 11 to compute the global offset, followed by a MAP at line 12 to calculate each particle global offset.

In practice, this algorithm can be optimized in many ways. First, the device vectors can be allocated only once, and not each time the grid is built. Second, the first two transforms (lines 9 and 10) can be mixed into one. This will limit the memory loading into device registers, known as a major performance limitation with GPU. At last, the last transform (line 12) and the scatter (line 13) can be mixed into a single call again to minimize the memory bandwidth usage. Moreover, the particles' data must be split into multiple arrays for efficiency (one array for position, one for density, one for pressure, etc.) as in [10].

3.3 Main algorithm

The most difficult part of the implementation of the IISPH method is the construction of the neighbors' grid, as for any non-mesh density kernel method. The rest of the calculation is rather simple and relies on two parallel models: the MAP for all the loops on particles and the REDUCE to control the termination of the corrective loop in the calculation of the pressure force.

It is noticeable that the IISPH loop to correct the pressure force runs on the CPU, because there is no available global synchronization on the GPU. Then, the REDUCE is used to return a value from the GPU to the CPU, to decide if more corrections are needed or not. Nevertheless, since this just consists of sending one real value, it is not a big bottleneck.

Moreover, many calculations use data from the neighbors (pressure, density, position, etc.). L1 GPU's memory is used to accelerate these calculations, reducing the computation time around a third in our experiment. Notice also that the IISPH corrective loop amortizes the neighbors' grid building. In our experiments the grid building now represents less than 10 percent of the full computation time.

4. Experiments

The IISPH is a valid solution to simulate a tsunami [11]. Its main advantage regarding a discrete method is that it does not need to refine the mesh near the obstacles, like the coast and the buildings. Moreover, the wave can go everywhere, including interfering with the beach, buildings, infrastructure, etc.

In this chapter, we illustrate the tsunami simulation using IISPH algorithm through a rather simple scenario. It contains a short coast ending with a mountain. We put a building just after the beach. The main difficulty, if either, consists of generating the solitary wave. A tsunami, for instance, is generated by an earthquake at long distance. The produced wave runs at 200 meter per second (720 km/h). We do not need to simulate the propagation of the wave since its epicenter, which is quite difficult with long distance: it needs very long simulation time to see the wave reaching the beach, and obviously it needs a huge amount of memory to handle the sea between the two distant locations. Instead, we simulate the wave into a rather small space. We can predict the time of arrival to the beach, assuming we know the exact distance between the beach and the earthquake location.

In [11], authors solve the solitary wave solution of Boussinesq. They calculate the wave paddle displacement using the equation:

$$X(t) = Ct - \frac{\theta}{\kappa} \tag{33}$$

where C is the wave velocity, t is the time in the simulation frame, κ is the decay coefficient, and θ is given using Newton's method by

$$\theta^{l+1} = \theta^l - \frac{\theta^l - \kappa Ct + \frac{H}{h}\tan\left(\theta^l\right)}{l + \frac{H}{h}\operatorname{sech}^2\left(\theta^l\right)} \tag{34}$$

More precisely, θ is the solution of the following problem:

$$X(t) = \frac{H}{\kappa h}\tanh(\kappa(Ct{-}X(t))) \tag{35}$$

where H and h are the wave height and the water depth, respectively.

While this method works on CPU, it is not well-suited for a CUDA implementation of the IISSPH, mainly because the number of iterations of the Newton-Raphson method depends on the input values, and so is not constant per particle.

Hence, in this chapter we use a different but simple technique. The wave is produced using a piston wave generator. Here, the piston is a huge virtual object that moves the water to reach the speed of the wave. The length and the speed of the piston movement are calibrated to obtain the good height and speed of the tsunami solitary wave.

Figure 6 illustrates such a simple wave simulation, before the tsunami wave arrives. **Figure 7** shows the wave arriving at the building at $t = 4$ s in the simulation frame. In **Figure 8**, at $t = 8$ s, the building is completely below the ocean that returns
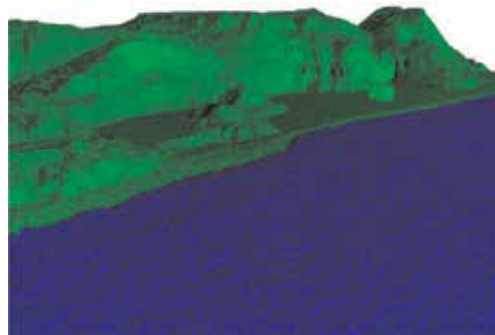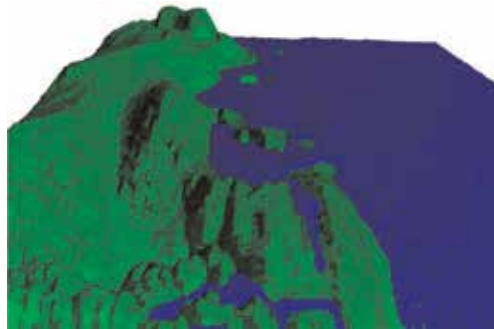

Figure 6.
Tsunami simulation before the solitary wave arrives.
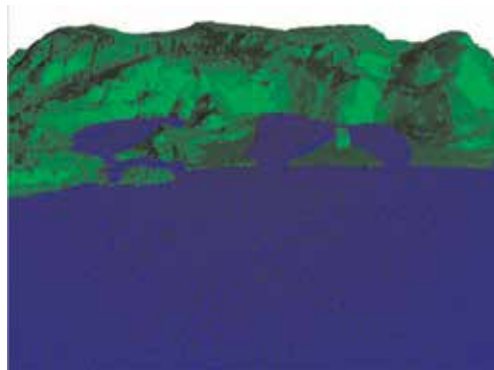

Figure 7.
Tsunami wave reaching the building near the beach.
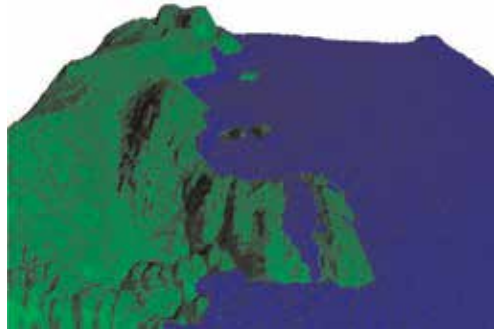
Figure 8.
The tsunami wave engulfed the building and the coast.

Figure 9.
The tsunami wave begins to pull off the coast. With flat coasts, this may take some time.

Figure 10.
After a longer time, the tsunami wave has almost completely disappeared.

into its bed after some more time (see **Figures 9** and **10**). The building is made with fixed particles that nevertheless are considered with the moving particles of the fluid. This allows an interaction between two kinds of particles, and it permits to obtain the pressure and force applied to the building, for instance, to check if it will resist or not.

5. Conclusions

This chapter focusses on the simulation of a tsunami solitary wave. Such a wave is mainly produced by submarine earthquake and may provoke vast disasters for

human living near the coasts. Such phenomena also may produce strong degradation on buildings and structures, in turn inducing human loss as what happened after the Tohoku earthquake in 2011. To avoid these disasters, it is important to be able to validate the robustness of structures and buildings near the dangerous coasts and to inform population after an always unpredictable submarine earthquake.

To achieve these goals, it is necessary to produce robust and fast fluid simulator software. To simulate a tsunami wave, a good candidate is the SPH method. Since it does not need the usage of a fix mesh like in discrete techniques, it allows to handle correctly the wave running on the beach and after. Moreover, it correctly handles the contact with buildings and structures, allowing to simulate the forces that they undergo.

This chapter recalls the implicit incompressible SPH method, which is one of the fastest among the SPH ones. The parallel implementation for GPU is detailed in depth, with a fast algorithm to build the neighbors' grid, avoiding the classical sorting method which is more time-consuming.

At last, this chapter proposes a simple tsunami wave simulation using a piston wave generator, a simple solution for implementing and providing valuable results. It can be used to simulate tsunami generated by submarine earthquake occurring in a pattern of seismic source mechanism when both the location and intensity are estimated.

Author details

Pierre Thuillier Le Gac[1], Emmanuelle Darles[1], Pierre-Yves Louis[2] and Lilian Aveneau[1]*

1 XLIM, UMR 7252, CNRS, University of Poitiers, France

2 LMA, UMR 7348, CNRS, University of Poitiers, France

*Address all correspondence to: lilian.aveneau@univ-poitiers.fr

IntechOpen

References

[1] Gingold RA, Monaghan JJ. Smoothed particle hydrodynamics: Theory and application to non-spherical stars. Monthly Notices of the Royal Astronomical Society. 1997;**181**(3): 375-389. DOI: 10.1093/mnras/181.3.375

[2] Lucy LB. A numerical approach to the testing of the fission hypothesis. The Astronomical Journal. 1977;**82**: 1013-1024

[3] Müller M, Charypar D, Gross M. Particle-based fluid simulation for interactive applications. In: Proceedings of the 2003 ACM SIGGRAPH/Eurographics Symposium on Computer Animation. 2003. pp. 154-159

[4] Silverman B. Density Estimation for Statistics and Data Analysis. New York: Routledge; 1998. DOI: 10.1201/9781315140919

[5] Solenthaler B, Pajarola R. Predictive-corrective incompressible SPH. In: Hoppe H, editor. ACM SIGGRAPH 2009 papers (SIGGRAPH '09). New York, NY, USA: ACM; 2009. 6 p. DOI: 10.1145/1576246.1531346

[6] Shao S, Lo EYM. Incompressible SPH method for simulating Newtonian and non-Newtonian flows with a free surface. Advances in Water Resources. 2003;**26**(6):787-800. DOI: 10.1016/S0309-1708(03)00030-7

[7] Ihmsen M, Cornelis J, Solenthaler B, Horvath C, Teschner M. Implicit incompressible SPH. IEEE Transactions on Visualization and Computer Graphics. 2014;**20**(3):426-435. DOI: 10.1109/TVCG.2013.105

[8] Blelloch GE. Vector Models for Data-Parallel Computing. Cambridge, Massachusetts, London, England: MIT Press; 1990

[9] Goswami P, Schlegel P, Solenthaler B, Pajarola R. Interactive SPH simulation and rendering on the GPU. In: Eurographics/ACM SIGGRAPH Symposium on Computer Animation; 2010. pp. 1-10

[10] Bilotta G, Zago V, Hérault A. Design and implementation of particle systems for meshfree methods with high performance. In: High Performance Parallel Computing. IntechOpen; 2018. DOI: 10.5772/intechopen.81755

[11] Sampath R, Montanari N, Akinci N, Prescott S, Smith C. Large-scale solitary wave simulation with implicit incompressible SPH. Journal of Ocean Engineering and Marine Energy. 2016; **2**(3):313-329. DOI: 10.1007/s40722-016-0060-8

Chapter 5

Seismic Velocity Structure in and around the Japanese Island Arc Derived from Seismic Tomography Including NIED MOWLAS Hi-net and S-net Data

Makoto Matsubara, Hiroshi Sato, Kenji Uehira,

Masashi Mochizuki, Toshihiko Kanazawa, Narumi Takahashi,

*Kensuke Suzuki and Shin'ichiro Kamiya*

Abstract

Japanese Islands are composed of four plates, with two oceanic plates subducting beneath the two continental plates. In 2016 the National Research Institute for Earth Science and Disaster Resilience (NIED) Seafloor Observation Network for Earthquakes and Tsunamis along the Japan Trench (S-net) started seismic observation of the offshore Hokkaido to Boso region in the Pacific Ocean, and Dense Oceanfloor Network System for Earthquakes and Tsunamis (DONET) was transferred to NIED. We add the NIED S-net and DONET datasets to NIED high-sensitivity seismograph network (Hi-net) and full range seismograph network (F-net) datasets used in the previous study and obtain the three-dimensional seismic velocity structure beneath the Pacific Ocean as well as Japanese Islands. NIED S-net data dramatically improve the resolution beneath the Pacific Ocean at depths of 10–20 km because the seismic stations are located above the earthquakes and on the east side of the Japan Trench. We find a NS high-Vp zone at depths of 20–30 km. The 2018 Eastern Iburi earthquake occurred below the northern part of this high-V zone. The coseismic slip plane of the 2011 Tohoku-oki earthquake has low Vp/Vs, but its large slip region has high Vp. The broad low-Vp/Vs region may play a role in large earthquake occurrence.

Keywords: seismic tomography, failed rift, offshore event, NIED S-net, DONET, NIED Hi-net

1. Introduction

The Japanese Islands are mainly composed of the Eurasian (EUR) and the North American (NA) plates, and a number of small islands are on the Philippine Sea (PHS) and the Pacific (PAC) plates (**Figure 1**). The PHS and PAC oceanic plates are subducting beneath the EUR and the NA plates. A number of earthquakes occurred both at the plate interfaces and within the plates.
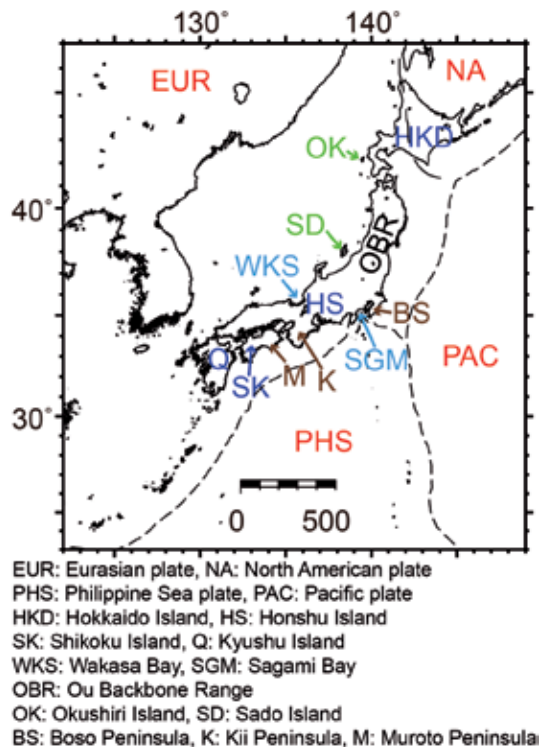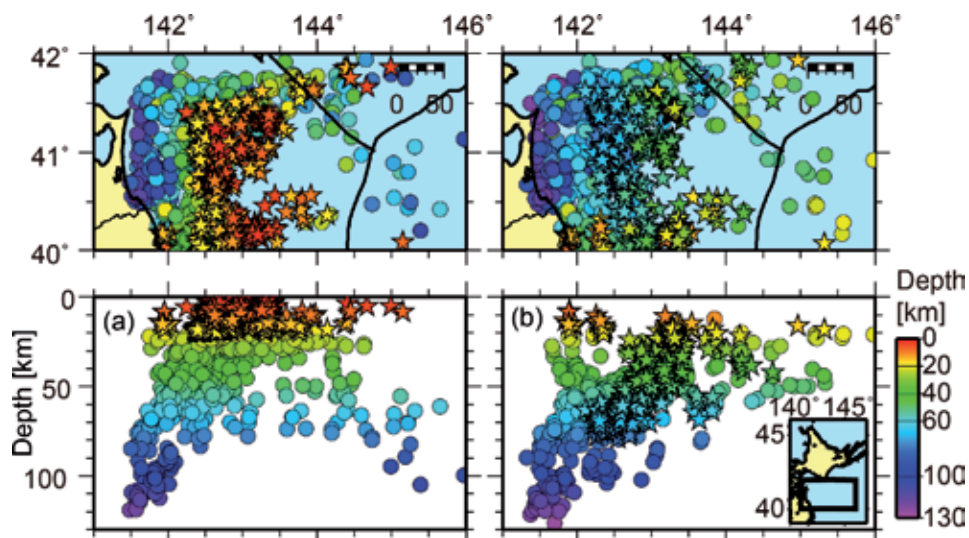
Figure 1.
Name of plates and location.

After the Kobe earthquake in January 1995, the Japanese government enacted the Special Measure Law on Earthquake Disaster Prevention in July 1995. This was to promote a comprehensive national policy on earthquake disaster prevention. Based on this goal, the National Research Institute for Earth Science and Disaster Resilience (NIED) contracted the deployment of the nationwide high-sensitivity seismograph network (Hi-net) [1] since NIED had already accumulated the experience for the Tokyo metropolitan deep borehole array and operated the Kanto-Tokai seismic network since 1979. NIED operates the Hi-net with approximately 800 stations since 2000 [2] and the full range seismograph network (F-net) [3] with approximately 70 stations composed of broadband seismographs since 1994 [4]. The Japan Meteorological Agency (JMA), the national universities, and other institutes operate other seismic networks with a total of approximately 600 stations for the detection of microseismicity. NIED operates ocean-bottom seismic stations beneath the Sagami Bay, while the JMA operates offshore the Tokai and Boso regions. The Earthquake Research Institute, University of Tokyo, operates the network offshore Sanriku, and the Japan Agency for Marine-Earth Science and Technology (JAMSTEC) operates offshore Kushiro and Muroto networks. JAMSTEC started the construction of the Dense Oceanfloor Network System for Earthquakes and Tsunamis (DONET) [5] off Kii and Muroto Peninsulas near the Nankai Trough in 2010, and they started operation networks offshore Kii (in 2014) and Muroto (in 2016) Peninsulas. NIED deployed the Seafloor Observation Network for Earthquakes and Tsunamis along the Japan Trench (S-net) [6] after the 2011 offshore Tohoku Earthquake (the Tohoku-oki event), which began operating in 2016 [7, 8]. DONET was transferred to NIED from April 2016. NIED started the operation of Monitoring of Waves on Land and Seafloor (MOWLAS) composed of Hi-net, F-net, S-net, DONET, strong-motion seismograph networks (K-NET and KiK-net) [9], and Volcano Observation Network (V-net) [10].

NIED S-net and DONET teams manually pick the arrival time data at the oceanic seismic stations after NIED Hi-net team has determined the hypocenters using the land stations. We confirm the difference of shallow hypocenters between the determination by only NIED Hi-net and that by NIED Hi-net and NIED S-net. Stars in **Figure 2** show the hypocenters at depths shallower than 20 km beneath the PAC plate determined by NIED Hi-net from September 11, 2017, to the end of 2018. The shallow hypocenters near the main island tend to remain shallow; however, hypocenters more than 200 km off the coast shifted significantly deeper to 40–80 km depth when including the S-net arrival time data (**Figure 2**). Deep events determined by NIED Hi-net on the east side of a longitude of 144°E are also shifted shallower. This suggests that it is important to include the S-net data for reliable hypocenter locations of offshore events.

Three-dimensional (3D) seismic velocity structure beneath the whole Japanese Islands has been studied using the vast data of seismic stations within the Japanese Islands maintained by NIED, JMA, national universities, and the other national and local governmental institutes (e.g., [11–14]). These studies used data obtained mainly at land-based seismic stations with a very few seismic stations on the sea floor such as Sagami Bay, off Kushiro, Sanriku, Boso, and Tokai regions. Reference [14] investigated the structure beneath the PAC plate at depths of 30–50 km using events that occurred under the Pacific Ocean (PO) with focal depths determined by NIED F-net. However, that study was not able to clarify the shallow structure beneath the PO at depths of 0–20 km because of the lack of seismic stations on the seafloor of the PO. The seismic ray takeoff angles proceed downward from the events to the seismic stations on land, and they do not pass through the shallow zone beneath the ocean since the distance from the hypocenter to the seismic stations is usually over 150 km. We investigated the 3D seismic velocity structure of and around Japanese Islands including the Sea of Japan and PO by the seismic tomographic method. We added the arrival time data detected in the S-net, the DONET, and the Hi-net datasets, operated by NIED, as well as other datasets, operated by multiple organizations, after 2016 in addition to the data used in [14]. Then we applied the seismic tomography to these datasets.

Figure 2.
Comparison of hypocenters determined by the NIED (a) Hi-net and (b) Hi-net and S-net. Stars denote hypocenters determined at depths shallower than 20 km by only Hi-net in (a) and redetermined by Hi-net and S-net in (b).

2. Data and method

The target region, 20–48°N and 120–148°E, covers the whole Japanese Islands from Hokkaido to Okinawa and the seismic stations both Hi-net on land and S-net and DONET beneath the ocean. In addition to the arrival time data used by [14], 1,782,425 P- and 1,528,733 S-wave arrival times from 32,952 earthquakes recorded at approximately 2000 stations including NIED S-net and DONET from April 2016 to June 2018 were selected. A total of 7,853,757 P-wave arrival data and 4,604,780 S-wave arrival data from 112,631 events are available after merging the new datasets (**Figure 3**).

We used the seismic tomographic method [15, 16] with spatial velocity correlation and station corrections to the original code by [11]. Grid nodes were placed with half of the spatial resolution. We performed smoothing in order to stabilize the solution for the inverse problem with the LSQR algorithm [17] since arbitrary damping matrix with combination of diagonal and smoothing matrices could be assumed.

We placed 3D grid nodes to construct the velocity (slowness) structure with the grid spacing shown in **Table 1** and adopted the 1D structure used in the routine determination of hypocenters at the Hi-net and S-net [18] as the initial velocity model (**Figure 4**). No velocity discontinuities such as Moho discontinuities or the plate boundary between the EUR and PAC or PHS plates were assumed in this study. This is because there were enough data to estimate the steep velocity gradient to represent plate boundaries so that velocity discontinues in the model were not necessary [13, 16, 19]. The total number of unknowns, 4,417,505, for P-wave slowness is the same as those for S-wave slowness. We solved the P- and S-wave slowness at each grid node from more than 10 associated rays.

First, we inverted the P- and S-wave seismic velocities using the initial hypocenter location. Second, both hypocenters and 3D seismic velocity structure were inverted simultaneously. We included the arrival times from the events beneath the ocean before 2015 in addition to the data used by [14]. Focal depths of offshore events were determined by NIED F-net or [20] since offshore events determined by only NIED Hi-net are not reliable. For these offshore events, only epicenters are inverted by the 3D seismic velocity structure, while hypocenter depths are fixed.
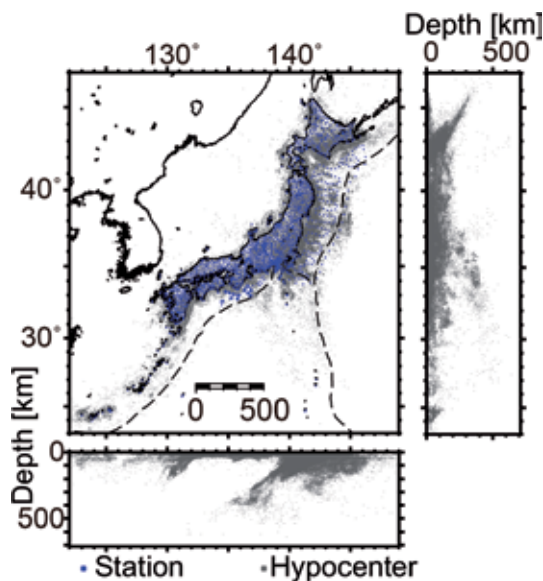
Figure 3.
Distribution of hypocenters and seismic stations used for seismic tomography.

Depth	Grid interval		Resolution/checkerboard pattern	
	Horizontal	Vertical (km)	Horizontal	Vertical (km)
0–10	0.1°	2.5	0.2°	5
10–40		5		10
40–60		10		20
60–180		15		30
180–300		20		40
300–		25		50

Table 1.
Grid interval and resolution size.
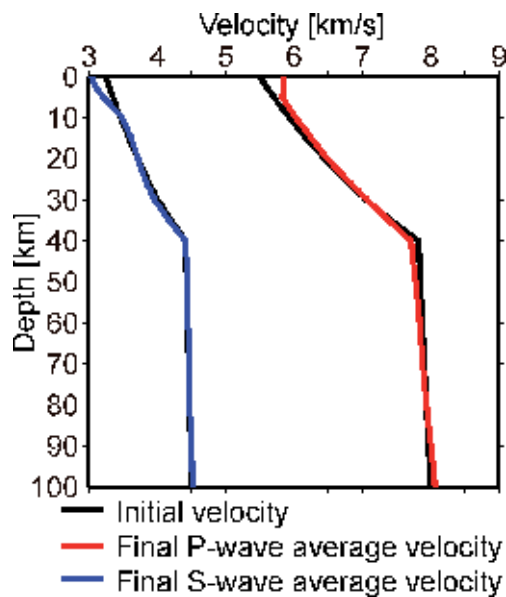
Figure 4.
Seismic velocity structures of the initial model and the average of the final 3D model.

We do not fix any condition for the events after 2016 detected by NIED S-net and DONET and the events within 50 km of the onshore seismic networks before 2015 during the inversion.

Residuals are improved to within 0.5 s for P-wave and 0.6 s for S-wave in the travel time inversion. In the final iteration, we used 6,356,481 P-wave arrival data and 3,534,482 S-wave arrival data to solve for the P-wave slowness at 1,135,165 grid nodes and the S-wave slowness at 1,103,525 grid nodes. The inversion reduces RMS of the P-wave travel time residual from 0.561 to 0.192 s and that of the S-wave data from 0.812 to 0.239 s after 11 iterations.
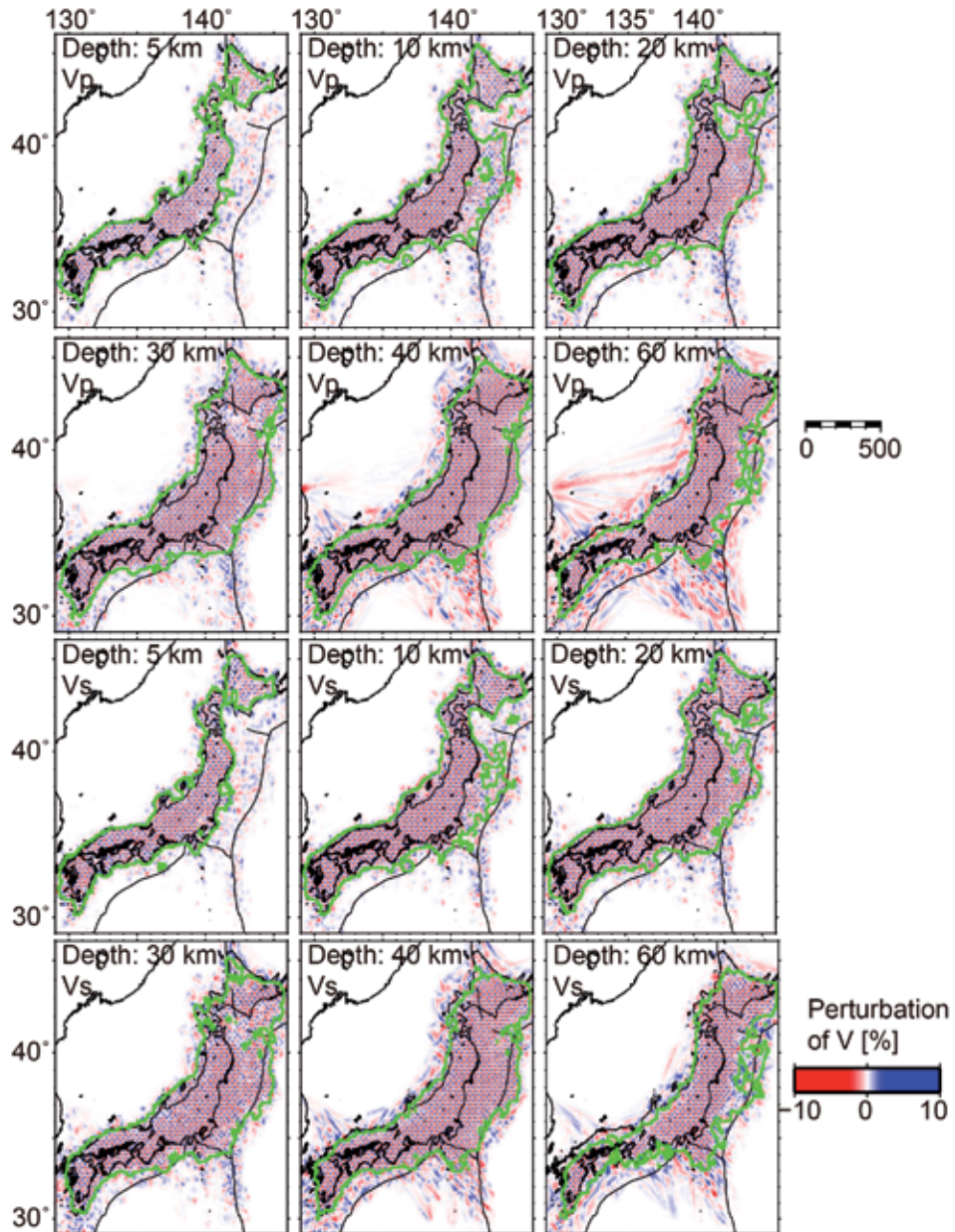
We conducted a checkerboard resolution test to evaluate the reliability of our solution [21]. We assumed a ± 5% checkerboard pattern and calculated synthetic travel times with random noise of 0 mean and standard deviations of 0.13 and 0.24 s for P- and S-waves, respectively. The standard deviations for random noise were derived from the average of the estimated uncertainty of the manually picked arrival times. The weight of data is inversely proportional to each width of picking error. The damping factors for the P-wave inversion are twice those for the S-wave inversion, since the average standard deviation of P-wave picking errors is almost half of that of S-wave.

3. Results

3.1 Results of checkerboard resolution test

Figure 5 shows the results of checkerboard resolution test. We calculate the recovery rate and stability with surrounding grid nodes in order to confirm well-resolved area [15]. The resolutions of Vp and Vs at depths of 5–30 km beneath main four islands are good. At depths of 40–60 km, resolutions are not good along the Sea of Japan coast because there are few deep earthquakes that can be used for inversion.

Figure 5.
Map views of checkerboard resolution test for Vp and Vs. green line surrounds the well-resolved area.

NIED S-net data increase the resolution at depths of 10–60 km from Honshu to the Japan Trench (**Figure 5**). Reference [14] used the offshore events such as aftershocks of the Tohoku-oki earthquake. The presence of a seismic station above the events is extremely important for the estimation of velocity structure as well as the determination of hypocenters. The resolutions at depths of 0 and 5 km are still not good in spite of the use of S-net data because the incident angle to the S-net stations are mainly steep and ray paths do not run horizontally because of the lack of shallow earthquakes. Resolutions near the triple junction of Japan Trench and Sagami Trough where three plates, PAC, PHS, and EUR, meet are good at depths of 20–30 km. This is an advantage of using NIED S-net.

Beneath the DONET area, the resolution at depths of 10–60 km is good for Vp, and those at depths of 5–40 km are good for Vs. The resolved zone extends to the Nankai Trough since there is sufficient seismicity in this area.
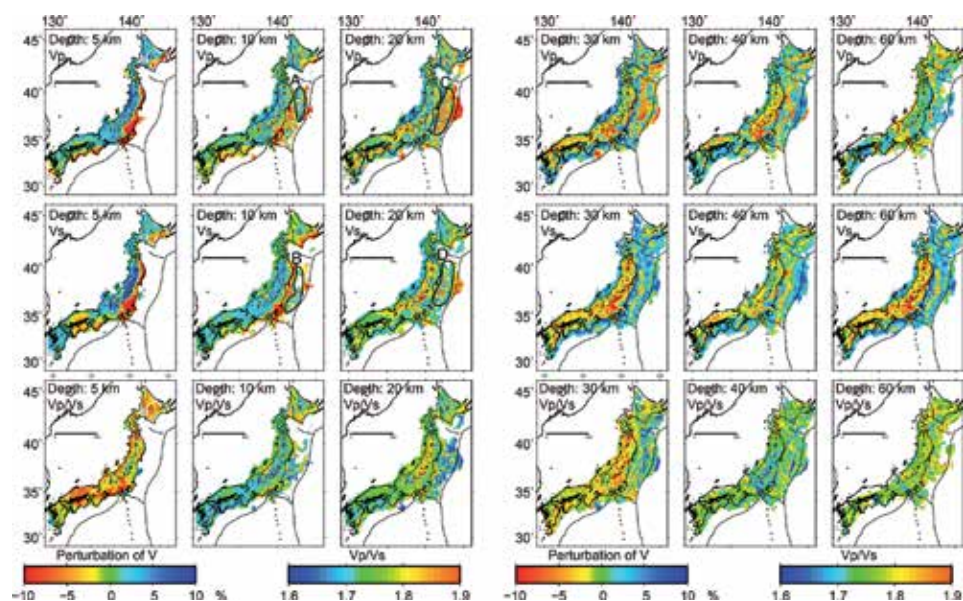
3.2 Map views at depths

We calculated the average 1D model from the final 3D velocity structure (**Figure 4**). We also showed the perturbation from these average velocities (**Figure 6**).

At a depth of 5 km, low-Vp and low-Vs regions are located along the PAC coast beneath southeastern Hokkaido, northeastern Honshu, most of Kanto, Sagami Bay, southern Kinki, and southern Shikoku regions. A low-Vs region extends beneath the entire Shikoku and southern Chugoku regions. A low-Vp/Vs region runs along the Ou backbone range in northeastern Japan and central Japan. Other regions have high Vp/Vs.

At a depth of 10 km, low-Vp regions extend beneath the active volcanoes in the northeastern and central Honshu and Kyushu regions. Low-Vs regions are almost the same as those at a depth of 5 km. High-Vp/Vs regions are distributed at central Hokkaido and coastal area in northeastern Japan. Low-Vp/Vs covers the other regions.

At a depth of 20 km, low-Vp regions lie beneath volcanoes in Hokkaido, central Honshu, and Kyushu. Low-Vs regions extend beneath the volcanoes and back-arc side of Honshu. Both low-Vp and low-Vs regions extend from central Kinki to

Figure 6.
Map views of Vp and Vs perturbation and Vp/Vs. Colored area is the resolved area. Broken white lines at depths of 10 and 20 km denote the median tectonic line.

Kyushu region across central Shikoku. This low-V zone remains the same as at a depth of 5 km. High-Vp/Vs regions cover the Ou backbone range and back-arc side of northeastern Honshu.

At a depth of 30 km, low-Vp extends beneath the northeastern Honshu, central and southwestern Honshu, and northern Kyushu regions. Low-Vs regions extend beneath most of Honshu, Kyushu, and northern Shikoku regions. High-Vp/Vs regions cover almost all Japanese Islands except the central Hokkaido.

At a depth of 40 km, low-Vp regions exist beneath the volcanoes in southeastern Hokkaido and northeastern and central Honshu regions. The low-Vp regions beneath the volcanoes in the northeastern Japan extend to back-arc side. Low-Vs regions are clarified beneath the volcanoes in southeastern Hokkaido and central Honshu regions. Low-Vs regions beneath the northeastern Honshu can be found east of the volcanic front as are low-Vp regions. Low-Vp/Vs regions cover the central mountains across Hokkaido and northeastern and central Honshu.

At a depth of 60 km, low-Vp and low-Vs regions extend beneath the volcanoes in Honshu and central Honshu. High-Vp and Vs regions extend beneath the Kinki, Shikoku, and eastern Kyushu regions where the PHS plates subduct. High-Vp/Vs regions are distributed across western Hokkaido, central Honshu, and central Shikoku regions.

At a depth of 90 km, low-Vp and low-Vs regions exist beneath the volcanoes beneath Hokkaido and Honshu. High-Vp and Vs regions extend to the east of northeastern Japan where the PAC plate subducts. High-Vp/Vs regions cover northern and southwestern Hokkaido, central Honshu, and central Kyushu regions.

3.3 Velocity structure beneath the Pacific Ocean off northeastern Japan beneath the S-net

At a depth of 10 km, a low-Vp and low-Vs zone extends along the coast of the PO in the northeastern Honshu. A high-Vp and high-Vs zone exists between the longitudes of 142 and 143°. East of longitude of 143° (**Figure 6A** and **B**), low-Vp, and low-Vs zone shows again. Vp/Vs is generally low except in some small regions.

At a depth of 20 km, a high-Vp and high-Vs zone extends along the coast of the PO in the northeastern Honshu, in contrast to the structure at a depth of 10 km. Low-V zones extend to the east of the high-Vp zone; however, some high-Vp zones exist among the low-Vp zones (**Figure 6C**). High-Vs zones are mixed with minor low-Vs zone off the east of northeastern Honshu, extending to a longitude of 143.5° (**Figure 6D**). This pattern can be seen with Vp at a depth of 10 km. Vp/Vs is also broadly low, and this pattern of Vp/Vs can be seen when the depth is 10 km except in some regions.

At a depth of 30 km, low-Vp zone extends off the east of northeastern Honshu between longitudes of 142 and 143.5 and to the region off the southeast of Hokkaido. High-Vp zone can be seen along the Japan Trench. Two patches of low-Vs zones exist in the east of northeastern Honshu at latitude of 37–40° and longitude of 142–143° and at latitude of 35–36° and longitude of 141–142°. High-Vp/Vs region is bounded by the low-Vp/Vs region, a north–south "stripe" pattern.

At a depth of 40 km, low-Vp and low-Vs zones extend between longitude of 142–143° and latitudes of 37–41°. These low-Vp and low-Vs zones extend to the west of the Hidaka Mountains. High-Vp and high-Vs zones can be seen on the east of the low-V zone and reach the east of the Japan Trench. Vp/Vs in this area is moderate except for some low-Vp/Vs regions with north–south trend.

At a depth of 60 km, low-Vp and low-Vs zones extend just off the coast of the PAC in the northeastern Honshu. High-Vp and high-Vs zones extend broadly on the east of the narrow low-V zone. Vp/Vs in this area is high.

3.4 Velocity structure beneath the Pacific Ocean off Kii and Muroto peninsula beneath the DONET

At depths of 20 and 30 km, low-Vp zones extend around the hypocenters of the large events with magnitude 6.9 and 7.4 that occurred on September 5, 2004. Low-Vs zones partly exist within the low-Vp zone. We cannot resolve the continuous structure from Honshu at depths of 5–10 km since the number of events for seismic tomography beneath the DONET stations is small. This is because the DONET picked data are basically added after the Hi-net manual picking. The seismic tomography will be recalculated when the microearthquake data triggered at DONET stations become available.

3.5 Station corrections

The station corrections for the final model are shown in **Figure 7**. Red stations denote positive O-C travel times. It means that the modeled velocity is too high due to thick sediment or low-V materials since the calculated travel time is too small. It also depends on the depth of borehole of Hi-net stations. The seismometers of the Hi-net stations are typically deployed at depths of around 100–200 m, and low-Vp sediment materials are estimated beneath the backbone range and back-arc side of Japan. Large station corrections are estimated along the Sea of Japan coast in northeastern Honshu since there are thick sediments, while borehole stations are relatively shallow. For Vs, there are many blue-colored stations meaning that the velocity model is too slow. Large station corrections are also estimated on the Sea of Japan side of northeastern Honshu.

For S-net stations, blue stations can be seen near the coast and the Japan Trench. Red stations are shown between them for both Vp and Vs. It suggests that the seismic velocity model is too slow near the coast and the Japan Trench and too fast between them.

For DONET stations, red stations are shown near the coast and blue stations reside off the coast. It means that the modeled seismic velocity is too high near the coast.
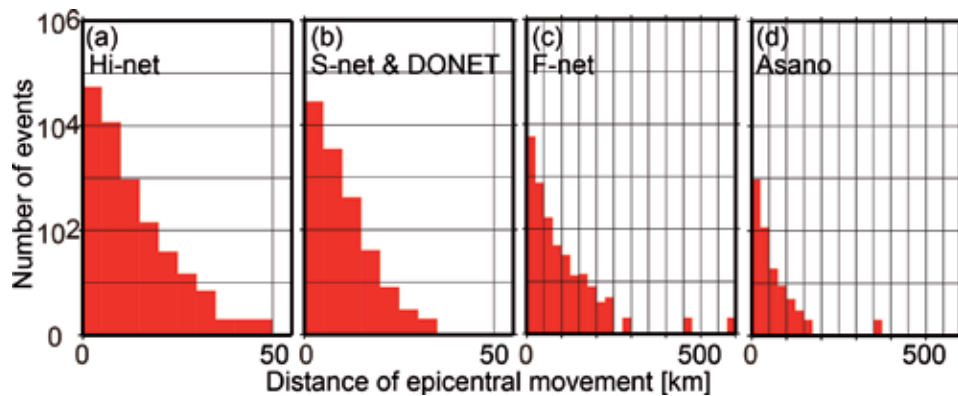
3.6 Movement of hypocenters

Figure 8 shows the histogram of the epicentral movement during the iterations. Epicenters determined by NIED F-net and [20] are shifted over 50 km
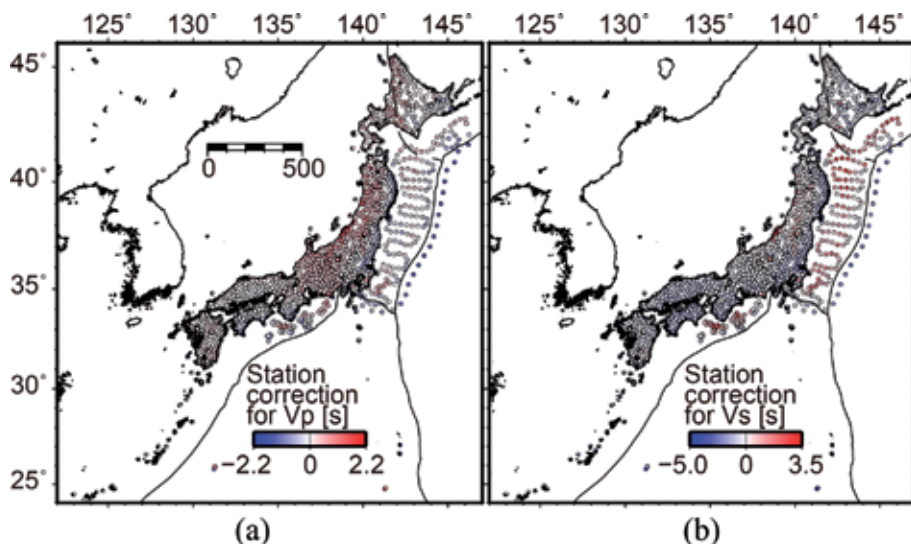
Figure 7.
Station corrections for (a) Vp and (b) Vs.

Figure 8.
Histogram of the earthquake epicentral movements during the inversion. The initial epicenters are determined by (a) NIED Hi-net; (b) NIED Hi-net, S-net, and DONET; (c) NIED F-net; and (d) Ref. [20]. The Hi-net system also uses the seismic stations operated by the other organizations.

after the inversion. Epicenters determined by NIED Hi-net or by NIED Hi-net, S-net, and DONET are mainly less than 10 km in spite of 11 iterations of inversion.

4. Discussion

4.1 Expanded resolved zone from the previous studies

Ref. [14] also clarified the seismic velocity structure beneath the PO at depths of 30–50 km; however, that study could not resolve the shallow structure at depths of 0–20 km since the ray paths, such as head waves, from the oceanic event to the land seismic stations pass through the deep zone. The ray paths from the events to NIED S-net stations run through the shallow part of the PO. In this study, we can clarify the structure at depths of 10–60 km and even east of the Japan Trench at depths of 20–30 km (**Figures 5** and **6**). This is a major improvement enabled by including NIED S-net data

4.2 Characteristic structure of the NS trending high-V and low-V zone off the northeastern Japan

One important feature is the probable Mesozoic rift structure trending NS from the coast of Tohoku to the west of Hidaka Collision Zone. The recent 2018 Hokkaido Eastern Iburi earthquake (M6.7) (Iburi earthquake) occurred at a depth of around 32 km, which is much deeper than the usual inland crustal earthquake. Unfortunately, the structure beneath the PO between the Honshu and Hokkaido islands at a depth of 20 km is not clear; however, a low-Vp zone at a depth of 30 km in north–south direction between 142 and 143° (**Figure 9**) is resolved. Low-Vp zones also exist west of the Hidaka Mountains and between the Honshu and Hokkaido at the northern extension of this low-V zone, although the high-Vp zone parallel to the Japan Trench along the coast of Honshu and Hokkaido invades the low-Vp zone. The high-Vp zone is consistent with the large positive Bouguer gravity anomaly [22] and large positive aeromagnetic anomaly zones [23]. It implies that high-V mantle mafic material is located in the shallow zone. The depth of the Moho is also shallow near the coast of northern Honshu [24]. The Iburi earthquake may be
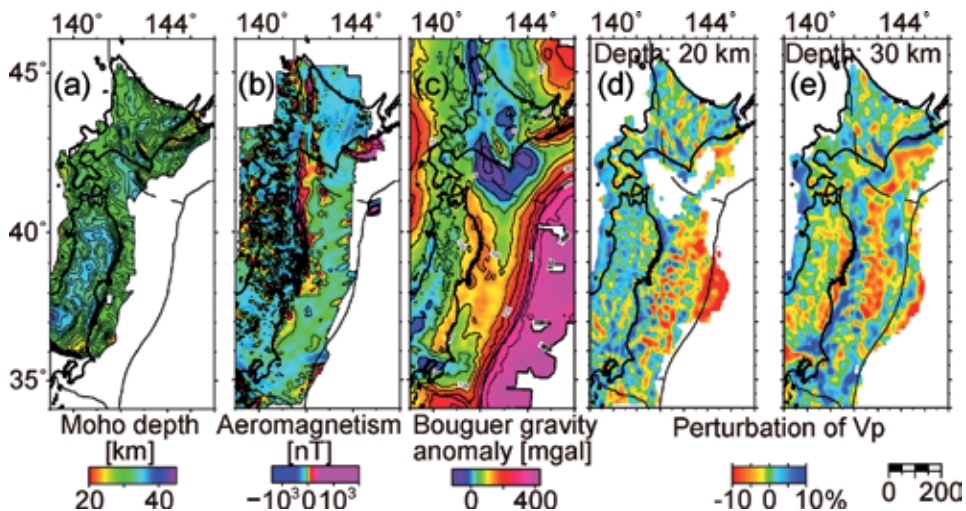
Figure 9.
Map views of (a) Moho depth, (b) aeromagnetism, (c) Bouguer gravity anomaly, Vp perturbation at depths of (d) 20 km and (e) 30 km beneath northern Japan.

related to the reactivation of the rift related to the structure in the upper mantle to the lower crust, where it is marked by high-Vp.

4.3 Characteristic structure along the sea of Japan

We clarified the seismic velocity structure beneath the Sea of Japan at depths of 10–20 km from offshore Hokkaido to Wakasa Bay (**Figure 6**). The Vp beneath the Okushiri and Sado Islands is low at a depth of 10 km; however, Vp beneath the Sea of Japan is high at depths of 10–35 km. Vp along the coast of Sea of Japan in western Japan gives moderate value. The lithospheric velocity structure in this region is strongly affected by the Mid-Tertiary breakup and formation of the Sea of Japan. Through the reactivation of the younger compressed tectonic terrain, tsunamigenic source faults have been developed. The lithospheric structure provides essential information to infer the structure of faults.

4.4 Comparison with the structure obtained by the offshore experiments

Ref. [25] imaged the bending-shaped low-Vp oceanic crust of PAC plate subducting from the Japan Trench at latitudes of 38–38.5° offshore Miyagi where the rupture of large interplate earthquakes propagated. In this study, low-Vp material is imaged at depths of 40–50 km bounded by the high-Vp materials with a number of earthquakes surrounded with red ellipse in **Figure 10**. It indicates the subducting oceanic crust of the PAC plate

The isovelocity contour of Vp = 7.0 km/s lies around depths of 25–40 km. Active-source seismic experiments off Sanriku region imaged the same contour lying at depths of 20–35 km [25] on the west side of Japan Trench, at depths of 15–30 km at the Japan Trench [26], and at depths of 15–25 km in NS direction between Honshu and Japan Trench [27]. The seismic velocity model of this study is relatively slower than those models derived from seismic experiments. The difference may depend on the initial velocity model of the oceanic region being set as the same as the land area in this study. The Moho depth becomes shallower with the EUR crust toward the Japan Trench. The oceanic crust of the PAC plate has also thinner crust than the EUR island arc crust.
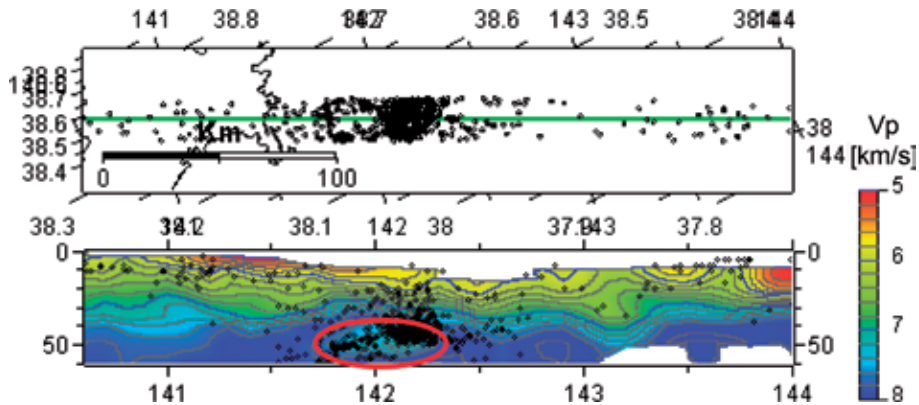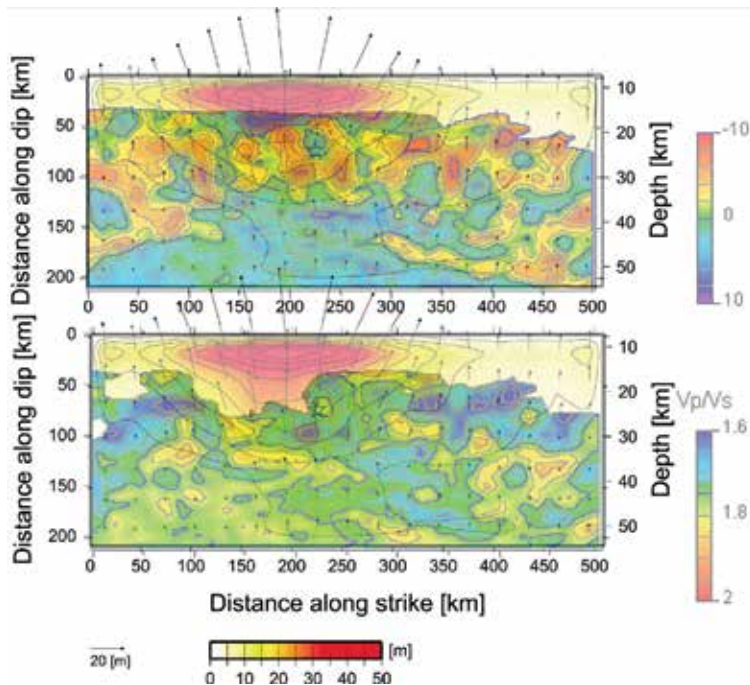
Figure 10.
Vertical cross section beneath the Pacific Ocean off Miyagi in WNW-ESE direction. Black circle shows the relocated hypocenters used for seismic tomography in this study.

4.5 Comparison of velocity structure on the coseismic slip plane of the Tohoku-oki event

Figure 11 shows the Vp perturbation just above the upper boundary of the PAC plate within the overriding EUR plate. The plane with the upper side at surface has a dip angle of 15°. Reference [28] also showed the Vp perturbation [29] above the upper boundary of the subducting PAC slab and three low-V zone offshore Sanriku, Miyagi, and Ibaraki. In our results, we obtain velocity structure in fine scale; however, we do not estimate the shallow structure along the Japan Trench. We obtain the broad low-Vp and low-Vp/Vs zone within the overriding EUR plate between the Japan Trench and Honshu. A high-Vp and slightly high-Vp/Vs zone exists on the
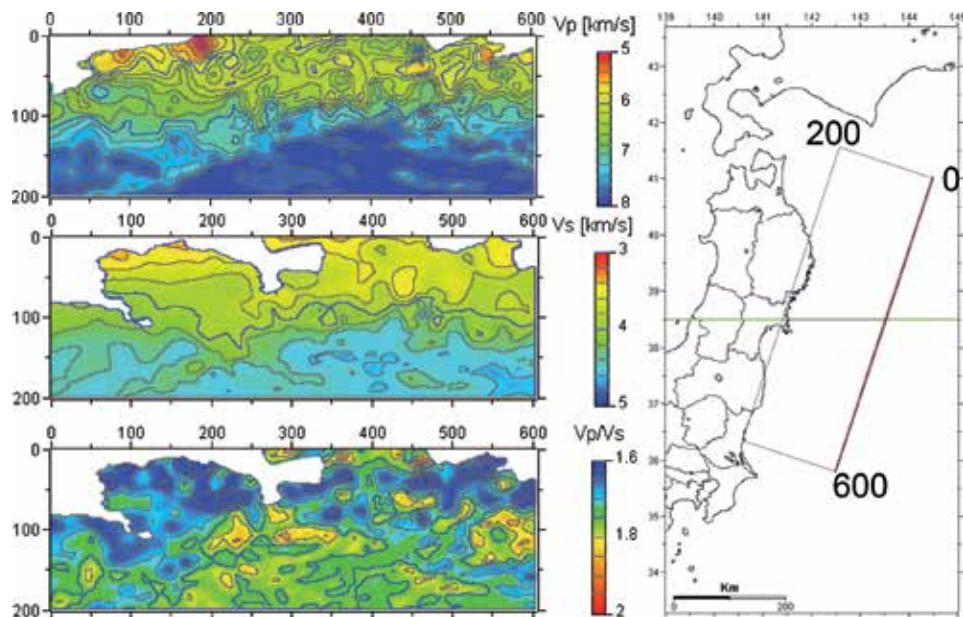
Figure 11.
Vp perturbation on the plane just above the upper boundary of the PAC plate within the overriding EUR plate. The plane has strike with S17degW from the point with a longitude of 144.5 and a latitude of 41.0 with dip angle of 12 deg. The depth of the upper edge of the plane is 10 km.

Figure 12.
(a) Vp perturbation and (b) Vp/Vs on the coseismic slip plane [30].

west side of the low-Vp and low-Vp/Vs zone. There are some small high-V zones within the low-V zone near the hypocenter of the Tohoku-oki event.

Figure 12 also shows the Vp perturbation and Vp/Vs on the coseismic plane of the Tohoku-oki event [30]. We do not obtain the shallow structure along the Japan Trench although the extremely large slip of the Tohoku-oki event is estimated near the Japan Trench. The western edge of the large slip zone is consistent with the high-Vp zone; however, the surrounding region has low-Vp and low-Vp/Vs. Low-Vp/Vs material is difficult to deform so that it can generate large elastic waves if it fails. Low-Vp/Vs on the coseismic slip region may be one of the reasons for the extreme size of the Tohoku-oki event.

5. Conclusion

We conducted the seismic tomography for entire Japanese Islands including oceanic area. This is the first tomographic study to use the data from NIED S-net. The hypocenters of oceanic events are greatly improved using the S-net data. We also obtain the detailed seismic velocity structure beneath the PO at depths of 10–60 km. Low-Vp and low-Vs zones are revealed between 142 and 143° at a depth of 30 km and in western Hokkaido where the Eastern Iburi Earthquake in 2018 occurred. The lithospheric velocity structure on the coast of Sea of Japan on Honshu is strongly affected by the Mid-Tertiary breakup and formation of the Sea of Japan. Tsunamigenic source faults have been developed through the reactivation of the younger compression. Subducting low-V oceanic crust is imaged within the mantle of overriding EUR and subducting oceanic PAC plate. The coseismic slip plane of the Tohoku-oki event has low-Vp/Vs; however, the shallow structure along the Japan Trench will be improved in the future with increased data. Previous seismic reflection and refraction studies found the oceanic crust at the uppermost part of the PAC

plate with Vp of approximately 6–7 km/s; however, the seismic tomography with NIED S-net clarified the 6–7 km/s Vp zone at depths of 25–40 km. The result may depend on the initial velocity model beneath the PO, which was the same initial model as the land area in this study. Applying the initial velocity model derived from the refraction or reflection seismology would improve the results beneath the ocean in the future.

Acknowledgements

Author details

Makoto Matsubara[1*], Hiroshi Sato[2], Kenji Uehira[1], Masashi Mochizuki[3], Toshihiko Kanazawa[4], Narumi Takahashi[1], Kensuke Suzuki[5] and Shin'ichiro Kamiya[1]

1 National Research Institute for Earth Science and Disaster Resilience, Tsukuba, Japan

2 Earthquake Research Institute, The University of Tokyo, Bunkyo, Japan

3 Ministry of Education, Culture, Sports, Science and Technology, Chiyoda, Japan

4 Association for the Development of Earthquake Prediction, Chiyoda, Japan

5 Japan Agency for Marine-Earth Science and Technology, Yokohama, Japan

*Address all correspondence to: mkmatsu@bosai.go.jp

IntechOpen

References

[1] National Research Institute for Earth Science and Disaster Resilience, NIED Hi-net, National Research Institute for Earth Science and Disaster Resilience. DOI: 10.17598/NIED.0003

[2] Obara K, Kasahara K, Hori S, Okada Y. A densely distributed high-sensitivity seismograph network in Japan: Hi-net by National Research Institute for Earth Science and Disaster Prevention. Review of Scientific Instruments. 2005;**76**:021301. DOI: 10.1063/1.1854197

[3] National Research Institute for Earth Science and Disaster Resilience, NIED F-net, National Research Institute for Earth Science and Disaster Resilience. DOI: 10.17598/NIED.0005

[4] Okada Y, Kasahara K, Hori S, Obara K, Sekiguchi S, Fujiwara H, et al. Recent progress of seismic observation networks in Japan-Hi-net, F-net, K-NET and KiK-NET. Research News Earth Planets Space. 2004;**56**:xv-xxviii

[5] National Research Institute for Earth Science and Disaster Resilience, NIED DONET, National Research Institute for Earth Science and Disaster Resilience. DOI: 10.17598/NIED.0008

[6] National Research Institute for Earth Science and Disaster Resilience, NIED S-net, National Research Institute for Earth Science and Disaster Resilience. DOI: 10.17598/NIED.0007

[7] Kanazawa T. Japan trench earthquake and tsunami monitoring network of cable-linked 150 ocean bottom observatories and its impact to earth disaster science. In: IEEE International Underwater Technology Symposium (UT). IEEE; 2013. pp. 1, 2013-5

[8] Uehira K, Kanazawa T, Mochizuki M, Fujimoto H, Noguchi S, Shinbo T, et al. Outline of seafloor observation network for earthquakes and tsunamis along the Japna trench (S-net). EGU General Assembly. 2016;**2016**:EGU2016-EG13832

[9] National Research Institute for Earth Science and Disaster Resilience, NIED K-NET, KiK-net, National Research Institute for Earth Science and Disaster Resilience. DOI: 10.17598/NIED.0004

[10] National Research Institute for Earth Science and Disaster Resilience, NIED V-net, National Research Institute for Earth Science and Disaster Resilience. DOI: 10.17598/NIED.0006

[11] Zhao D, Hasegawa A, Horiuchi S. Tomographic imaging of P and S wave velocity structure beneath northeastern Japan. Journal of Geophysical Research. 1992;**97**:19,909-19,928

[12] Matsubara M, Obara K, Kasahara K. Three-dimensional P- and S-wave velocity structures beneath the Japan Islands obtained by high-density seismic stations by seismic tomography. Tectonophysics. 2008;**454**:86-103. DOI: 10.1016/j.tecto.2008.04.016

[13] Matsubara M, Obara K. The 2011 off the Pacific coast of Tohoku earthquake related to a strong velocity gradient with the Pacific plate. Earth, Planets and Space. 2011;**63**:663-667

[14] Matsubara M, Sato H, Uehira K, Mochizuki M, Kanazawa T. Three-dimensional seismic velocity structure beneath Japanese Islands and surroundings based on NIED seismic networks using both inland and offshore events. Journal of Disaster Research. 2017;**12**:844-857. DOI: 10.20965/jdr.2017.p0844

[15] Matsubara M, Hirata N, Sato H, Sakai S. Lower crustal fluid distribution in the northeastern Japan arc revealed by

high resolution 3D seismic tomography. Tectonophysics. 2004;**388**:33-45. DOI: 10.1016/j.tecto.2004.07.046

[16] Matsubara M, Hayashi H, Obara K, Kasahara K. Low-velocity oceanic crust at the top of the Philippine Sea and Pacific plates beneath the Kanto region, Central Japan, imaged by seismic tomography. Journal of Geophysical Research. 2005;**110**:B12304. DOI: 10.1029/2005JB003673

[17] Nolet G. Seismic Tomography. D. Reidel Publishing Company; 1987. p. 386

[18] Ukawa M, Ishida M, Matsumura S, Kasahara K. Hypocenter determination method of the Kanto-Tokai observational network for microearthquakes (in Japanese with English abstract). Research Notes National Research Center Disaster Prevention. 1984;**53**:1-88

[19] Matsubara M, Obara K, Kasahara K. High-Vp/vs zone accompanying non-volcanic tremors and slow slip events beneath southwestern Japan. Tectonophysics. 2009;**472**:6-17. DOI: 10.1016/j.tecto.2008.06.013

[20] Asano Y, Saito T, Ito Y, Shiomi K, Hirose H, Matsumoto T, et al. Spatial distribution and focal mechanisms of aftershocks of the 2011 off the Pacific coast of Tohoku earthquake. Earth, Planets and Space. 2011;**63**:669-673. DOI: 10.5047/eps.2011.05.018

[21] Inoue H, Fukao Y, Tanabe K, Ogata Y. Whole mantle P-wave travel time tomography. Physics of the Earth and Planetary Interiors. 1990;**59**:294-328

[22] Geological Survey of Japan. Gravity Database of Japan. DVD edition, Digital Geoscience Map P-2. Geological Survey of Japan, AIST. 2013

[23] Nakatsuka T, Okuma S. Aeromagnetic Anomalies Database of Japan. Digital Geoscience Map P-6. Geological Survey of Japan. 2005

[24] Matsubara M, Sato H, Ishiyama T, Van Horne AD. Configuration of the Moho discontinuity beneath the Japanese Islands derived from three-dimensional seismic tomography. Tectonophysics. 2017;**710-711**:97-107. DOI: 10.1016/j.tecto.2016.11.025

[25] Ito A, Fujie G, Miura S, Kodaira S, Kaneda Y, Hino R. Bending of the subducting oceanic plate and its implication for rupture propagation of large interplate earthquakes off Miyagi, Japan, in the Japan trench subduction zone. Geophysical Research Letters. 2005;**32**:L05310. DOI: 10.1029/2004GL022307

[26] Obana K, Fujie G, Takahashi T, Yamamoto Y, Tonegawa T, Miura S, et al. Seismic velocity structure and its implications for oceanic mantle hydration in the trench-outer rise of the Japan trench. Geophysical Journal International. 2019;**217**:1629-1642. DOI: 10.1093/gji/ggz099

[27] Fujie G, Kodaira S, Yamashita M, Sato T, Takahashi T, Takahashi N. Systematic changes in the incoming plate structure at the Kuril trench. Geophysical Research Letters. 2012;**40**:88-93. DOI: 10.1029/2012GL054340

[28] Zhao D, Huang Z, Umino N, Hasegawa A, Kanamori H. Structural heterogeneity in the megathrust zone and mechanism of the 2011 Tohoku-oki earthquake (Mw 9.0). Geophysical Research Letters. 2011;**38**:L17308. DOI: 10.1029/2011GL048408

[29] Huang Z, Zhao D. Mechanism of the 2011 Tohoku-oki earthquake (Mw 9.0) and tsunami: Insight from seismic tomography. Journal of Asian Earth Sciences. 2013;**70-71**:160-168

[30] Suzuki W, Aoi S, Sekiguchi H, Kunugi T. Rupture process of the 2011 Tohoku-Oki mega-thrust earthquake (M9.0) inverted from strong-motion data. Geophysical Research Letters. 2011;**38**:L00G16. DOI: 10.1029/2011GL049136

[31] Wessel P, WHF S. New version of generic mapping tools released. EOS Transactions. 1995;**79**:329

[32] Matsubara M. Software for viewing 3D velocity structures beneath whole Japan Islands. Report of the National Research Institute for Earth Science and Disaster Prevention. 2010;**76**:1-9

Low-Frequency Electromagnetic Signals Observed before Strong Earthquakes

Igor I. Rokityansky, Valeriia I. Babak and Artem V. Tereshyn

Abstract

We consider two kinds of signals preceding earthquake (EQ): intensification of internal electromagnetic (EM) field – lithosphere emission (LE) and change of the Earth interior response function (RF). Several cases of LE before strong EQs were reviewed and analyzed, and preliminary portrait of LE precursor was compiled. LE can appear several times with lead time month(s), weeks, days, and hours and can attain amplitude of several hundreds of nT which not uniformly decreases with increasing distance from the source. Typical LE frequency content/maximum is 0.01–0.5 Hz. Data of 19 Japanese geomagnetic observatories for 20 years preceding the Tohoku EQ on March 11, 2011 were analyzed, and RFs (mainly induction vector) were calculated. At six observatories in 2008–2010, anomalous variations of RF were separated which can be identified as middle-term precursors. Applying the original method developed in Ukraine, a short-term two-month-long precursor of bay-like form was separated by phase data of observatory KNZ in the Boso peninsula where electrical conductivity anomaly was also discovered. Hypothetical explanation based on tectonic data is advanced: Boso anomaly connects two large-scale conductors—Pacific seawater and deep magma reservoir beneath a volcanic belt. Between two so different conductors, an unstable transition zone sensitive to changes of stress before strong EQs can be expected.

Keywords: geomagnetic field, lithosphere emission, conductivity structure, induction vector, earthquake precursor

1. Introduction

One of the long lasting challenges for the Earth sciences is earthquake (EQ) prediction. EQ precursors deliver unique information which is necessary for the solution of two interconnected fundamental problems—EQ prediction (humanitarian practical aspect) and support to the development of EQ theory (scientific aspect).

The history of the EQ precursor study goes back to antiquity. But even now their study remains purely empirical, and any precursor even recorded with perfect instrument can be treated as not related with seismicity (skepticism to prediction widely spread now), and it is difficult to prove that it is genuine EQ precursor because physics of EQ preparation process is still not well understood. The causes of such situation are (1) the complexity of the real Earth and processes

in it, (2) the absence of direct information from the place of EQ preparation, nucleation, and occurrence in the Earth interior. Nevertheless, consider the unique case of the successful EQ prediction—Haicheng prediction.

1.1 Haicheng EQM7.3

The Haicheng EQM7.3 occurred on February 4, 1975 at 19:35 local time in northeast China. After 1965, activation of seismicity occurred in an area of 120 km to SSW from Beijing with several destructive EQsM > 6. After this *long-term prediction*, the Chinese government greatly strengthened EQ study and precursor monitoring (telluric currents, well water, animal behavior, and other phenomena related with EQ) attaching to observation experts and also amateurs and scholars. Many precursors were observed in 1973 and 1974 in a large area of 200 × 300 km (*middle-term precursors*) which in December 1974–January 1975 concentrated in a smaller area. In January 1975, quiescence of seismicity was observed but anomalies of groundwater, telluric currents, radon, tilt, animal behavior, etc. increased till January 23 (*short-term precursors*), then slightly decreased, and since February 1 rouse in hundreds times. From 16:00, February 3, to 18:30, February 4, 500 EQs with M up to 4.2 occurred in the area between Yingkou and Haicheng cities. They were interpreted as foreshocks of strong EQ. Emergency evacuation was ordered by authorities, and law-abiding Chinese left their houses. At 19:36, a devastating EQ struck dozens of cities including Haicheng with almost 1 million inhabitants. Thousands of buildings collapsed, but hundred thousand lives have been saved by the well-timed prediction. Instructive lessons from successful Haicheng prediction are (1) continuous transition from long−/intermediate-term prediction to short/immediate ones with consistent improvement of expected EQ time, place, and magnitude; (2) close cooperation of authorities, scientists, amateurs, and mass media; and (3) the use of all available precursors, including "nonscientific" ones as animal behavior [1].

Multiparameter monitoring and strong scientific efforts of the last decades reveal some unexpected features of precursors: (1) Long-distance appearance up to thousands km from EQ epicenter. (2) Spatial selectivity: EQ precursors can be observed in some sensitive zones (usually fault zones) and be not observable in vast territories even not far from impending EQ. (3) Spatial–temporal migration of precursors: initially it appears in one locality, and then it appears in the next locality, usually with changed parameters. Such features did not find explanation in the framework of simple dominant ideas in the middle of the twentieth century about geological media. These features evidenced the complexity of geological media, and in the second half of the twentieth century, several new concepts have appeared to explain new data (Sadovsky MA, Varotsos P, Gufeld IL and many others).

For effective EQ prediction, we need automatic system of monitoring, processing, and analysis of all observed precursory parameters, their cross-correlation analysis to estimate probability of expected EQ (taking into account all previous global, regional, and local analyzes). High-level scientific team must keep contact with decision-making authorities for providing public announcement of the EQ prediction and plan of emergency measures. Such system needs great funds. Some elements of such system are created in few regions (California, China, ex-USSR countries).

1.2 Goal and scope of the chapter

Multitude of EQ precursors is the unique base for EQ prediction. Complexity of the earth and poor understanding of seismicity process enforce us to use as many

kinds of precursors as possible. Two approaches are perspective for the fishing of the precursory signals from geomagnetic data: (1) Direct observation of the lithosphere emission (LE) of the internal electromagnetic fields arising in the course of EQ preparation and nucleation process and (2) transformation of the time series of the observed three components of geomagnetic field into time series of response functions of the Earth's interior conductivity.

In the next sub-section, we review few case stories of the most reliable records of ultralow-frequency (ULF) LE.

In Section 2, we shortly outline the rather sophisticated methodology of response function (RF) approach referring for details to few monographs [2–5].

In Sections 3 and 4, we apply RF method to the Japanese geomagnetic observatories data in the attempt to separate the precursors of great Tohoku EQM9 11.03.2011, wherein obtained quite reliable result on the Boso conductivity anomaly and advance its tectonic interpretation.

In Section 5, we discuss the results obtained.

In Section 6, we summarize the results and give the recommendations for the improvement of the low-frequency EM precursor study.

1.3 Case stories of LE records before strong EQs

There are many reports on LE registration, in particular before EQs. Consider fortunate cases when EM observations turned out to be located in the places where LE field was well above magnetotelluric (MT) field+noise background and can be easily identified.

1.3.1 Great Alaska EQM9.2 on March 28, 1964

Geomagnetic observatory in the city of Kodiak was located in the distance of 440 km from the epicenter of the EQ and only in 30 km from the fault zone along which displacement occurred. The full field proton magnetometer recorded several magnetic disturbances. The strongest one with intensity 100nT appeared 1 h 06 min before the EQ [6].

1.3.2 Loma Prieta EQM7.1 on October 18, 1989

One of the most convincing cases of LE precursors was recorded before that EQ [7]. The monitoring system of Stanford University (created for traffic noise study) operated since October 1987 at the distance of 7 km from the future EQ epicenter. The system included induction coils and special computer which calculated half-hourly averages of the magnetic field power spectra in each of nine narrow frequency bands covering the overall range 0.01–10 Hz.

During 23 months record was normal with low noise. After September 12, 1989, anomalous signal began to appear in two frequency bands: 0.05–0.1 and 0.1–0.2 Hz and grew up to 1.5 nT. In October 5, a large increase of amplitude appeared at all frequencies with the strongest one at the lowest frequency 0.01 Hz, where it reached 30 times the normal level. On the last several days before EQ, anomaly gradually diminishes (a quiescence!), and 3 h before the EQ, very large amplitude appeared only at periods longer 0.5 Hz, exceptionally large at frequency 0.01 Hz. We must emphasize that instrumentation of Stanford University which allowed to get results every half an hour is very good for LE monitoring. Unfortunately, it did not continue the operation for EQ prediction.

1.3.3 Caucasus

Kopytenko et al. [8, 9] developed three-component magnetometers for frequency range 0.005–10 Hz. The first instrument started the record 23 days before destroying Spitak EQM6.9 at 7.41 UT, on December 7, 1988, in geomagnetic observatory at Dusheti, 129 km to the north from the EQ epicenter. It recorded intensive B_{LE} which started 4 h prior the EQ (**Figure 1a, b**).

In the time interval November 14, 1988 to March 5, 1989 in frequency range 0.1–1 Hz 59 unusual noise-like bursts of LE with an amplitude well higher the background noise (0.03 nT) and the duration ranging from several minutes to several hours (mean duration ≈30 min) were recorded mainly before the strong aftershocks. Decrease in aftershock activities and B_{LE} activity was quite synchronous.

The next strong event was Racha EQM6.9 at 9.13 UT, on April 29, 1991, occurred at the epicentral distance of 90 km from Dusheti where no pronounced B_{LE} were recorded. It means that Dusheti is not a sensitive place for the EQs in Racha region (effect of spatial selectivity). Kopytenko's team organized B_{LE} observations in two field sites Nik and Oni for June–July 1991—the time of Racha aftershock activities. Forty-seven B_{LE} with intensity up to 2 nT and duration ranging from several minutes to several hours were observed at both observatories, 23 of them were recorded 1–4 days before the strong aftershock M6.2 on June 15,1991. **Figure 1c** presents B_{LE} bursts observed before aftershock M4.0. The distance from the epicenter to Oni was two times smaller than to Nik, but intensity of LE signal at Nik was considerably larger: for H component in 10–20 times, for D in 1.3–2 times, and for Z in 5–7 times. It means strong spatial selectivity of the LE signals preceding EQ [10, 11].
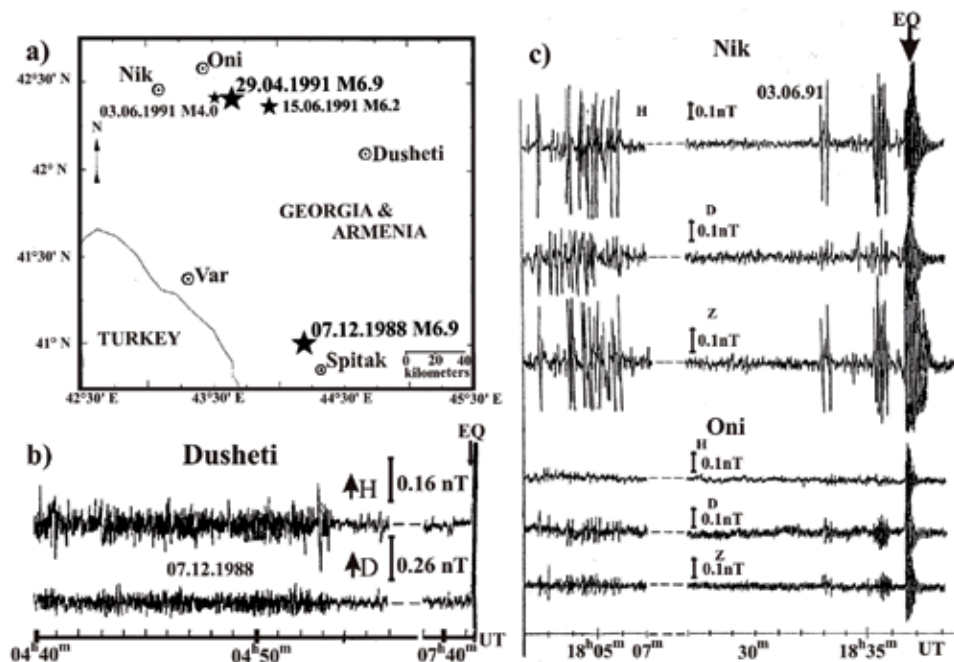
Figure 1.
B_{LE} *preceded some EQs in Caucasus [8, 9]. (a) Map of seismoactive region with the sites of observation and epicenters (given by stars) of the events discussed in text. (b) Final fragment of B_{LE} record started 4 h before Spitak EQ and abruptly terminated 2 h 48 min before it. (c) Several short B_{LE} bursts records during 33 min before aftershock M4.0 at field stations Nik and Oni located at the distance 34.6 and 16.9 km from the epicenter correspondingly.*

In the conclusion we like to emphasize that magnetometers in described studies can register variations in the frequency band of 0.005–10 Hz, but they recorded most intensive B_{LE} at the frequencies 0.1–1 Hz that differs from the result in Loma Prieta, where the maximum tends to their lowest frequency 0.01 Hz.

1.3.4 Taiwan

The island-wide geomagnetic network consisted of three-component geomagnetic observatory LP in the seismically quiet area and seven full field stations equipped by proton magnetometers with 0.1 nT sensitivity and sampling rate of 10 min distributed in areas of high seismicity [12]. Chi-Chi EQM7.6 occurred on September 21, 1999, in the middle of Taiwan. Stations LY turned out to be just near to surface rupture of the EQ along Chelungpu fault and recorded the strongest LE which clearly separated from comparison with records of remote observatory LP. LE begun more than a month before the EQ and attained in maximum 200 nT, and then its amplitudes gradually weakened, and the disturbance level reduced to that of a quiet period almost right after the second strong Chia-Yi EQM6.4 that occurred near the southern end of the Chelungpu fault on October 22, 1999 [12].

1.3.5 Greece

In Greece in the early 1980s for the registration of the LE electric components, the so-called seismic electric signals (SES) special network was created by Prof.
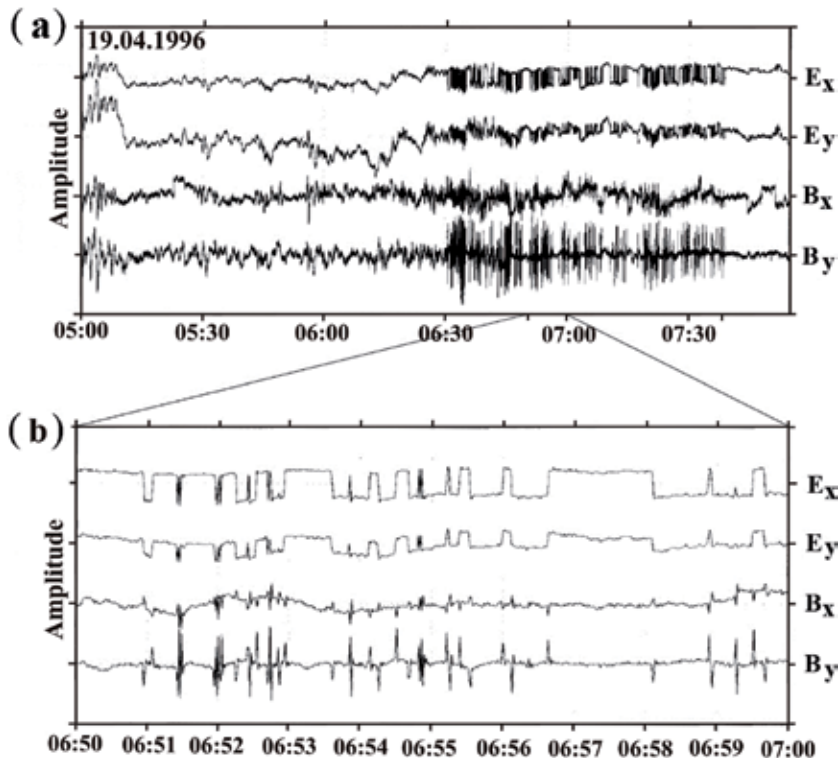
Figure 2.
The SES activity on April 19, 1995, before the Grevena-Kozani EQM6.6 on May 13, 1995, recorded in Greece at the IOA observatory at the distance of 80 km from the epicenter with a sampling rate of 1 sample/s: (a) 3 h record with strong SES activity in 6.30–7.40 time interval, (b) is the 5 min fragment of (a), showing both electric and magnetic components in expanded time scale [11]. Amplitudes are given in relative units.

P. Varotsos [11, 13]. The network consists of 10–15 stations. Each station included several (from 6 up to 100) grounded electrical dipoles with the length from 50 m up to 20 km that allows to study spatial characteristics of observed field and separate SES from MT field and noise. In the course of continuous monitoring for more than 35 years, Prof. Varotsos and collaborators identified (as the result of a posteriori analysis) many SES before the following EQs and studied their regularities [11], for example, the selectivity effect: SES can be observed in some sensitive zones and be not observable in vast territories even not far from impending EQ. Prof. Varotsos made a number of correct EQ predictions registered officially before the event. We show interesting case of joint registration SES and horizontal magnetic components recorded on April 19, 1995, 25 days before Grevena-Kozani EQM6.6 on May 13, 1995 (**Figure 2**). Magnetic components look as derivative of electrical impulses that are clearly seen in the lower graph (b) with expanded time scale. In the latter years, Prof. Varotsos' group develops deeper insight in the physics of LE: entropy and natural time analysis for the better understanding of the EQ preparation process and for the distinguishing LE signals from similarly looking variations of MT and noise origin [14, 15].

2. Basic concepts and definitions. Methodology

2.1 Varying geomagnetic field

Varying geomagnetic field $\mathbf{B}(t) = B_x\mathbf{e_x} + B_y\mathbf{e_y} + B_z\mathbf{e_z}$ (where $\mathbf{e_x}$, $\mathbf{e_y}$, and $\mathbf{e_z}$ are unit vectors directed to north, east, and downward correspondingly) continuously exists in and around the Earth and is recorded nowadays digitally with a time reading interval Δt (1 min or 1 s in our study). All components are functions of time t which we skip out for brevity.

2.2 Main sources of observed geomagnetic field

$$\mathbf{B}(t) = \mathbf{B}_{MT} + \mathbf{B}_{noise} + \mathbf{B}_{LE}, \qquad (1)$$

where $\mathbf{B}_{MT} = \mathbf{B}_{MT}ext + \mathbf{B}_{MT}intn + \mathbf{B}_{MT}inta$ is the magnetotelluric field.

$\mathbf{B}_{MT}ext$ is the external primary magnetic field of the currents in magnetosphere and ionosphere of the Earth.

$\mathbf{B}_{MT}intn$ is the normal internal secondary magnetic field of the currents induced by $\mathbf{B}_{MT}ext$ in the Earth's interior having a hypothetical "normal" horizontally layered conductivity structure. The horizontal components of $\mathbf{B}_{MT}intn$ add together with $\mathbf{B}_{MT}ext$ increasing observed horizontal MT-field up to doubling over hypothetical ideally conducting Earth. On the contrary, the vertical component of $\mathbf{B}_{MT}intn$ subtracts from $\mathbf{B}_{MT}ext$ diminishing observed normal vertical MT field up to 0 (phase neglected).

Thus, $\mathbf{B}_{MT}n = \mathbf{B}_{MT}ext + \mathbf{B}_{MT}intn$ has the horizontal component much greater than the vertical one and embraces great territory equal to external source field dimension.

$\mathbf{B}_{MT}inta$ is the anomalous internal secondary field arising on local/regional conductivity anomalies as a result of redistribution of the currents responsible for $\mathbf{B}_{MT}intn$.

Such subdividing of secondary internal field is rather artificial, but it is used in geoelectromagnetic methods: $\mathbf{B}_{MT}intn$ in sounding methods, magnetotelluric sounding (MTS) and geomagnetic deep sounding (GDS); $\mathbf{B}_{MT}inta$ in profiling one, magnetic variation profiling (MVP) [2–5].

Bnoise is the ever-present noise, both man-made and natural.

B$_{LE}$ is the purely internal field of lithosphere emission, it is usually local and transient, and the ratio of vertical component to the horizontal one usually differs from the same ratio for MT field.

After the conventional processing using Fourier transform, a **B**(t) record of duration t_2-t_1 is transformed into a superposition of harmonic components with periods $T_1, T_2...T_n$.

2.3 Response function

Response function is the term widely used in natural sciences and mathematics. In the geoelectromagnetic studies of *electrical conductivity* σ (x, y, z) of the Earth's interior [2–4], the RFs are supposed to be some functions derived from the Earth's electromagnetic (EM) data that provides us with a possibility to determine the conductivity structure of the Earth. EM RFs are usually frequency/(period T) dependent, and then they are complex functions having real (index u) and imaginary (index v) parts. We use two of these functions.

2.3.1 Induction vector

Induction vector C = A**e**$_x$ + B**e**$_y$ (A and B are determined from the linear equation: B$_z$ = AB$_x$ + BB$_y$). Real induction vectors **C**$_u$ = A_u**e**$_x$ + B_u**e**$_y$ possess an important property: in the notation of Wiese used here, they are directed away from a good conductor.

2.3.2 Anomalous horizontal magnetic variation tensor

Anomalous horizontal magnetic variation tensor [M] is determined from the linear system of equations B$_x$(**r**$_i$) = M$_{xx}$B$_x$(**r**$_0$) + M$_{xy}$B$_y$(**r**$_0$) and B$_y$(**r**$_i$) = M$_{yx}$B$_x$(**r**$_0$) + M$_{yy}$B$_y$(**r**$_0$), where **r**$_0$ and **r**$_i$ are coordinates of base (reference) and some other observation place. Tensor [M] reflects the change in geoelectric structures between two places (if the source field used is uniform).

2.4 The processing of observed geomagnetic field

The processing of observed geomagnetic field **B**(t) for the monitoring of geodynamic and other environmental processes implies transformation of three components of geomagnetic field time series with time reading interval Δt (1 min or 1 s in our study) into a variety of time series with temporal resolution $\Delta\tau$ ($\Delta\tau$»Δt) of different RF components: *Re* and *Im* and *x* and *y* at the set of periods $T_1, T_2...T_n$ of received harmonics (Δt « T_i « $\Delta\tau$).

2.5 The theory of geoelectromagnetic methods

The theory of geoelectromagnetic methods [2–4] is developed for natural source field in the form of vertically incident plane wave (Tikhonov-Cagniard (T-C) model), which usually holds for an external source field of magnetosphere-ionosphere origin (named as magnetotelluric field) for the periods less than 10^4 s. Ideally RF depends only on the Earth's conductivity distribution which is sensitive to the stress variations and therefore to geodynamic processes including the earthquake preparation.

3. Variations of geomagnetic response functions (mainly induction vector) before the 2011 Tohoku earthquake

RFs and their variations, especially in relation with EQs preparation, were studied in Japan for many years and were described in many works among which we cite only few [16–18]. In the last two decades, the RF approach became less used for EQ studies because of strong noise at Japanese observatories. After the catastrophic Tohoku EQ on March 11, 2011, near Japan, we analyzed the available geomagnetic data to obtain some EQ precursors using the RF method. Some results were presented in Russian [19–21], which together with the latest results of our study will be summarized below.

Data used: We obtained data of 17 Japanese geomagnetic observatories (**Figure 3**, **Table 1**) for time interval of 12–20 years with temporal reading every 1 min (and few observatories with 1 s reading). For the conversion of geomagnetic field **B** time series into RF time series, we used the advanced multi-window remote reference (rr) robust programs with coherency control [22, 23]. After processing we got values of four components of induction vector A_u, B_u, A_v, B_v for each day for five period intervals centered at: 225, 450, 900, 1800, and 3600 s. To reduce the great scattering, everyday values were smoothed with moving windows and/or were found average or median values for some interval (usually 1 month).

3.1 Results of processing for separation of middle-term precursors

Analyzing large material of processed data for 15 years from 2001 till 2015, we found that aperiodic variations (or enhancement of annual variation) of induction vectors were observed at periods 225, 450, and 900 s during 3–5 years before the Tohoku EQ at stations: HAR, KAK, OTA, KNZ, and TTK, most clearly at period 450 s presented in **Figure 4**. We should emphasize that no such aperiodic variations were observed at other stations including ESA and MIZ, which are the nearest to the EQ epicenter. The best correlation of middle-term anomalies is observed between the two most remote (620 km) from each other stations HAR and TTK: at both we see strong synchronous variations of induction vectors with maxima in the end of 2008, the end of 2009, with several maxima in 2010, in the beginning of 2011, and
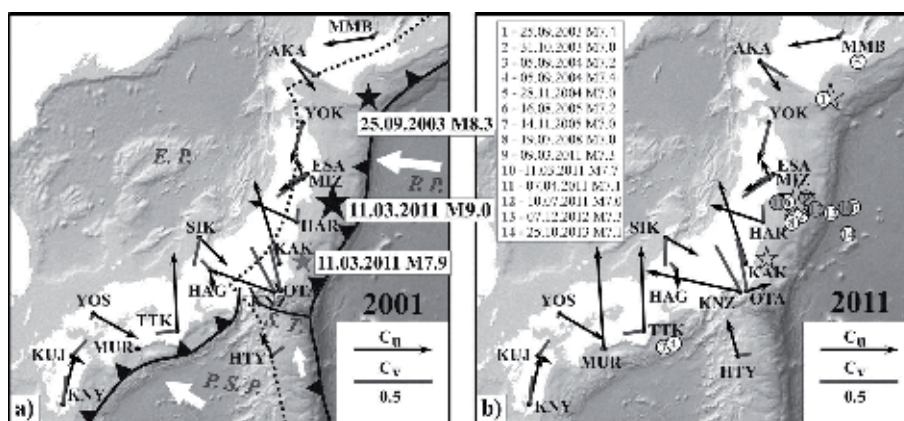
Figure 3.
Map of Japan with real C_u and imaginary C_v induction vectors for the period 450 s at 17 geomagnetic observatories by 1 min record data. (a) Mean vectors for the year 2001. Stars present EQs with M > 7.8 since 2001. Elements of plate tectonics; white arrows represent the directions of plate motions; E. P., Eurasian plate; P. P., Pacific plate; P. S. P., Philippine Sea plate; S. T., Sagami trough; dotted line, volcanic front. (b) Mean vectors for 2011. Circles present EQs with M ≥ 7. The depth of hypocenters is less than 50 km for all EQs.

| Code	Station name	Geom. lat.	Geom. long.	Geogr. lat.	Geogr. long.	Processed years
MMB	Memambetsu	35.44	148.24	43.910	144.189	1993–2012
AKA	Akaigawa	34.31	151.09	43.072	140.815	2001–2012
YOK	Yokohama	32.28	150.43	40.993	141.240	2001–2012
ESA	Esashi	30.55	150.09	39.237	141.355	1997–2012
MIZ	Mizusawa	30.41	150.21	39.112	141.204	1997–2015
HAR	Haramachi	28.90	150.25	37.615	140.953	2001–2015
SIK	Shika	28.04	153.96	37.082	136.773	2001–2012
KAK	Kakioka	27.47	150.78	36.232	140.186	1956–2015
HAG	Hagiwara	26.98	153.47	35.985	137.186	2001–2012
OTA	Otaki	26.54	150.63	35.292	140.230	2001–2015
KNZ	Kanozan	26.48	150.87	35.256	139.956	1996–2016
YOS	Yoshiwa	25.12	157.87	34.476	132.176	2001–2012
TTK	Totsukawa	24.83	154.52	33.932	135.802	2001–2015
HTY	Hatizyo	24.30	150.75	33.073	139.825	1991–2008
MUR	Muroto	24.10	155.99	33.319	134.122	2004–2012
KUJ	Kuju	23.65	158.58	33.061	131.260	2001–2015
KNY	Kanoya	22.00	158.80	31.424	130.88	1991–2016

Table 1.
Geomagnetic observatories in Japan used in the study.

return to the previous level after the Tohoku EQ. We may suppose that these aperiodic variations can be the middle-term precursors of the Tohoku EQ. These observatories are located not at the shortest distance from the EQ, which is in agreement with well-known phenomenon of spatial selectivity of EQ precursors known during the centuries for hydrological precursors and recently proven for LE registered in the form of seismic electric signal [11, 13].

Having 1 min time series, we can analyze only geomagnetic variations with period T > 3 min, and the most interesting shorter part of ULF spectra (0.01–10 Hz), where strongest $\mathbf{B}_{LE}$ have been observed [7–9], is left not resolved. So, we get 1 s data for observatories KAK, KNZ, ESA, MIZ, and for short time intervals for UCU and KYS to analyze RF for periods T > 5 s.

3.2 Boso conductivity anomaly

Processing of records from 18 observatories (16 of them are shown in **Figure 3** and KYS and UCU in **Figure 5**) for the determination of horizontal tensors [M] with KAK as the base station yields the absence of noticeable horizontal tensor anomalies in ESA, MIZ, HAR, TTK, and MUR but reveals their existence in KNZ, UCU, OTA, and KYS (**Figure 4a**). In KNZ and OTA the enhancement of real tensor components M_{xx} and M_{yy} equals to ≈40% and ≈30% correspondingly at periods T < 500 s decreasing at longer periods. This result was supported by direct visual measurements described below. At closely located observatories KNZ and OTA, the latitudinal (E-W) component of induction vector at period 450 s and shorter increased (in 2011 comparatively to 2001) in opposite directions: westward in KNZ and eastward in OTA (see **Figure 3b**). It means that between these two observatories, an additional current (of geodynamic origin) appeared in 2011.
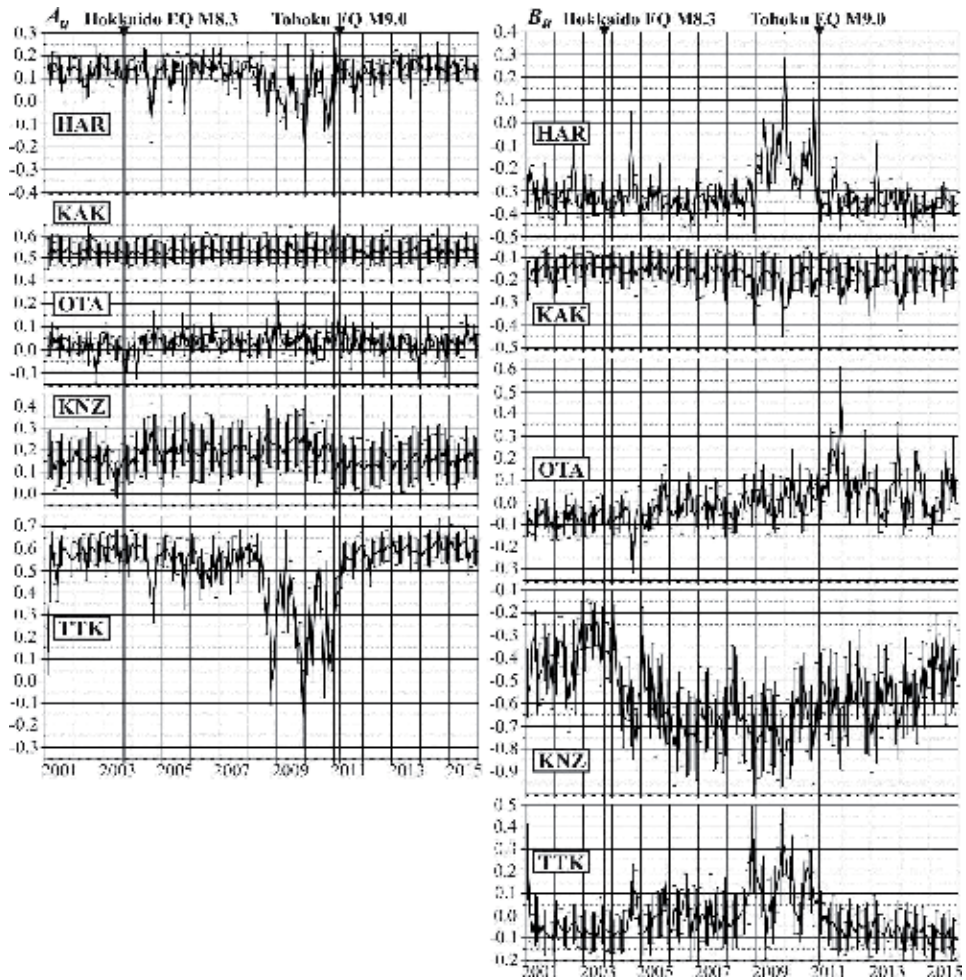
Figure 4.
Variations of the monthly mean induction vector components at the period of 450 s during 2001–2015 at five observatories with significant changes before the Tohoku EQ: HAR, KAK, OTA, KNZ, and TTK. Vertical bars present the uncertainty of every monthly mean value. Two strong EQs are shown by vertical lines.

3.2.1 Visual analysis of geomagnetic records

Considering the geomagnetic field synchronous records (**Figure 3a**), we noticed that magnetotelluric field appears synchronously at all observatories, while noise appears locally at each one. The stations most contaminated by noise are UCU and KNZ which are the nearest to DC railways. But during the after-midnight time interval from ≈1:30 to ≈4:30 LT (16:30–19:30 UT) the strong noise from DC railways almost disappears.

Direct measurements of the strong MT amplitude variations in each component provide a check (not precise but very reliable) of the results obtained by processing. So, the enhancement of B_x at KNZ and OTA at approximately 30–40% exists, and it can be interpreted only by the electrical conductivity anomaly under the observatories, i.e. under the central part of the Boso peninsula.

3.3 Comparison with geology and tectonic evidence

The relation between M_{xx} and M_{yy} anomalies in KNZ defines WNW-ESE strike of the Boso conductivity anomaly. Geological data [25, 26] presented in **Figure 4b–c**
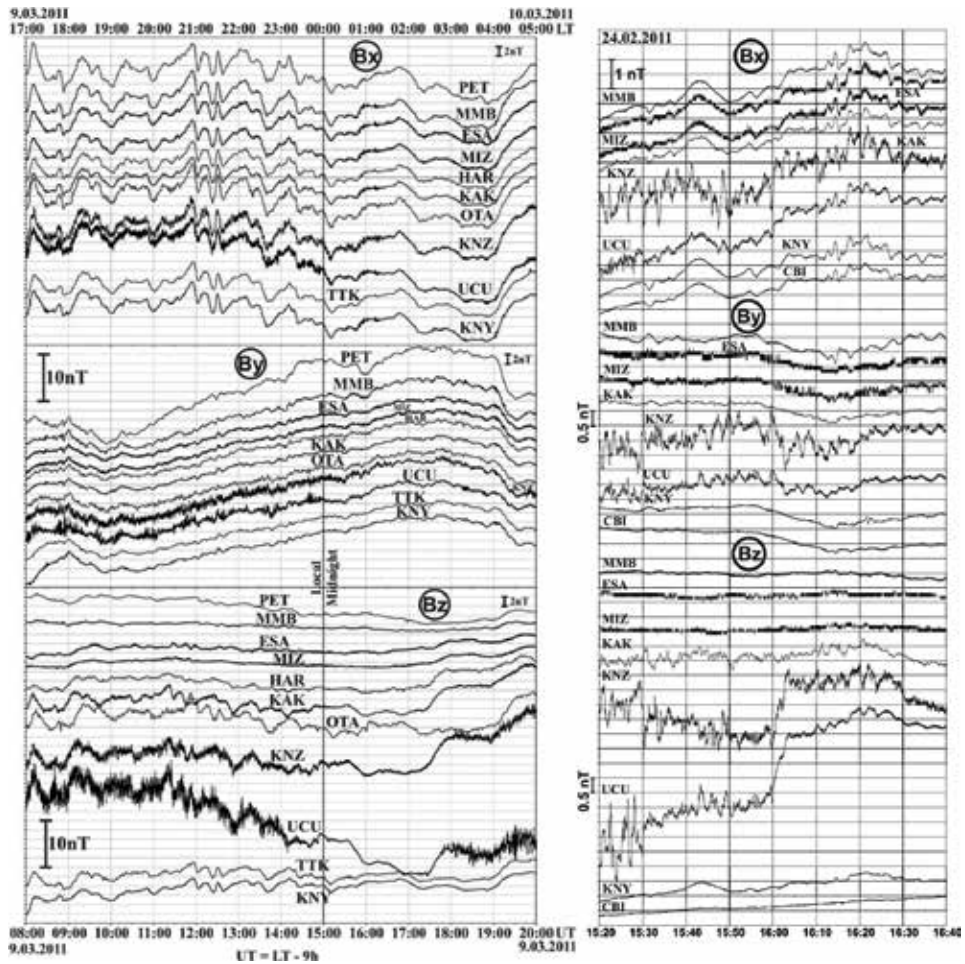
Figure 5.
(a) Synchronous records (1 min data) of 10 Japanese and 1 Kamchatka (PET) geomagnetic observatories 2 days before the Tohoku earthquake. In the UCU and KNZ observatories records, we see during daytime strong noise due to DC electric trains and an absence of this noise during the hours after midnight. Geomagnetic activity presented by global 3 h index Kp was as follows: in the 6–9 UT hours time interval Kp = 1+; in 9–12 UT hours, Kp = 1–; in 12–15 UT hours, Kp = 1; in 15–18 UT hours, Kp = 1–; in 18–21 UT hours, Kp = 1 + . (b) Synchronous record (February 24, 2011) (1 s data) of eight Japanese observatories 80 min after midnight (15 h UT). Magnetic activity was very low: Kp =0+. DC railway traffic is almost stopped, but the noise-like variations were not terminated in the Boso peninsula. Maybe it is a precursory LE which according to [24] started on February 22, 2011.

suggest the existence of anomalous conductor of WNW-ESE strike in Miura Group sediments of the Kanto plain at depth 0–4 km. Relations between M_{xx} and M_{yy} in UCU, OTA, and KYS are different as seen in **Figure 6a**. It means that the direction of anomalous currents is also different under each observatory. Calculations show that at least 50% of anomalous currents should be located near the surface in the sediments of the Kanto plain to fit the received data.

On the other hand, the plate tectonic evidences that the Boso anomaly is located over the Sagami trough, structure at the depth 15–20 km in the complex junction of three lithosphere plates (**Figure 3a**). Strike of the trough is the same, WNW-ESE, so some part of the anomalous conductor can be located in the Sagami trough.

The eastern part of both conductors (shallow sediments and deep trough) has contact with seawater, while the western one can contact with a magma reservoir. In such a circuit it can be some unstable area(s) with conductivity strongly dependent on stress and sensitive to stress changes related with EQs.

In **Figure 6b**, vectors are shown for a period of about an hour (4000 s), at which industrial noise is practically absent and vectors adequately reflect the heterogeneity of geoelectric structure. In **Figure 6c**, vectors at the period 25 s are built with dominated noise field, which is greater than MT field on four observatories considered. Real and imaginary vectors at periods 16, 25, 50, and partly at 200 s (**Figure 6d**) are directed to the source of noises—the nearest railway. To reduce influence of the noise, night records and remote reference technique were used (**Figure 6f**). Received corrected vectors appeared still very scattered (**Figure 6e**) and for monitoring of geodynamic processes can be used cautiously. However, vectors averaged over a long period of time can be used for clarifying of the geoelectric structure. Corrected real vector in KNZ at the shortest periods directs to north.
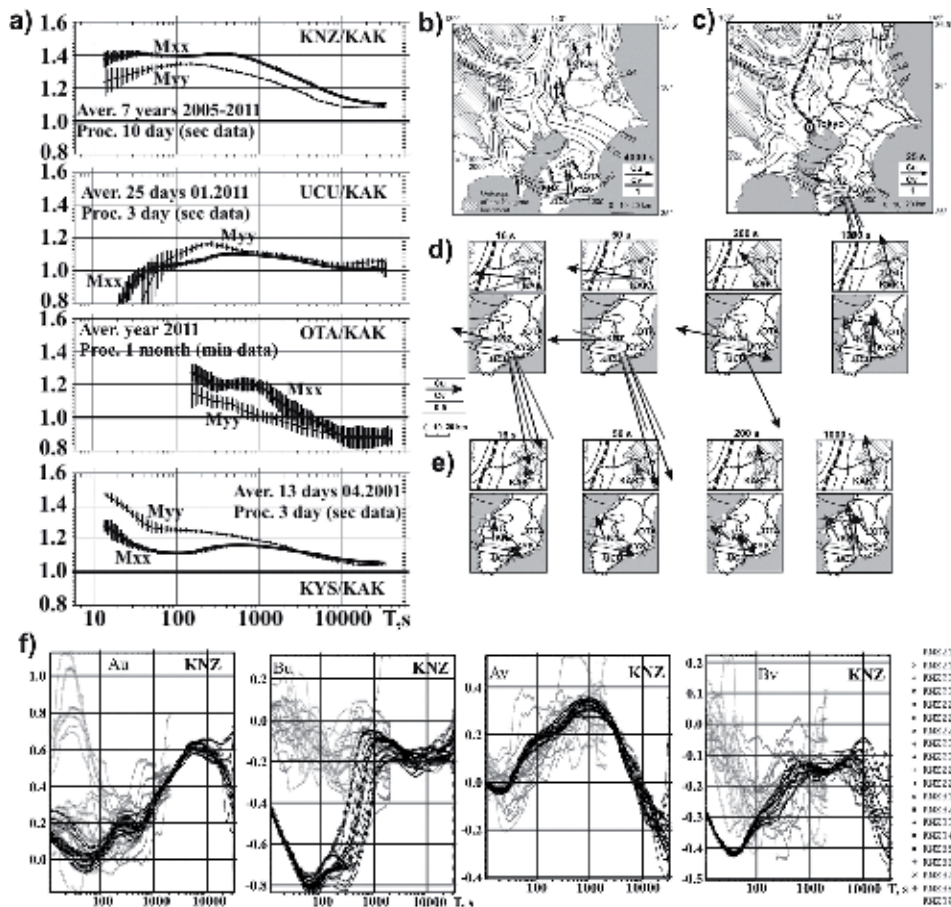
Figure 6.
RFs and Neogene sediments in the Kanto plain and the Boso peninsula. (a) Frequency characteristics of the modulus of horizontal tensor [M] main components at Boso observatories with reference to the base observatory KAK. Every curve is a mean value for 7 years (KNZ), 25 days (UCU), 1 year (OTA), and 12 days (KYS). Interval of averaging (aver.) with the date and the length of processed realizations (Proc.) is written at every graph (they were chosen depending on the interval of available data and their discreteness). (b) Thickness of Neogene sediments [25, 26] and induction vectors for period ≈1 h, named observatories with real and imaginary vectors—is our processing, the other six real vectors are taken from [16]. (c) Thickness of Miura group deposits with "N.8 half graben fills" and induction vectors for T = 25 s obtained from the dominant DC noise and directed to the noise source—DC railways given by thin lines for suburb railways and by thick line for magistral one. (d) Similar results for another four periods. (e) Results of the same data processing with an attempt to make away the impact of the noise by means of either only after-midnight 4 h use or by remote reference technique application. (f) Frequency characteristics of induction vector components at KNZ. Dark lines for the wide period range are the results of ss (single station) processing of 3-day realizations with sliding reference to middle day; light lines, processing of after-midnight 4 h records of the same 20 days from February 18 to March 9, 2011.

It means that the most conductive part of Boso electrical conductivity anomaly is located to south of KNZ, apparently near the southern side of the asymmetric "N.8 half graben fills" of the Miura Group sediments [26].

Results of the single station and nighttime records processing at KNZ are given in **Figure 6f**. We see that full-day and nighttime results significantly differ from each other only for B_u and partly B_v components because a railway is located to the west from KNZ and brings the distortions mainly in the eastern component. The northern component is less affected by noise at periods 100 s and more that opens the possibility to use it for separation of EQ precursor that will be used in the next section.

4. Short-term precursor separation

4.1 Introductory remarks

The induction vector derived from very noisy records, practically from noise field, has small stable phase. Therefore, if some other magnetic fields, which are usually not so stable (let it be a precursor field), are superimposed on the field of noise, exactly the phase of induction vector will be the most sensitive component for a precursor separation.

Below we apply a new approach developed by Tregubenko [27], who used it for processing the data of seismo-prognosis monitoring network in Ukraine. He separated precursors before few strongest (M ≈ 4) Crimean EQs occurred during 15 years, in particular before the Sudak, Crimea EQM3.9 on January 24, 2005 [27]. We applied this approach to KNZ, KAK, and ESA 1-s data, but the precursor was found only in KNZ. We can explain this by the spatial selectivity of the precursors: high sensitivity of KNZ place is quite natural in virtue of Boso electrical conductivity anomaly located just under KNZ observatory.

4.2 Processing of KNZ data

The processing was made with the use of Varentsov's [22] program. Coherences were used as weight estimates for averaging the results. To minimize the effect of noise, the estimates with multiple coherences less than 0.7 were ignored that allowed us to obtain minimally shifted estimates of induction vector's components. Maximum anomalous effect before the Tohoku EQ was observed for the phase of the induction vector northern component—arg(A) for periods 100–200 s. For the longer periods, the anomaly gradually decreases, so that we now present the results for T = 100 s. The processing and analysis were made in two steps:

Step 1. A 7-year-long (2005–2011) geomagnetic field time series with every 1 s reading was processed for every month as a single unit. Arg(A) time series with every month reading were received as in **Figure 7a** and analyzed by a polynomial approximation approach. The most significant first-, second-, and seventh (quasi-annual)-order polynomials were extracted from the rough data, and we obtained **Figure 7b** which is more perspective for comparison with EQs. But 1-month temporal resolution of RF is not sufficient for such an analysis. As for the Tohoku EQ precursors, we see a 9-month-long negative anomaly in 2010 approximately 1 year before the main event.

Step 2. A 2-year-long (2010–2011) 1 s time series were processed for every day as single unit. Large scatter of everyday results was reduced by averaging with moving window of 5 days long with 1-day shift. From these curves, i.e., arg(A) time series with everyday reading, we extracted first-, second-, and seventh (quasi-annual)-order polynomials determined in step 1. The result is shown by the gray rough curve
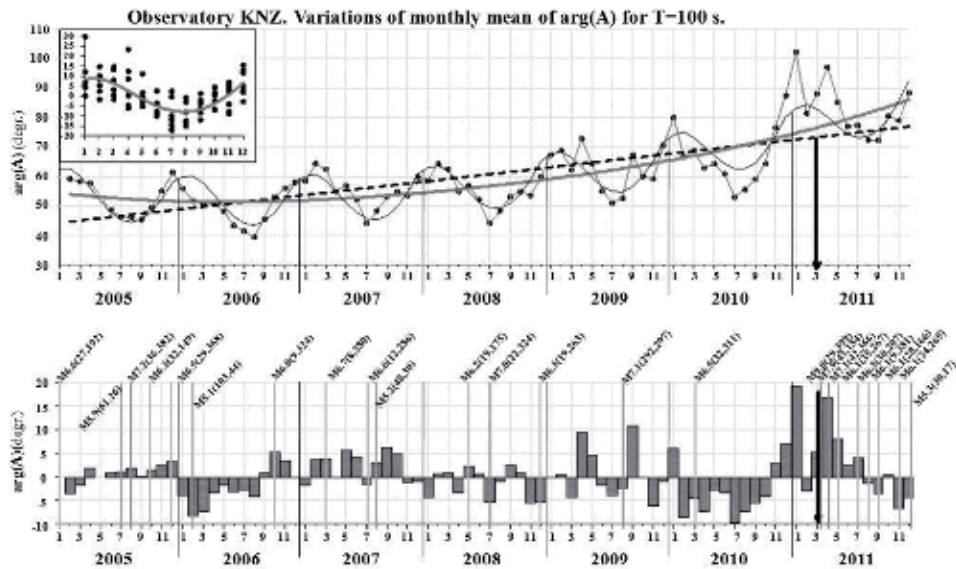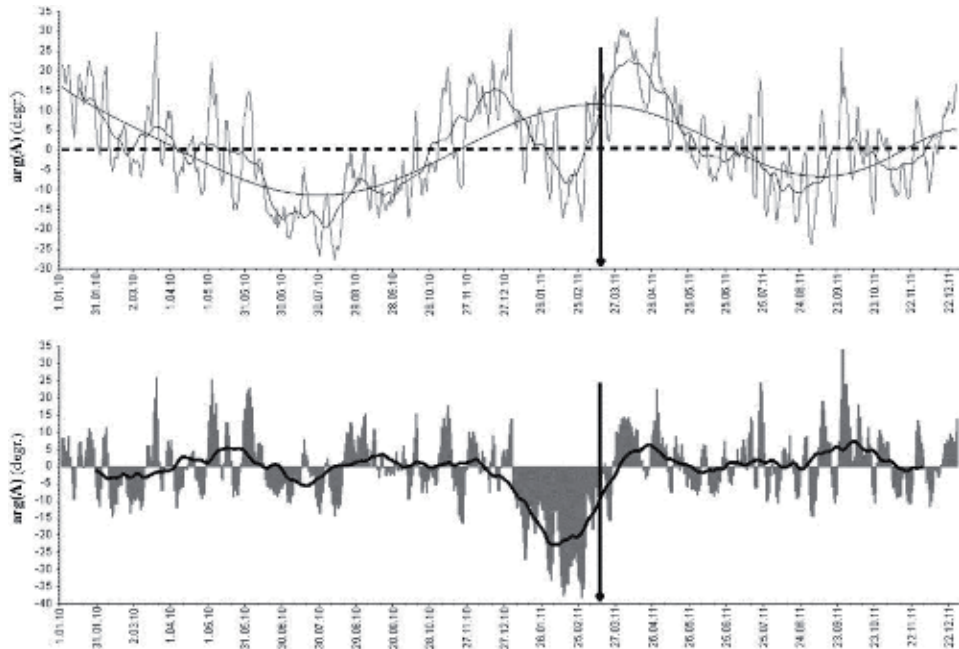
Figure 7.
Variations of arg(A) for the period T = 100 s at the observatory KNZ during 2005–2011. (a) Monthly values of arg(A) are given by dots. The dashed straight line and bold solid line are the first- and second-order polynomials, respectively. Thin smooth line is quasi-annual variations obtained as seventh-order polynomial approximation. In the upper left corner, the determination of mean annual variation is shown (first- and second-order polynomials were excluded). (b) Variations of arg(A) after removal of the first-, second-, and seventh (quasi-annual)-order polynomials. Moments of strong EQsM > 5 are indicated by vertical lines with given magnitude M (the first number in parentheses is the depth of the hypocenter, and the second one is distance from epicenters to the observatory KNZ, both are given in km).

in **Figure 8a**. The bold solid line is the result of averaging with moving window of 29 days with 1-day shift to suppress monthly variations arising from the Moon rotation around the Earth (gravity effect) and the Sun rotation around its axis (magnetic activity effect). The mean for 7 years 2005–2011 annual variation have been subtracted, but we see a residual annual variation in **Figure 8a** (RF annual variation enhancement was recorded at several observatories 2–3 years before Tohoku EQ and can be considered as middle-term precursor). So, such a residual annual variation was determined once more from 2-year data presented in **Figure 8a** and subtracted; the result is presented in **Figure 8b**.

4.3 Discussion of short term precursor

The variations of arg(A) given by the bold solid line in **Figure 8b** are cleaned from periodic variations of annual and monthly periods, which make it more convenient to identify EQ precursors. Indeed, we see a strong bay-like variation that begins almost 2 months before the Tohoku EQ and has approximately 2-month duration. This is in good agreement with the finding of Prof. Varotsos' team [14, 15]. In particular, Varotsos et al. showed that the initiation of an SES activity in Japan appears almost simultaneously with the minimum of the fluctuations of the order parameter of seismicity analyzed in natural time, and such a minimum was clearly observed [15] on January 5, 2011, that is, almost 2 months before the Tohoku EQ occurrence.

Time of beginning of a bay-like precursory variation and its duration depends on the magnitude of an expected EQ. This time is equal to approximately 2 weeks for the processed Crimean EQs with magnitude approximately 4 [27] and 2 months for Tohoku EQ with magnitude 9 according to our study.

Figure 8.
*Variations of arg(A) for the period T = 100 s at the observatory KNZ by the data for 2010–2011 years. (a) Rough gray curve is the result of everyday processing after moving averaging with window length of 5 days with 1-day shift. Bold solid line is the result of averaging with moving window of 29 days (for elimination of monthly variation) with 1-day shift. (The first -, second-, and seventh (quasi-annual)-order polynomials determined from seven years data and presented in **Figure 7a** were subtracted). The time of the Tohoku EQ on 11.03.2011 is marked by a vertical arrow. (b) The same after the removal of residual annual variation determined from 2010-2011 data and given in **Figure 8(a)** by thin line.*

Kopytenko et al. [24] compared nighttime records of KAK and UCU observatories (see **Figures 3**, **6**) in frequency range of 0.33–0.01 Hz for the interval of 21 days before the Tohoku EQ, that is, since February 2, 2011 till March 3, 2011. They found the appearance of anomalous changes on February 22, 2011 (18 days before EQ): decrease of the correlation coefficients between geomagnetic components of KAK and UCU observatories and rise of B_z component in sub-diapason 0.033–0.01 Hz. It was interpreted as appearance LE.

Now let us see **Figure 5b**. It presents nighttime records on February 24, 2011, 16 days before the Tohoku EQ, in geomagnetically quite interval with rather good temporal and amplitude resolution. MT variations in the horizontal components are almost the same at all presented observatories distributed at the territory 2000 km long. In the records of UCU and KNZ (separated by 17 km) we see strong varitations with frequencies of 0.002–0.1 Hz and amplitude of 0.2 and 0.5 nT, respectively, and even more strong variations in B_z component. All of this is in good agreement with the results of [24]. Variations in KNZ and UCU cover approximately the same frequency diapason as in [24], slightly correlate one with the other, and are not observed at other observatories. All signs of LE! But we cannot exclude that there are some remainders of the daytime noise from DC traffic. We need several more observatories (as SES network in Greece) for more definite conclusions.

5. Discussion of LE features

To use the LE for EQ prediction, one needs to know its lead time, amplitude, frequency characteristic, and expected distribution of sensitive places in the Earth

Earthquake	Δr, km	Δt, day or hour	A, nT	f, Hz	A/Δr, nT/km
Alaska M9.2	440 (30)	1 h	100		0.28 (3.3)
Loma Prieta M7.1	7	36 day, 13 day, 3–0 h	1.5, 2, 5	0.01–0.5	0.21 0.29 0.71
Taiwan Chi-Chi M7.6	80 (≈5)	>32 day, 10–2 days	200		2.5 (40)
Spitak M6.9	130	4 h	0.1	0.1–1	0.001
Racha aftershock M6.2	≈50	4–1 days, few h	≈1	0.1–1	0.02
Racha aftershock M4	35	Hours	1	0.1–1	0.029
Greneva-Kozani M6.6	80	25 days	≈1?	≈0.05?	

Δr, distance between observatory and EQ epicenter (or nearby displacement fault, given in brackets); Δt, lead time of LE appearance before the EQ; A, LE amplitude; f, frequencies at which LE recorded or the maximum of LE frequency characteristic. Scatter of A/Δr ratio shows strong irregularities in spatial decay of LE.

Table 2.
Parameters of the observed LE.

surface. This knowledge can be obtained now only empirically. We can extract the necessary properties from the data presented in Section 1.3 supplementing them with other published data. An attempt of such extraction is presented in **Table 2**.

The results depend of the conditions of observation. So, sampling rate of 10 min and compressed time scale in [12] describing two EQs in Taiwan exclude frequency content estimation. Important parameter – lead time Δt is properly determined only before Loma Prieta EQ when signal-to-noise ratio was large during long time that allowed separate three stages of the precursor appearance. Spatial selectivity complicates the formulation of the LE spatial regularities. Thus, we are in the very beginning of LE phenomenon study and use.

6. Conclusions

We have calculated induction vectors using data from Japanese observatories for many years preceding the 2011 Tohoku EQ. In 2008–2010 at six observatories, we found anomalous variations of induction vectors, which are regarded as middle-term EQ precursors. Those observatories are located not at the shortest distances from the EQ epicenter, which is in general agreement with the well-known phenomenon of spatial selectivity of EQ precursors. The analysis of horizontal tensors reveals a conductivity anomaly under the central part of the Boso peninsula with a WNW-ESE strike coinciding both with the Sagami trough strike and well conducting 3-km-thick sediment strike. A joint analysis of geoelectric and tectonic data leads to a preliminary conclusion that the Boso conductivity anomaly connects two large-scale conductors: Pacific seawater and a deep magma reservoir beneath a volcanic belt. Similar anomaly was found earlier in Kamchatka [21]. Then, applying original data analysis with the elimination of annual and monthly variations, we separated two-month-long short-term EQ precursor of the Tohoku EQ.

Several cases of lithosphere emission LE before strong EQs were reviewed and analyzed, and preliminary portrait of LE precursor was compiled: LE can appear several times with lead time a month(s), weeks, days, hours, and minutes and can attain amplitude several hundreds of nT which rapidly and not uniformly diminishes with moving away from the source. Typical frequency content/maximum is 0.01–0.5 Hz. As it is widely accepted [5], LE is generated by the process of

microcracks opening in the course of EQ preparation and should be a rather common phenomenon. It is not quite clear how high-frequency microcrack radiation propagates through many kilometers of the Earth's crust to be recorded at the Earth surface. Seemingly, the radiation finds the optimal pathways leading to sensitive places on the earth surface where signal can be observed. Then, the search of sensitive spots opens new channel of information for the Earth interior study.

Recommendation on the LE monitoring for the strong EQ prediction

1. Network must allow the gradient measurements, so a minimum of three magnetometers must be installed for synchronous records [24].

2. The best but very expensive is the SES monitoring network in Greece. Electrical dipoles can be supplemented or replaced by magnetometers. We recommended for use the practice of sensitive places search and use [11] and the methodology of LE sophisticated analysis developing by Prof. Varotsos' team [14, 15].

3. RF approach is a valuable supplement to LE. It has lower temporal resolution but yields additional information on the conductivity variations in the EQ preparation zone.

Author details

Igor I. Rokityansky*, Valeriia I. Babak and Artem V. Tereshyn
Ukrainian National Academy of Sciences, Subbotin Institute of Geophysics, Kiev, Ukraine

*Address all correspondence to: rokityansky@gmail.com

IntechOpen

References

[1] Wang K, Chen Q-F, Sun S, Wang A. Predicting the 1975 Haicheng earthquake. Bulletin of the Seismological Society of America. June 2006;**96**(3): 757-795. DOI: 10.1785/0120050191

[2] Rokityansky II. Geoelectromagnetic Investigation of the Earth's Crust and Mantle. Berlin Heidelberg New York: Springer-Verlag; 1982. 381 p

[3] Berdichevsky MN, Dmitriev VI. Models and Methods of Magnetotellurics. Berlin Heidelberg: Springer-Verlag; 2008. 564 p. DOI: 10.1007/978-3-540-77814-1

[4] Chave AD, Jones AG, editors. The Magnetotelluric Method. Cambridge: Cambridge University Press; 2012. 584 p. DOI: 10.1017/CBO9781139020138.002

[5] Surkov V, Hayakawa M. Ultra and Extremely Low Frequency Electromagnetic Fields. London: Springer Geophysics; 2014. 486 p. DOI: 10.1007/978-4-431-54367-1

[6] Moore GW. Magnetic disturbances preceding the 1964 Alaska earthquake. Nature. 1964;**203**:508-509. DOI: 10.1038/203508b0

[7] Frather-Smith AC, Bernardi A, McGill PR, Ladd ME, Helliwell RA, Villard OG Jr. Low-frequency magnetic field measurements near the epicenter of the Ms 7.1 Loma Prieta earthquake. Geophysical Research Letters. 1990;**17**(9):1465-1468. DOI: 10.1029/GL017i009p01465

[8] Kopytenko YA, Matiashvili TG, Voronov PM, Kopytenko EA, Molchanov OA. Detection of ultra-low-frequency emissions connected with Spitak earthquake and its aftershock activity, based on geomagnetic pulsations data at Dusheti and Vardzia observatories. Physics of the Earth and Planetary Interiors. 1993;**77**:85-95

[9] Kopytenko YA, Matiashvili TG, Voronov PM, Kopytenko EA. Observation of electromagnetic ultralow-frequency lithospheric emission in the Caucasian seismically active zone and their connection with earthquakes. In: Hayakawa b M, Fujinawa Y, editors. Electromagnetic Phenomena Related to Earthquake Prediction. Tokyo: Terra Scientific Publishing Company (TERRAPUB); 1994. pp. 175-180

[10] Rokityansky II. Spatial selectivity of earthquake's precursors. Physics and Chemistry of the Earth. 2006;**31**: 204-209. DOI: doi.org/10.1016/j.pce.2006.02.028

[11] Varotsos AP. The Physics of Seismic Electric Signals. Tokyo, Japan: TERRAPUB; 2005. 338 p

[12] Tsai YB, Liu JY, Ma KF, Yen HY, Chen KS, Chen YI, et al. Precursory phenomena associated with the 1999 chi-chi earthquake in Taiwan as identified under the ISTEP program. Physics and Chemistry of the Earth. 2006;**31**:365-377

[13] Varotsos P, Alexopoulos K, Lazaridou M. Latest aspects of earthquake prediction in Greece based on seismic electric signals, II. Tectonophysics. 1993;**224**:1-37. DOI: 10.1016/0040-1951(93)90055-O

[14] Varotsos PA, Sarlis NV, Skordas ES, Lazaridou MS. Seismic electric signals: An additional fact showing their physical interconnection with seismicity. Tectonophysics. 2013;**589**:116-125. DOI: 10.1016/j.tecto.2012.12.020

[15] Sarlis NV, Skordas ES, Varotsos PA, Nagao T, Kamogawa M, Tanaka H, et al. Minimum of the order parameter fluctuations of seismicity before major earthquakes in Japan. Proceedings of the National Academy of Sciences of the United States of America.

2013;**110**:13734-13738. DOI: 10.1073/pnas.1312740110

[16] Yanagihara K, Nagano T. Time changes of transfer function in the Central Japan anomaly of conductivity with special reference to earthquake occurrences. Journal of Geomagnetism and Geoelectricity. 1976;**28**(2):157-163

[17] Fujita S. Monitoring of time changes of conductivity anomaly transfer functions at Japanese magnetic observatory network. Memoirs of the Kakioka Magnetic Observatory. 1990;**23**:53-87

[18] Fujiwara S. Temporal changes of geomagnetic transfer functions using data obtained mainly by the geographical survey institute. Bull Bulletin of the Geographical Survey Institute. 1996;**41**:1-25

[19] Rokityansky II, Tregubenko VI, Babak VI, Tereshyn AV. Induction vector and horizontal tensor components variations before the Tohoku earthquake on the 11th march 2011 according to the data of Japanese geomagnetic observatories. Geophysical Journal. 2013;**35**(3):115-130. (in Russian)

[20] Rokityansky II, Babak VI, Tereshyn AV. Geomagnetic activity impacts on the results of the induction vector calculations. Geophysical Journal. 2015;**37**(6):86-98. (in Russian)

[21] Rokityansky II, Babak VI, Tereshyn AV. An analysis of geomagnetic response functions prior to the Tohoku, Japan earthquake. Journal of Volcanology and Seismology. 2016;**10**(6):78-91

[22] Varentsov IM. Arrays of simultaneous EM soundings: Design, data processing and analysis. In: Spichak V, editor. EM Sounding of the Earth's Interior. Methods in Geochemistry and Geophysics. Vol. 40. Heidelberg, London: Elsevier;

2007. pp. 259-275. DOI: 10.1016/S0076-6895(06)40010-X

[23] Klymkovych TA. Peculiarities of temporal variations of anomalous magnetic field and induction vectors in the Transcarpathian seismic-active trough [PhD thesis] Kiev: Institute of Geophysics; 2009 (in Ukrainian)

[24] Kopytenko YA, Ismaguilov VS, Hattori K, Hayakawa M. Anomaly disturbances of the magnetic fields before the strong earthquake in Japan on march 11, 2011. Annals of Geophysics (Italy). 2012;**55**(1):101-107. DOI: 10.4401/ag-5260

[25] Suzuki H. Underground geological structure beneath the Kanto plain, Japan. National Research Institute for Earth Science and Disaster Prevention, Japan. 2002;**63**:1-19

[26] Takahashi M, Yanagisawa Y, Hayashi H, Kasahara K, Ikawa T, Kawanaka T, et al. Miocene subsurface half-grabens in the Kanto plain, Central Japan. Proceeding of International Workshop on Strong Ground Motion Prediction and Earthquake Tectonics in Urban Areas. 2005:65-74

[27] Tregubenko VI. Seismoprognostic researches. In: Goshovsky SV, editor. 50 Years of Ukrainian State Geological Institute (1957-2007). Anniversary Directory. Kyiv: Ukr SGPI; 2007. pp. 52-56 (in Ukrainian)

Edited by Masaki Kanao and Genti Toyokuni

The importance of seismic wave research lies not only in our ability to understand and predict earthquakes and tsunamis, but it also reveals information on the Earth's composition and features in much the same way as it led to the discovery of Mohorovicic's discontinuity. As our theoretical understanding of the physics behind seismic waves has grown, physical and numerical modeling have greatly advanced and now augment applied seismology for better prediction and engineering practices. This book demonstrates the latest techniques and advances in seismic wave analysis from a theoretical approach, data acquisition and interpretation, to analyses and numerical simulations, as well as research applications. The major topics in this book cover aspects on seismic wave propagation, characteristics of their velocities and attenuation, deformation process of the Earth's medium, seismic source process and tectonic dynamics with relating observations, as well as propagation modeling of seismic waves.

IntechOpen